UNIVERSITÁ DEGLI STUDI DI CATANIA

FACOLTÁ DI SCIENZE MATEMATICHE, FISICHE E NATURALI

DOTTORATO DI RICERCA IN FISICA - XXIII CICLO

Angela Elisa Messina

CHROMOSPHERIC ACTIVITY AND LITHIUM ABUNDANCE IN THE NGC2516 AND NGC3766 OPEN CLUSTERS

TESI DI DOTTORATO

Tutor:
Chiar.mo Prof. ***A.C. Lanzafame***

Coordinatore:
Chiar.mo Prof. ***F. Riggi***

DICEMBRE 2010

A chi mi vuole bene e continua a credere in me...

Contents

Abstract

The aim of this thesis is the analysis of chromospheric activity and lithium abundance of late type stars in open clusters of different ages. The study of open cluster is very important for our understanding of stellar evolution and atmospheres, since all cluster members have almost the same age and chemical composition and this allows to infer their properties more easily than individual stars. In this work two open clusters have been considered, NGC2516 and NGC3766, using spectra acquired by the ESO spectrograph FLAMES at VLT, in the LiI and CaII H and K region.

Most of our knowledge of young stars comes from the observations of general properties of open clusters, since they represents a good tool for testing the stellar evolution models, and the age measurement' methods. In fact, stellar ages can be determined only by comparison with theoretical models, and open clusters are widely used to calibrate methods of age determination, since their observation allows to determine average properties of a group of stars approximately coeval.

One of the methods used to determine the age of young stars is the lithium depletion, based on the determination of the lithium abundance of a cluster's star. This method has been used in this work to determine the age of both observed clusters. Their lithium depletion has been derived, confirming that, for the cluster NGC2516, the age is approximately around 150Myr, as observed previously by other authors. Assuming solar metallicity for NGC3766, direct comparison of Li equivalent with other clusters indicates an age close to that of the Pleiades or even older, in disagreement with previous age determination. A metallicity higher than solar may explain at least partially this disagreement.

Chromospheric activity in NGC2516 has also been studied using CaII H and K lines VLT/FLAMES-GIRAFFE observations. Since no VLT/FLAMES-GIRAFFE observations of Mt. Wilson standards are available, I applied the method of Linsky et al. (1979b) and Strassmeier et al. (2000). A comparison with the standard Mt. Wilson method has been done using FEROS spectra. A study of astrophysical parameter determination using the spectral region between 3990 and 4040 A has also been performed.

This work is organized as follows: the problem of age determination in open clusters

is briefly discussed in Chapter 1; Chapter 2 contains a review of chromospheric activity indicators; Chapter 3 contains a description of the cluster studied; Chapter 4 describes the reduction of VLT/FLAMES-GIRAFFE data; Chapter 5 describes the method used to derive stellar physical parameters. Finally, in Chapter 6 the chromospheric activity analysis for NGC2516 and the lithium abundance analysis in both NGC2516 and NGC3766 are presented.

Chapter 1

Introduction: stellar ages and lithium abundance

Open clusters are groups of up to few thousand of stars, mainly found in the galactic plane of spiral galaxies. Open clusters' members forms from the same molecular cloud, and for this reason are approximately coeval, so they represents excellent laboratories for studying stellar evolution. Furthermore, while most of the fundamental stellar properties such as mass, radius, and rotation velocity are directly derivable through the study of orbital motion, eclipses, and rotation period measurements, stellar ages, instead, can be determined only by comparison with theoretical models. The knowledge of star's age provide more constraints about the physical state of a star.

The methods used to derive the age can be divided into two principal groups: model-dependent (i.e. based on the comparison with a model) and empirical (i.e. based on observed relations between a measured characteristic and the age). The most difficult problem in the age determination is the need of a calibration. The usual way to calibrate an age relation is to observe stars in clusters in order to have many stars and determine average properties with a good precision. For this reason, open clusters' studies are very important since, at least in principle, open clusters' ages, especially the nearby ones, should be well known. A limitation is given by the fact that the galactic forces tend to disgregate open clusters on a time-scale of $\sim$200 Myr, expecially the weakly-bounded ones (Soderblom, 2010).

In the following sections I will describe the age measurements methods mostly used, how the study of open clusters is useful for age estimation, and the relation between age and activity.

1.1 Age measurements methods

Open clusters provide a good benchmark to study age-related properties and an essential tool is the Hertzsprung-Russell diagram (or the colour-magnitude diagram). Very young

clusters usually have ages determined from their massive stars at the MS-turnoff, whereas intermediate-age clusters have ages determined from intermediate-mass stars where the inner mechanism is different. Old clusters'ages often depend on the locations of evolved stars in the HR-diagram. Soderblom (2010) listed the methods used to to determine the age of open clusters:

- The Lithium depletion boundary;
- The Kinematic expansion, based on the study of the motions of a group of stars into the past to determine when they were in closest physical proximity, which is assumed to be the time of formation;
- The Isochrone fitting, based on the comparison of the models with the entire cluster data;
- Empirical methods (rotation, activity, and lithium), usually applied to stars younger than $\tau < 0.5$Gyr, even if with these methods is observed a scatter that exceeds the change in the quantity over significant times.

Unfortunately, there are not many open clusters with ages determined with all these techniques, so it is difficult to make comparisons to establish the validity of these methodologies. Moreover, rotation and activity are not independent each other and even their physical correlation is known. Furthermore, the methods used for determing the ages of young stars can be quite different from pre-main sequence (PMS) and main sequence (MS) stars.

The most used method for PMS stars in open clusters is the isochrone fitting. Beyond $\sim$200 Myr age this method becomes impractical because the displacement of low mass stars above the zero-age main sequence (ZAMS) becomes small relative to the errors introduced by uncertainties in metallicity, reddening, etc. However, in principle, at ages significantly less than that value, it should be possible to derive accurate ages for relatively nearby open clusters from PMS isochrone fitting (Stauffer, 2004). For PMS stars, the paper by Naylor et al. (2009) presented three methods for determing the age:

- The empirical isochrones, based on the comparison with the models, allow us to derive an age ordering, but not to an actual age, since the position of the isochrones depends from the distances, with which the age degenerate.
- The radiative-convective gap represents the gap in colour-magnitude diagram between the PMS and the MS, due to the change in the internal structure between the fully convective interiors of the PMS stars and the partially radiative one of the MS stars.

The limitation of this method is that it needs to be calibrated with respect to age which is derived from other methods, before it can be used as an age indicator.

- The nuclear age is based on the fact that before stars turn off the MS, they evolve redwards away from the zero-age MS, driven by their nuclear evolution. The measure of this effect in the colour-magnitude diagram can provide an age indicator.

For MS solar-type stars, instead, the observational uncertainties in the HR-diagram position can be large enough to include a wide fraction of the star's lifetime (Mamajek, 2009). For this reason, it is useful to consider alternative age indicators beyond deriving individual isochronal ages. The paper of Hillenbrand et al. (2009) list the following techniques:

- The comparison of stars in the HR diagram with models is useful only for stars younger than the Sun, with age less than 20-30 Myr old (in the PMS phase), and is based on the comparison with models. However, this method needs confirmation from other activity/lithium diagnostic;

- The measure of the chromospheric activity, using the chromospheric index R'_{HK} (defined in Chapter 2), that ranges approximately from 10^{-4} to 10^{-5} with saturation above -4.35 dex. It increases with rotation leading and is most useful for slow rotators of age >200Myr;

- The measure of the coronal activity index $R'_{Xray} = (L_{Xray}/L_{bol})$(defined as the luminosity measured in the X band and divided for the bolometric one), that ranges from 10^{-3} to 10^{-7} with saturation above -4.0 dex. It also increase with rotation;

- The measure of rotation has maximum spread around the age of α Per ($\sim$80 Myr), due to interaction between the star and its circumstellar disk, and can provide another indication of the age of cluster;

- The lithium depletion of Li λ6707Å is independent from the other indicators. It is related both to standard stellar evolution and to rotation, but generally has a factor of two of spread at constant age and mass. It is usually used for stars with age in the range of 30-200 Myr.

The behaviour of all these empirical quantities with age is mass dependent and in Figure 1.1 are summarized using the calibrations done by Hillenbrand et al. (2009). In each of them one can see the same LogAge range as function of different empirical indicators.

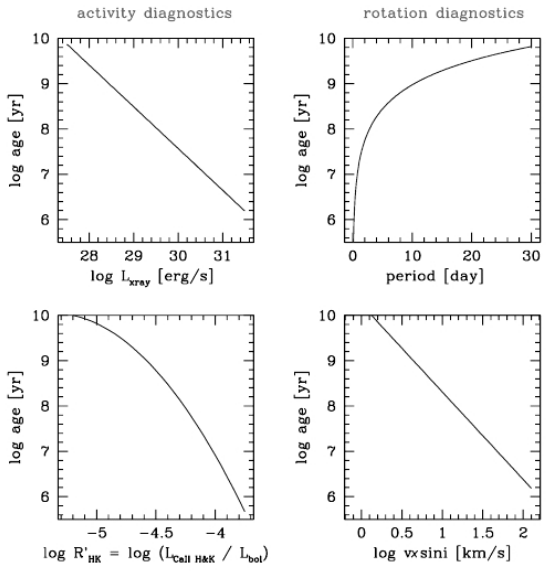

Figure 1.1: Calibration obtained by Hillenbrand et al. (2009) between observed diagnostic and stellar ages for solar colour stars, divided in activity and rotation diagnostic. The ages are derived using open clusters of known ages and theoretical methods such as the MS-turn off and the lithium depletion boundary.

1.2 Lithium depletion

As previously said, the measure of the lithium abundance in open star clusters is one of the most used methods to infer the age of the cluster studied. Moreover, open clusters are excellent laboratories for investigating non-standard stellar physics relating to Li depletion, since they are coeval groups of stars with very similar compositions. By choosing clusters with a range of ages and compositions one can test the validity of standard stellar evolution model.

Lithium plays a special role in astrophysics since it is the only metal that the Big Bang has produced in significant amounts and that is destroyed at relatively low temperatures in the stellar interiors via (p, α) and/or (p, d) reactions (together with other light elements such as Be and B). Although isotopes of these elements are observed to be much less abundant than those of neighboring atomic species, they are far too abundant to be accounted for in terms of standard stellar nuclear processing. For these reasons, its abundance becomes an important cosmological indicator and a useful tracker of particle transport in stars (Michaud & Charbonneau, 1991).

When a star reaches the MS, lithium survives only in few percent in mass of the outer envelope. In fact, the value of Li abundance is equal to the ZAMS one to the depth at which $T = 2.6 \times 10^6$K, then it falls rapidly to zero. During the MS lifetime, in K- and M-dwarfs, the content of lithium in the envelope varies slowly in time, therefore, the base of the superficial convection zone is deep enough to reach the depth at which $T = 2.6 \times 10^6$K, and lead to

Li burning in a manner similar to PMS Li burning (Michaud & Charbonneau, 1991). This technique, based on the observation of the lithium abundance, follows the assumptions that up to 10 million years, all stars retain cosmic lithium abundance, but at about 10Myr the core temperature of low mass stars below 0.25 $M_\odot$ reaches the lithium fusion temperature and their surface lithium abundance go to zero. As the cluster age go further the mass corresponding to where lithium fusion begins reaches 0.075 $M_\odot$ at ∼125Myr, thus, at age 125Myr stars with mass from 0.25 to 0.075 $M_\odot$ would have not detectable lithium, while stars below 0.075 $M_\odot$ will retain their original lithium abundance. At 250Myr the boundary would reach 0.065 $M_\odot$, and at this age the method ceases to provide information about the age of older clusters, since stars with mass below 0.065 $M_\odot$ never reach core temperature hot enough for lithium fusion (Stauffer, 2000).

An example of the lithium depletion for two well studied clusters, the Pleiades and the Hyades, is plotted as function of temperature, in Figure 1.2.

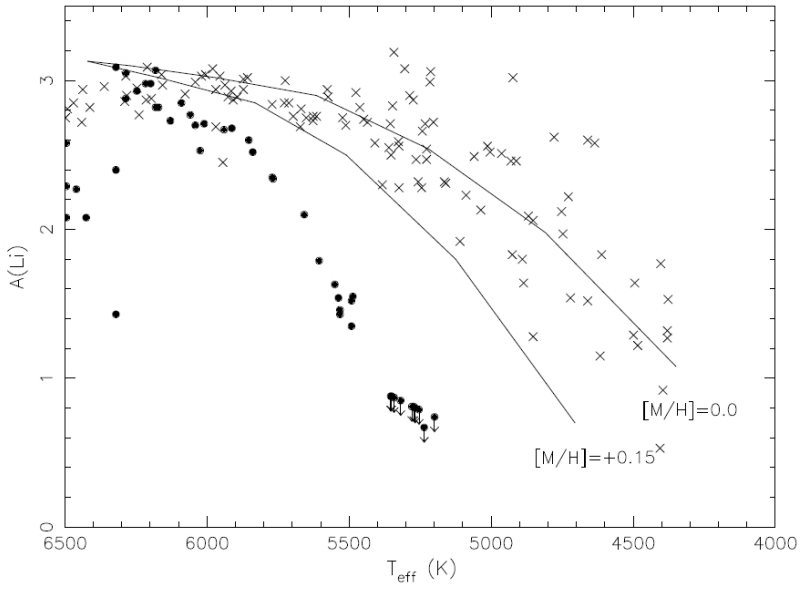

Figure 1.2: Li abundances for members of the Pleiades (crosses) and Hyades (dots). The solid lines are standard model predictions of PMS Li depletion for two different compositions (Jeffries, 2000, and reference therein).

The study of lithium abundance also allows to test the precision of the "standard model", but Michaud & Charbonneau (1991) and after Jeffries (2000) pointed out that this one does not explain well the lithium depletion seen in open clusters. In fact, it gives a good explanation, through PMS burning, of the abundance in a young cluster, the Pleiades, and of the lithium abundance in the halo star (close to the cosmological one). Also, it does not explain the Li abundance in G stars of clusters older than than 10^8 yr nor in the Sun.

Finally, a connection between the lithium depletion and the rotation has been suggested

by Jeffries (2000), who stated that the scatter observed in G and K stars in the Pleiades can be correlated with rotation. Fast rotating stars have suffered little Li depletion whereas slowly rotating stars show both high and low Li abundance. Moreover, there are observational indications that rapidly rotating stars preserve lithium better than slow rotators of the same mass (Tschäpe & Rüdiger, 2001, and reference therein). In order to explain the observed depletion, lithium must be transported below the convection zone (the "tachocline"). The model calculations lead to the result that this transport is the less effective the faster the stellar rotation is. They verified this for a samples of stars of the same age and the same metallicity, but with different rotation rates, i.e. G-type stars in young and intermediate-age clusters, finding that rotation may play a role for inducing the Li abundance spread but, obviously, it cannot be the only parameter which is responsible for it.

1.3 Age and activity

Among the methods listed before, the relation between age and chromospheric activity has also been considered. In particular, it is widely used as an age indicator for solar-type stars based on the evidence that there is a smooth evolution from young and active to old and inactive stars. Wilson (1968) noticed that chromospheric activity decreases during the main sequence life time of late type stars like the Sun, and that the strength of the emission in the core of the CaII H&K lines could be used as indicator of chromospheric activity level. From that time on, the possibility of using the emission from these lines to measure stellar ages has been widely explored by different surveys, such as the Mount Wilson program. Historically, the normalised chromospheric fluxes to bolometric emission, usually indicated with $\mathrm{R'_{HK}}$ (Noyes et al., 1984), has been known as a common age estimator for field stars with a mass roughly equal to the Sun one. The description of the different methods of measure of the activity levels in these lines will be described in more details in Chapter 2.

In a recent paper of Mamajek & Hillenbrand (2008) considered the trends between the mean $\mathrm{R'_{HK}}$ and colour for stellar samples of known age, observing that it varies with ages. They calibrated the activity-rotation and rotation-age correlations and predicted the evolution of $\log \mathrm{R'_{HK}}$ as a function of age and colour for solar-type stars (see Figure 1.3, left panel). Unfortunately, the connection between activity and colour is not well parameterised yet, and could impact on calibration of $\mathrm{R'_{HK}}$ as an age estimator. However, they provided an improved $\log \mathrm{R'_{HK}}$ vs. age relation for solar-type stars:

$$\log \tau = -38.053 - 17.912 \log \mathrm{R'_{HK}} - 1.6675 \log(\mathrm{R'_{HK}})^2$$

where τ is the age in years and where the fit is only appropriate between -4.0 and -5.1. They argue that, for young stars recently arrived on the MS (e.g., the Pleiades), $\log \mathrm{R'_{HK}}$ is not

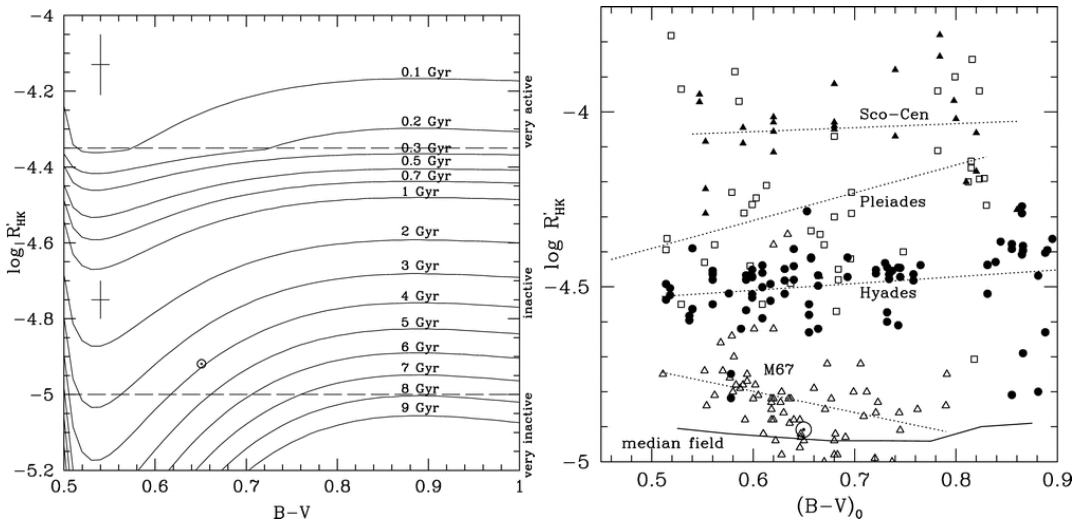

Figure 1.3: $(B-V)_0$ vs. R'_{HK} for members of several stellar clusters (left). Predicted chromospheric activity levels as a function of age (right). From Mamajek & Hillenbrand (2008).

very useful because of it large RMS which amounts to an order of magnitude. As stated by White et al. (2007), and reference therein, while R'_{HK} values have been shown to correlate with stellar age, this diagnostic typically has not been used to estimate ages less than ∼100 Myr, probably due to the lack of R'_{HK} measurements for stars in young clusters of known age.

Soderblom (2010) state that the HK measures in young (<500Myr) clusters show a wide range of values, related to spread in rotation, and this exceeds the difference in cluster averages. For this reason there is an overlap in apparent age for stars with the same level of chromospheric activity. As for rotation, this scatter is quite absent in the Hyades and it is assumed to reflect the convergence in rotation. On the other hand, for older stars (>0.5 Gyr) the relation of Mamajek & Hillenbrand (2008) seems to estimate the ages of solar-type dwarfs to roughly ±0.25 dex accuracy, even if not taking into account for colour-dependent evolution effects that seems to be present. One can therefore conclude that, following their prescriptions, the open clusters that supports a strict monotonicity of the chromospheric activity time evolution are the one in the age range from the Hyades to the Sun.

1.4 Motivation of this work

As discussed before, the determination of the age is important for studying stellar evolution. The purpose of this thesis is to characterize the NGC2516 and NGC3766 open clusters, studying in particular the chromospheric activity of NGC2516 and the lithium abundance of both clusters.

NGC2516 is a quite well studied open cluster, with an age slightly older than the one of the Pleiades (Jeffries et al., 1998). For this reason it can be used to verify if there is a scatter

in the $\log R'_{HK}$ versus $B - V$ for cluster of this age, as states by Mamajek & Hillenbrand (2008), considering that, up to now, the chromospheric activity in the CaII H and K for the stars of this open cluster has not been measured yet. Furthermore, the analysis of the lines in the continuum region near the CaII H and K features has never been done. Therefore, I tried to determine the physical parameters of the cluster's stars by measuring the equivalent width of some suitable lines and comparing them with theoretical models. This region of the spectra is very difficult to study, since, due to the presence of a very large number of absorption lines, the continuum level is suppressed to a pseudo-continuum. This aspect will be discussed, showing that the use of lines in this region is not convenient, due to different problems.

NGC3766, instead, is a very young cluster, still yet in the PMS and not well studied, and the analysis of the lithium abundance in this PMS cluster will provide more information about its age.

Chapter 2

Chromospheric activity in solar-like stars

The low intensity of the radiation received from stars limits somehow our information on them. The Sun, on the other hand, gives us the opportunity to obtain detailed information about its atmosphere, and allow us to test models that can be applied more generally to solar-like stars.

Since one of the main subjects of this thesis is the study the chromospheric activity in late type stars, I need to define what the chromosphere is and how it can be explored. The chromosphere is an intermediate region in the star's atmosphere lying above the photosphere and below the corona. In the case of the Sun, the solar atmosphere can be divided into different parts: the *photosphere*, the visible surface of the Sun, that is the layer below which the Sun becomes opaque to visible light; the *chromosphere*, a region extending some 2,500 Km above the photosphere (between the photosphere and the chromosphere there is a region called "temperature minimum region", in which the temperature is about 4,500 K, where the temperature grows slowly); the *transition region*, in which the temperature rises rapidly from around 100,000 K to coronal temperatures; *the corona*, that is the hotter part of atmosphere of the Sun and have a temperature of several million of K; the *heliosphere*, that extends from approximately 20 solar radii (0.1 AU) to the end of the solar system.

For decades, a lot of studies have been made to understand the fundamental mechanisms of magnetic activity, that are responsible of the temperature gradient inversion observed in the Sun and active stars. Since the stars are too distant to be resolved, these studies are based on the analysis of specific lines that can be defined as "indicators" of magnetic activity.

In the first two sections of this Chapter I will describe the structure of the solar chromosphere and the solar type activity; in the third section I will concentrate on the chromospheric models and on the chromospheric indicators, considering the connections between them; in the fourth section I will finally concentrate on chromospheric activity indicators from the

CaII H and K line.

2.1 Solar chromosphere

In Figure 2.1(a) is shown the chromospheric network in the ultraviolet line of calcium. The network outlines the supergranule cells and is due to the presence of magnetic field lines, that are concentrated there by the fluid motions in the supergranules. In Figure 2.1(b) are shown filaments and plages in H_α. The filaments are dark features seen in H_α, that are dense and cool clouds of material, suspended above the solar surface by loops of magnetic field. Plages are bright regions surrounding sunspots and form a part of the network that characterize the chromosphere. In Figure 2.1(c) are shown prominences or filaments in H_α. The prominences are filaments seen projecting out above the limb, or edge, of the Sun. In Figure 2.1(d) are shown spicules in H_α, that are small, jet-like eruptions seen throughout the chromospheric network.

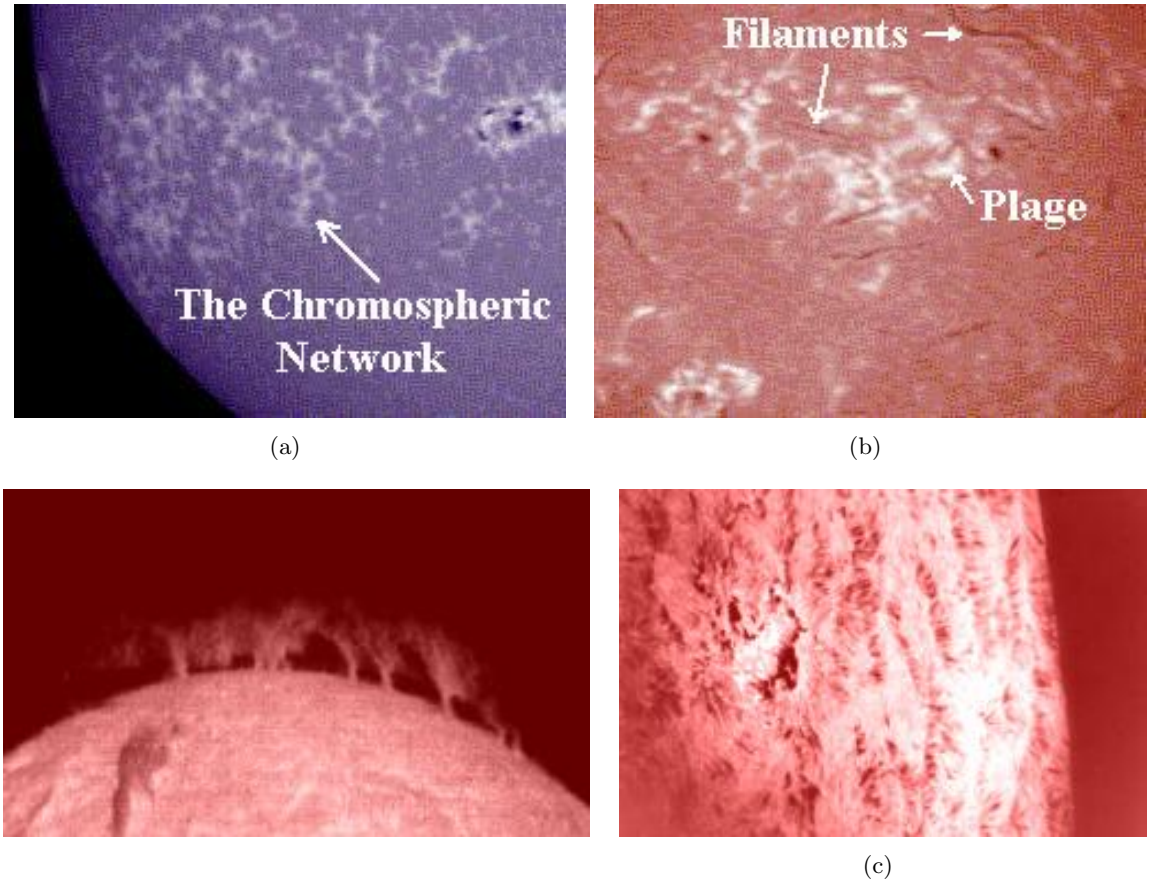

Figure 2.1: (a) The Sun chromosphere viewed in the light emitted by ionized calcium, CaII, at a wavelength of 3934 Å (K-line). The presence of the chromospheric network is evident. (b), (c) and (d): The Sun chromosphere viewed through a filter that isolates the H_α emission (6563 Å). There are shown respectively filaments and plages, prominences and spicules. The images are from NASA website (`http://solarscience.msfc.nasa.gov/chromos.shtml`).

The temperature distribution of the chromosphere is shown in Figure 2.2. As it can be seen, the temperature declines through the photosphere to a height of about 500 km, reaching the temperature minimum, then rises slowly to about 8000 K at 2000 km, and after rises sharply. The chromospheric temperature rise is revealed by the core of the CaII H and K lines, and much more strongly in the h and k cores of MgII. This is due to the Mg abundance fifteen times higher, that makes the h and k lines more opaque than H and K, and less sensible to departures from LTE (Local Thermodynamic Equilibrium) at the base of the chromosphere, and thus display the temperature rise more clearly (Hall, 2008). The

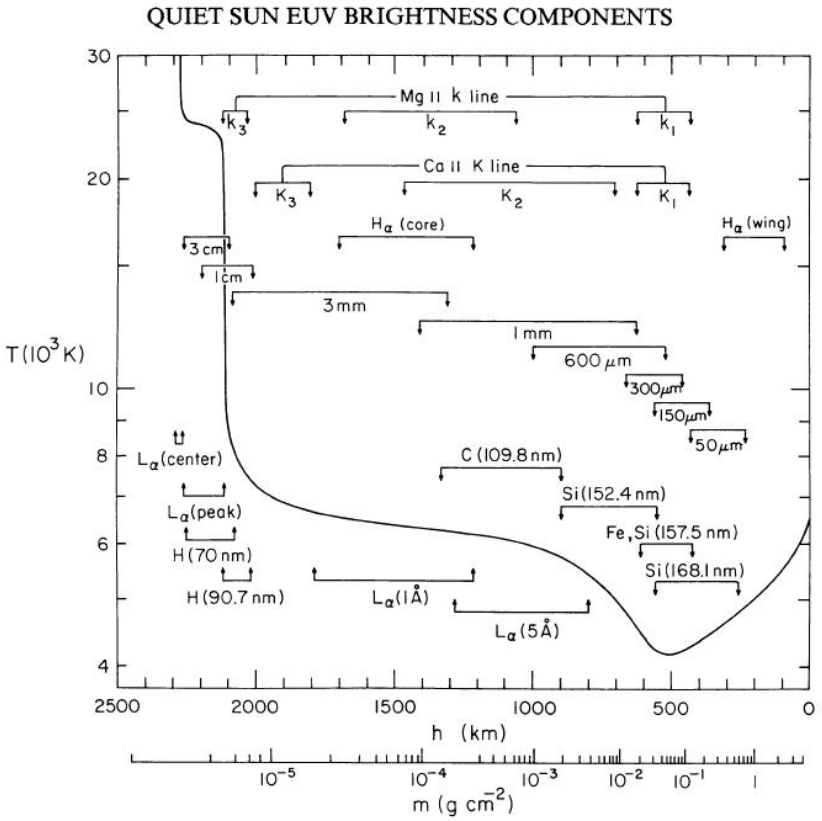

Figure 2.2: The model VAL III C temperature distribution from Vernazza et al. (1981). The solar chromosphere lies between the temperature minimum at right and the rapid rise toward transition region and coronal temperatures at ≈2300 km. On the right there is the photosphere; the chromosphere is between $h = 500 - 2,000$ km and then the temperature increase above $h = 2,000$ km, in the transition region.

structure of the temperature minimum region can be determined by the spectra in three wavelength regions: (1) the Si and Fe continua in the UV range 150-180 nm, (2) the 50-300 μm microwave continuum and (3) the K_1 and k_1 (and the H_1 and h_1) minimum features in the wings of the CaII and MgII lines (Vernazza et al., 1981).

The energy transport through the plasma, in a stellar atmosphere in radiative equilibrium (RE), occurs by radiation and any absorption is balanced by emission. In solar-like stars, there are some phenomena, due to the magnetic fields and their interaction with rotation, that

release mechanical energy into the atmosphere overlying the photosphere, causing heating beyond the expected RE values. The plasma balances this amount of energy increasing hydrogen ionization fraction, such that the temperature rise from ≈ 5000 K to ≈ 8000 K. Once hydrogen is fully ionized, the plasma loses this cooling mechanism and the temperature rises rapidly to coronal temperatures (Hall, 2008). The detail of thermal models of chromosphere, from which Figure 2.2 is derived, will be discussed in section 2.3.1.

2.2 Background of solar type activity

Manifestations of solar-like activity in main sequence stars are rather numerous and various. There are non-stationary phenomena, such as flares, involving all layers of stellar atmospheres, or other manifestations, such as cool spot on the stellar surface and the variability of large scale structures of stellar atmospheres, chromospheres and coronae. Moreover, there is the evidence of long term cycles of stellar activity, similar to the 11-year solar cycle. All these features are determined by the presence of magnetic fields, that controls both the structure and dynamics of the atmospheric plasma. The engine of solar-type activity is associated to subphotospheric convective motions. Convection and rotation lead to a differential rotation regime that is responsible of the magnetic dynamo. This one operates at the bottom of the convective zone and modifies the poloidal field into toroidal field, giving origin to a complex phenomenology of typical solar-type active regions, such as spots, plages and flares.

The stars in which this kind of activity can be found are primarily cool stars (see also Figure 2.3), because the magnetic and non-magnetic sources of activity need the presence of a convective zone, that has a critical role in maintaining the magnetic dynamo. The variation of energy output of the Sun and its activity have been monitored during the years in great detail, showing the presence of the typical solar phenomena. But while the existence of a solar activity has long been known, the discovery that such activity occurs also in other stars is quite recent (such as the observative survey of Olin Wilson and collaborators in the sixties). Since it is a manifestation of the interaction between plasma motions and magnetic fields and it is strictly connected to the presence of a convective zone, the stellar magnetic activity seems to take place in all cool stars.

Along the main sequence, magnetic activity is indeed found all the way down from the F-type stars to the coolest M-type stars (Figure 2.3). A convective envelope turned out to be a necessary condition, because indications for magnetic activity are exclusively found in stars with convective envelopes, including PMS stars, such as the T Tauri stars (Schrijver & Zwaan, 2000).

Activity of cool stars is usually attributed to temperature gradients generated by nonra-

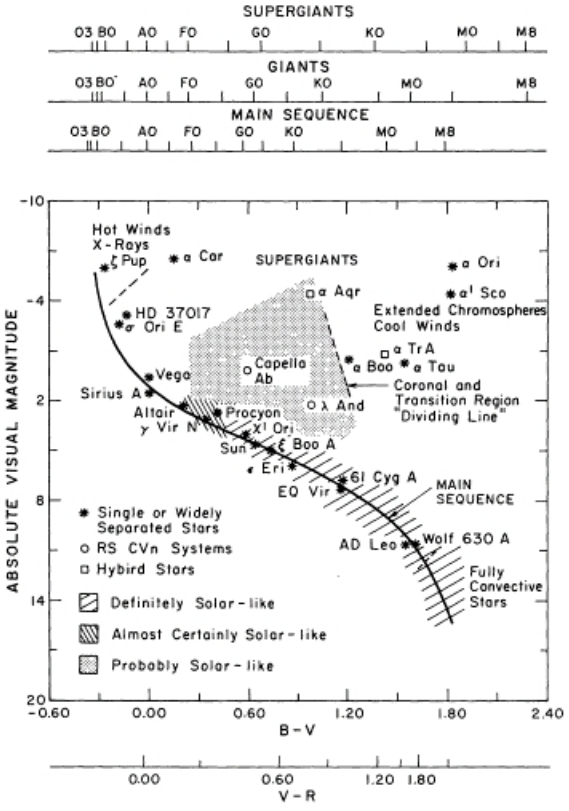

Figure 2.3: HR diagram showing stars with magnetic activity. The regions of HR diagram where massive winds occur and hot plasma is apparently absent are also indicated. Some frequently studied stars (both magnetically active and non active) are identified by name. From Saar & Linsky (1985).

diative heating. A possible mechanism of chromospheric heating is due to magnetic energy fluxes (Narain & Ulmschneider, 1996; Rutten et al., 1991; Ulmschneider et al., 2001; Fawzy et al., 2002). The generation of magnetic fields within a star with a subsurface convection zone is ascribed to a solar-type dynamo mechanism induced by rotation. Thus, both stellar rotation rate and convective zone depth are expected to influence stellar surface magnetic activity.

The rotation rate in late-type stars moderates the dynamo mechanism, which generates and amplifies the magnetic field in the convection zone. Furthermore, the presence of stronger emission in stars which rotate more rapidly is also a clear evidence of the relation between rotation and activity. It follows that, the determination of stellar rotation is important in testing the dynamo theory and in general to understand the magnetic activity of stars and that one can divide in "active" and "quiet" due to the different characteristics of the magnetic field that influence the structure of chromosphere and corona. The strong emission observed generally in H and K, in the case of stars which rotate more rapidly, can be explained by the Ω-effect of the classic $\alpha\Omega$ dynamo. If stars are rotating very slowly, the residual chromospheric emission is non-magnetic and they show a low level of surface magnetism. On the other

hand, if their rotation is faster, the chromospheric emission is due to the magnetic-associated heating (Noyes, 1983).

During its lifetime, a star loses mass, which streams away along the magnetic field lines, just like the Sun loses mass with the solar wind. Conservation of angular momentum implies that the rotation rate of the star decreases with age: the older the star, the less active it is (Skumanich, 1972; Noyes et al., 1984; Baliunas et al., 1995).

As was shown by Wilson (1963), the average intensity of CaII emission in a late-type dwarf has an inverse relationship to its age. Skumanich (1972) quantified the chromospheric activity in G stars, using both rotational velocities and CaII emission decline, demonstrating that this is proportional to the rotation rate:

$$\mathrm{v}\sin\mathrm{i} \propto \mathrm{t}^{-1/2}$$

Noyes et al. (1984) found that the chromospheric emission of cool stars, expressed as a fraction of the bolometric luminosity, is correlated with the inverse of Rossby number, defined as the ratio between the rotation period and the convective turnover time at the base of the convective zone:

$$\mathrm{R_o} = \mathrm{P_{obs}}/\tau_\mathrm{c}$$

where $\mathrm{P_{obs}}$ is the period and τ_c the convective turnover time.

Vaughan & Preston (1980) discovered that the overall distribution of chromospheric HK fluxes in the Mt. Wilson Observatory (MWO) sample shows an interesting bifurcation in the activity level, known as the Vaughan-Preston Gap (Figure 2.4). It was interpreted as a changing in dynamo behaviour between young and old G stars. The CaII H and K lines emission seems to decreases for $\mathrm{B}-\mathrm{V} < 0.45$, but Hartmann et al. (1984) state that is not a real gap, due to an upper limit to emission, coupled with a photospheric emission measured by the S index of F-G stars. They interpreted the break in chromospheric activity as a fluctuation in the local stellar birthrate, so that the gap depends from a slowly varying star formation rate. Vieytes & Mauas (2004) thought that the existence of the VP gap is not related to a discontinuity in the response of activity due to rotation or age, or of the rate of star formation in the past, but to the response of the CaII line emission to chromospheric heating. The assumption if the VP gap is real or not, and if so, its implications for the evolution of the magnetic dynamo that drives chromospheric activity, has been studied in terms of the Rossby number. Even if Noyes et al. (1984) and Hartmann et al. (1984) assumed that is not real, the gap appears in surveys employing both $\mathrm{R'_{hk}}$ (Henry et al., 1996; Gray et al., 2006) and absolute flux (Hall et al., 2007) and seems to be a real aspect of chromospheric activity in Sun-like stars.

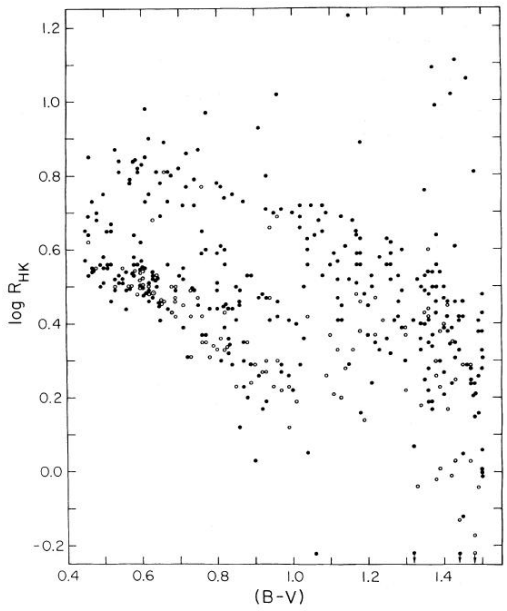

Figure 2.4: The chromospheric emission-colour diagram for stars within 25 pc from the Sun, based on the data of Vaughan & Preston (1980) combined with Middelkoop (1982) flux calibration. R_{HK} is the CaII H and K surface flux, measured with respect to the stellar surface flux. The VP-Gap is evident in the region between 0.5 and 0.7 $\log R_{HK}$ and $B - V$ between 0.8 and 1. From Hartmann et al. (1984).

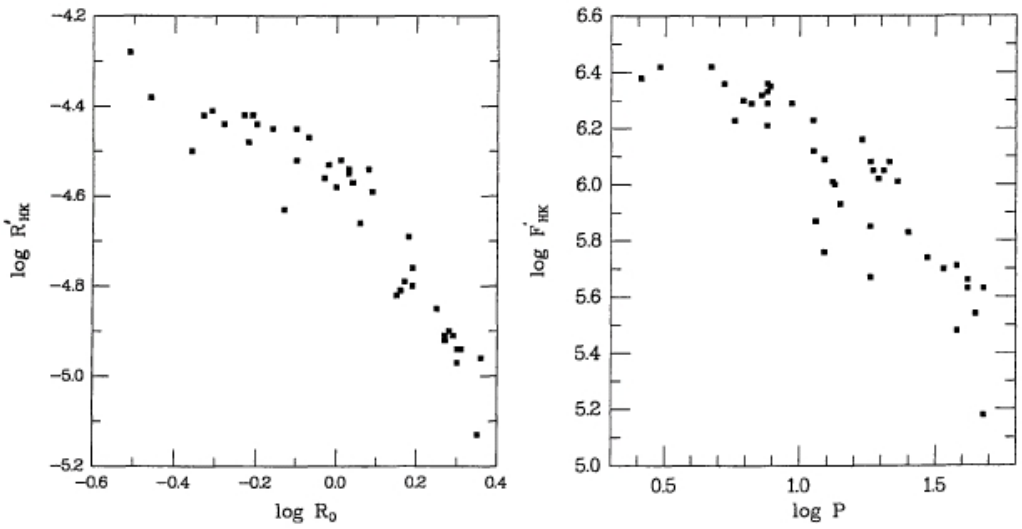

Figure 2.5: CaII chromospheric flux R'_{HK} on Rossby number, and CaII surface flux F'_{HK} on stellar rotational period P. From Noyes et al. (1984).

Since understanding of the dependence of magnetic field generation on global parameters can be only obtained only from the systematic study of many objects, the use of an extensive sample of stars of stellar clusters of different ages could provide key constraints for stellar and solar dynamo theory.

2.3 Chromospheric activity indicators

A chromospheric indicator represents a diagnostic of a particular region of the chromosphere whose variations are connected to the changes of the chromosphere properties in that region.

The CaII resonance lines H (λ 3968 Å) and K (λ 3933 Å) and the MgII resonance lines h (λ 2803 Å) and k (λ 2796 Å) have been traditionally used as diagnostics of luminosity and chromospheric activity in cool stars. Other useful indicators of chromospheric gas include the lines of HI (in particular the H_α at 6563Å), the infrared triplet lines ($\lambda\lambda$ 8498, 8542, 8662 Å) of CaII, the HeI lines (λ5876 and λ10830 Å) and the ultraviolet resonance lines of OI, CI, CII and SiII (at $\lambda\lambda$ 1814, 1264 Å).

Before the advent of space-based astronomy, the lines used to explore the nature of stellar chromospheric activity were limited to optical and near-UV resonance lines, but, fortunately, the most prominent and well-studied of these, such as the H and K lines of CaII or the H_α, provided a good base for the theoretical models.

Collisionally dominated lines such as CaII H and K reflect the local plasma conditions since collisional processes are tied to the local electron temperature. This is manifested in the emission reversals in the line cores, which for the H and K lines are formed high in the chromosphere. Neutral metals in general reflect the continuum radiation via the control of their source functions by radiative terms, and show no such reversal (Hall, 2008). The H_α line, whose core is formed high in the chromosphere, is marginally controlled by photoionization in Sun-like stars (Jefferies & Thomas, 1959; Fosbury, 1974), but during flares, and in extremely active stars, the collisional terms become increasingly important and it begins to fill in or goes into emission.

In the following sections I will consider the chromospheric models developed during the years and how can be obtained information about the chromospheric activity analysing the emission in lines formed in the chromosphere, such as the MgII lines, the H_α and the lines of CaII.

2.3.1 Chromospheric models

The models used to describe the chromosphere differ from physical and empirical ones. With the term *physical model* is intended a model which include enough physical processes to allow extrapolation from the data, so it is predictive. In this kind of model one must first identify the major energy mechanisms and then describe the transport processes. The *empirical model*, instead, put together the data with suitable diagnostic tools and transform the data prescription into physical variables. An atmosphere model have the purpose to provide

a deduction from data about the properties of the star (Athay, 1981). A way to treat the problem using both approaches is then to use a so-called *semiempirical model*, where parameters are varied until the results show a good accordance with empirical observations. It tends to reproduce as close as possible the observed data and perform an analysis of the physical processes that play an important role in the energy transport and in the determination of atmospheric structure. This kind of model began to emerge in the 1970s as development of the work on the solar CaII line. As described in, e.g., Lanzafame (1995), a scheme for obtaining a semi-empirical model is:

1. choose an appropriated model photosphere for the given spectral type and luminosity;
2. define a temperature distribution for the chromosphere to juxtapose onto the top of the photospheric model;
3. solve the equations of statistical equilibrium, radiative transfer and hydrostatic equilibrium for the defined temperature profile;
4. adjust the chromospheric temperature to agree with the observations.

Based on these assumptions, the first models of the solar chromosphere were one-dimensional, static, semiempirical models that list the stratifications of temperature and gas pressure. In the chromosphere, unlike the photosphere, where the plasma conditions can be determined assuming LTE, the photon mean free path increases so much that the assumption of LTE is no longer valid. The study of the line source function led to the development of the NLTE (non-LTE) chromospheric models, such as the model of Vernazza et al. (1973, 1976, 1981), to be adapted to particular conditions such as plages, the average quiet Sun, and so on. The VAL models (from the name of the authors) and their revisions are still frequently used.

The semiempirical VAL III model of Vernazza et al. (1981) is build to fit the observed profiles of a large number of spectral lines and the continuum. No hypotheses are made about the process responsible for the observed phenomena, but this modelling indicates only the general trend of the temperature and represents different brightness components of the solar chromosphere (quiet cell, magnetic network and active regions), in particular the average quiet Sun model VAL III C. The various radiative loss contributions of lines and continua have been computed by using an equivalent two-level radiative transfer code called PANDORA (Avrett & Loeser, 1992) that consider a one-dimensional atmospheric region that is either finite or seminfinite in the plane parallel case, or that has spherical symmetry. Then hydrostatic equilibrium and pressure equilibrium are assumed and a new temperature distribution is determined from the energy balance constraint together with a density distribution. When

these ones are known, the NLTE energy level population of various atoms and ions are calculated.

Subsequently, a multilevel radiation code called MULTI, based on the complete linearization method, was developed by Carlsson (1992). It is calculated from a small set of free parameters (the effective temperature, the acceleration of gravity and the chemical composition), by solving the appropriate equation describing the physics of stellar atmosphere and assuming to use a given temperature structure, a one-dimensional atmosphere and the mass density as function of height. Finally the statistical equilibrium and the radiative transfer equations are simultaneously solved for all the lines and continua.

It is clear that a one-component models could not explain the complexity inhomogeneous nature of the chromosphere, and it should be better described with a three-component model, but this is still well beyond the current computational capabilities. Typical semiempirical model are also the Stellar Model Chromosphere series of Jeffrey Linsky (such as Ayres et al. (1974) and Ayres & Linsky (1975) and subsequent articles) that provided a description of the stellar atmospheric structure, together with a study of the radiative losses in active chromosphere stars.

Most of the model for non-magnetic and magnetic regions, considered the radiative losses only in a single line and then scale up with correction factors to account for the full radiative losses. These correction factors were originally obtained by using the results of the VAL III model, where is defined a net cooling rate for continua, given by:

$$\Phi_{\mathrm{m}} = 4\pi \int_{\mathrm{m}} \mathrm{k}_{\nu} \left(\mathrm{S}_{\nu} - \mathrm{J}_{\nu}\right) \mathrm{d}\nu \tag{2.1}$$

where k_{ν} is the continuous, S_{ν} the source function and J_{ν} the mean intensity of radiation. A positive value of Φ implies a net loss of energy (cooling), and a negative value represents a net energy absorption. For a spectral line the Equation (2.1) becomes:

$$\Phi_{\mathrm{ul}} = \mathrm{h}\,\nu \left[\mathrm{n_u} \left(\mathrm{A_{ul}} + \mathrm{B_{ul}}\bar{\mathrm{J}}\right) - \mathrm{n_l}\mathrm{B_{lu}}\bar{\mathrm{J}}\right] \tag{2.2}$$

where $\mathrm{n_u}$ and $\mathrm{n_l}$ are the upper and lower levels of number densities, $\mathrm{A_{ul}}$, $\mathrm{B_{ul}}$ and $\mathrm{B_{lu}}$ are the Einstein coefficients and $\bar{\mathrm{J}}$ is:

$$\bar{\mathrm{J}} = \frac{\int \mathrm{k}_{\nu}\mathrm{J}_{\nu}\mathrm{d}\nu}{\mathrm{k}_{\nu}\mathrm{d}\nu} \tag{2.3}$$

The Equation (2.2) also can be written as:

$$\Phi_{\mathrm{ul}} = \mathrm{h}\,\nu\,\mathrm{n_u}\,\mathrm{A_{ul}}\,\rho \tag{2.4}$$

where ρ is given by:

$$\rho = 1 - \frac{\bar{\mathrm{J}}}{\mathrm{S^L}}$$

S^L represent the line source function that describes the ratio of the emission coefficient to the absorption coefficient. It is a measure of how photons in a light beam are removed and replaced by new photons by the material it passes through and depends on the number densities and the statistical weights, and it is connected with $\bar{J}$.

Considering the net cooling rates per unit volume in Figure 2.6, one can see that the hydrogen, expecially the Ly_α, gives an high cooling rate, since it is dominant in the transition region at temperature between 2×10^4 and 3×10^4 K. Normally, the Ly_α net radiative cooling

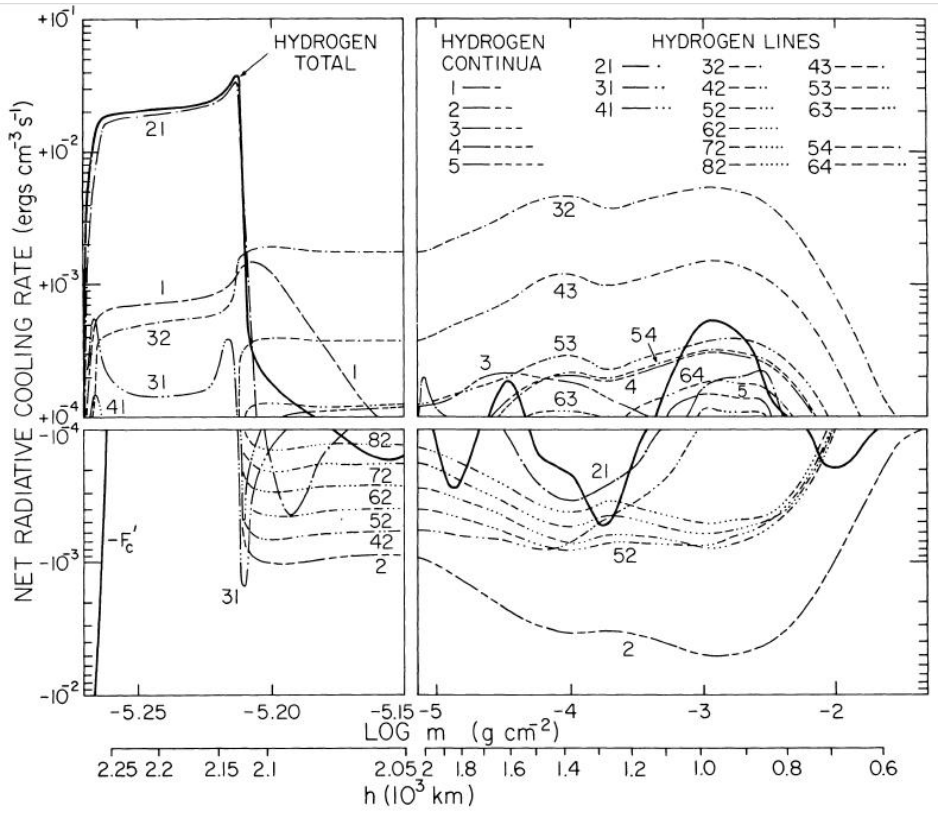

Figure 2.6: Net radiative cooling rates for hydrogen from the model VAL III C. The transition region (left) is dominated by radiative cooling in Ly_α (label 21). The solid curve is the combined net cooling rate in all HI lines and continua. From Vernazza et al. (1981).

rate is positive, so that the number of Ly_α photons emitted by the gas exceeds the number of photon absorbed at the same depth. In the transition region, the gas is heated by net absorption of Ly_α radiation, due to the higher temperature. The Ly_α heating mechanism may play a role in the transfer of energy from the corona to the upper chromosphere. Some of this energy could reappear in other hydrogen transitions, either to heat the gas radiatively or to offset other radiative cooling losses.

In VAL III C model, the thermal conduction from the corona become ineffective for transition region temperature below 2.5×10^4 K. Ly_α absorbs energy from the corona down to the plateau region, and then deposits part of this energy in the chromosphere by radiative

heating, that is lower than the Balmer continuum radiative heating. The net radiative rates for the Balmer continuum and the H_α line have approximately the same absolute value but opposite sign, and the net emission in H_α is balanced by net absorption of photospheric radiation in the Balmer continuum. Part of the absorbed energy is then carried by thermal conduction from the corona to the lower levels. However, H^- cooling rate is less than the contributions due to the CaII lines in the low chromosphere (the H^- bound-free cooling rate is comparable to the H^- free-free cooling rate). The net radiative heating by H^- and CaII and MgII lines is negative in the temperature minimum, due to their omission of numerous weak atomic and molecular lines. The maximum near 800 Km in the low chromosphere and its gradual decrease with height is due fundamentally to the CaII and MgII lines emission. The negative values at the temperature minimum can be explained by the presence of prominent lines of molecules such as carbon monoxide or due to the waves motion that remove energy (Avrett, 1985) (Figure 2.7). In the next sections I will show in more detail the lines most used to study the chromosphere.

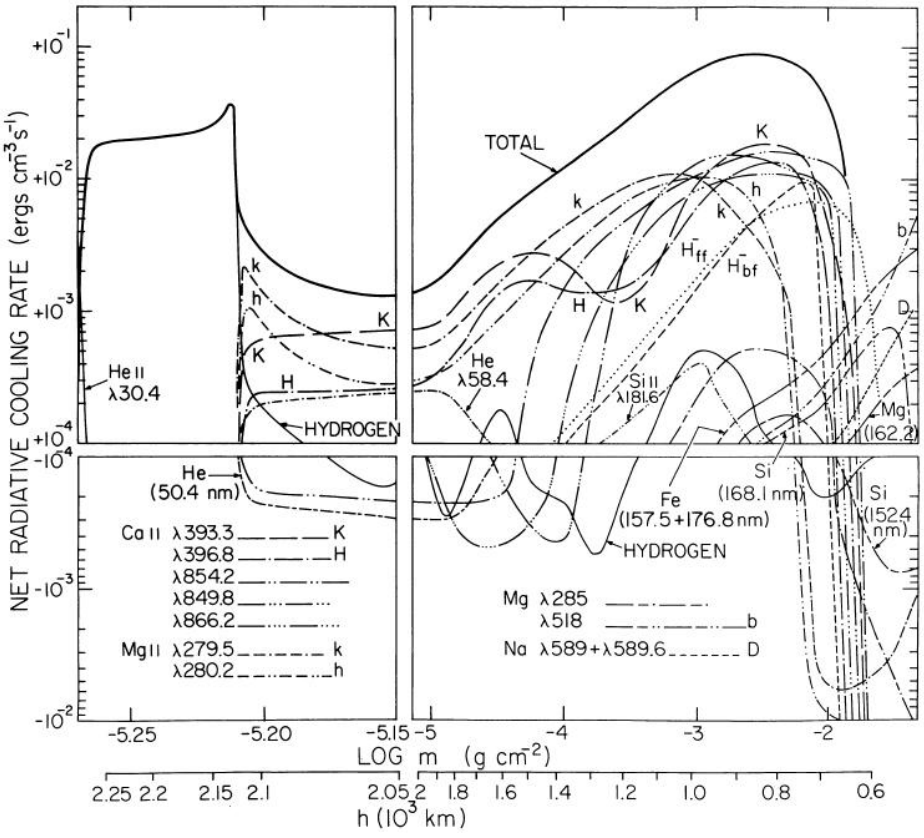

Figure 2.7: Net radiative cooling rates for CaII, MgII, H, H^- and other constituents from the model VAL III C. The curve marked HYDROGEN is the combined net cooling rate in all HI lines and continua shown solid in figurename 2.6. The solid curve marked TOTAL specifies the total radiative losses of the VAL III chromosphere at every height. They are dominated by the MgII h and k and CaII H and K resonance lines over most of the chromosphere. In the temperature minimum region ($\sim$ h = 500 km) these lines are net heaters. From Vernazza et al. (1981).

2.3.2 MgII h and k lines

The MgII h and k resonance lines are formed at higher temperatures and greater heights than the CaII lines, and their appearance are similar. The MgII doublet arises from transitions between the 3^2P levels and the ground state 3^2S. Thanks to the large abundance of magnesium in cool stars, they are also good indicators of the total chromospheric radiative loss and of heating of the thermal structure of stellar atmospheres, especially from the high photosphere to the upper part of the chromospheric plateau (Linsky & Ayres, 1978).

In the solar case, the MgII core-to-wing ratio defined by Heath & Schlesinger (1986), has become a valuable index of variability of the chromospheric radiation. In order to connect stellar and solar observations, Cerruti-Sola et al. (1992) compared IUE MgII profiles with some Skylab spectra of solar regions. They showed that different MgII emission levels observed in stars of similar spectral type are due to differing fractions of their surfaces covered by magnetic regions. In previous studies, it was found that the radiative fluxes of the CaII and the MgII lines are highly correlated among themselves (Oranje & Zwaan, 1985; Schrijver, 1987; Rutten et al., 1991). Using nearly simultaneous observations, Schrijver et al. (1992) derived a linear relationship between the MgII h and k fluxes (F_{MgII}), measured using IUE spectra, and the Mount Wilson CaII H and K fluxes (F_{CaII}).

2.3.3 H_α line

H_α (6562 Å) is one of the most prominent lines in cool stars' spectra. Besides being an important chromospheric activity indicator, it is also a good indicator of circumstellar emission and mass flow in late-type stars. Active stars have usually a less deep absorption in comparison with non-active stars, for example in the RS CVn, this line is emission. In G and K stars with moderate activity the formation of the Ha line is dominated by photoionization. In the atmosphere of more active stars the role of electron collision in the H_α formation increases. When H_α is in emission, like in dKe and dMe stars, it is also collisionally dominated. This condition is more easily reached towards later spectral types where the underlying continuum radiation field is weaker (Cincunegui et al., 2007).

The use of H_α as activity indicator is well studied (see, for example Montes et al., 1995b; Pasquini & Pallavicini, 1991). According to the solar-stellar analogy, chromospheric stellar activity can be established by the presence of emission in the core of the Balmer Hα line. As in the Sun, Hα emission intensification has often been observed in surface features (plages) spatially connected with the photospheric starspots (see, e.g. Biazzo et al., 2007, 2006, and reference therein). Thus, the time variability of the Hα spectral features can be used to estimate the basic properties of the emitting sources, allowing the mapping of the stellar

chromosphere. The H_α core emission is usually determined by subtraction of the EW of an inactive star with the same spectral type and luminosity, or a synthetic spectrum (Figure 2.8). It has been claimed that a strong correlation exists between H_α and the CaII lines (Giampapa et al., 1989; Strassmeier et al., 1990; Robinson et al., 1990; Montes et al., 1995b).

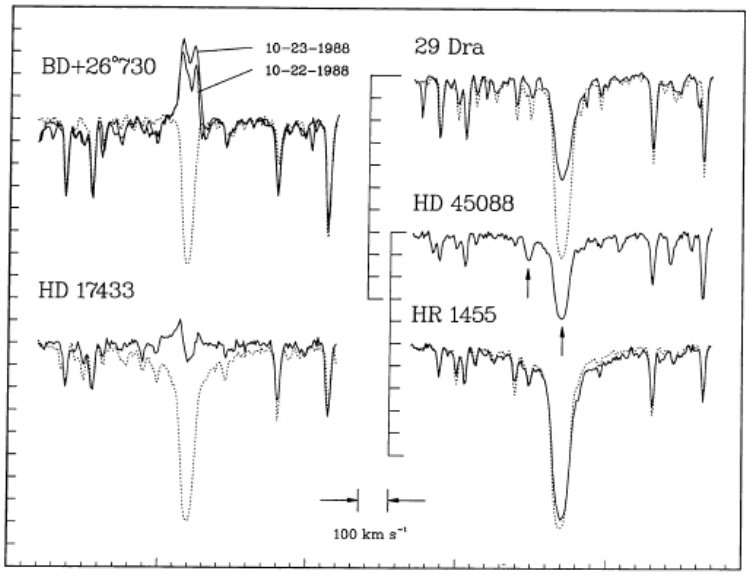

Figure 2.8: H_α profiles of five different stars. Each of them represents a typical example of a particular type of H_α profile. The dotted lines are spectra of reference stars of the same spectral type and luminosity class. HD17433 show a weak emission line with a strong superimposed absorption line. 29Dra shows a filled in absorption line profile. HD 45088 shows a filled in absorption line profiles in a double lines spectroscopy binary (the arrows indicate the two H_α lines). HR 1455 shows a composite H_α profile. From Strassmeier et al. (1990).

2.3.4 CaII IRT lines

The infrared triplet lines of CaII at $\lambda\lambda$ 8498, 8542, 8662 Å (hereafter CaII IRT), due to transitions between the upper 4p $^2P_{1/2,3/2}$ levels and the lower metastable 3d $^2D_{3/2,5/2}$ levels (Figure 2.9), are the most prominent features of the near infrared region of the spectra of G, K and M stars (Mallik, 1998). The same upper levels decay to the ground state 4s $^2S_{1/2}$ to give rise to the CaII H and K lines. Although the CaII IRT have the lower levels populated radiatively and are not collisionally controlled like the CaII H and K lines, they have been identified as very good luminosity probes. They are easy to observe even in faint stars because are intense and not contaminated much by the telluric lines (Mallik, 1997).

Several authors have underscored the diagnostic power of these lines as activity indicators. Linsky et al. (1979a) show that the radiative loss rates in the 8542 Å line are well correlated with radiative loss rates in the CaII H and K and MgII h and k lines. Montes et al. (2000), through the analysis of high resolution spectra of 16 chromospherically active binary systems, find that the CaII IRT lines turn out to be a very useful chromospheric activity indicator. All

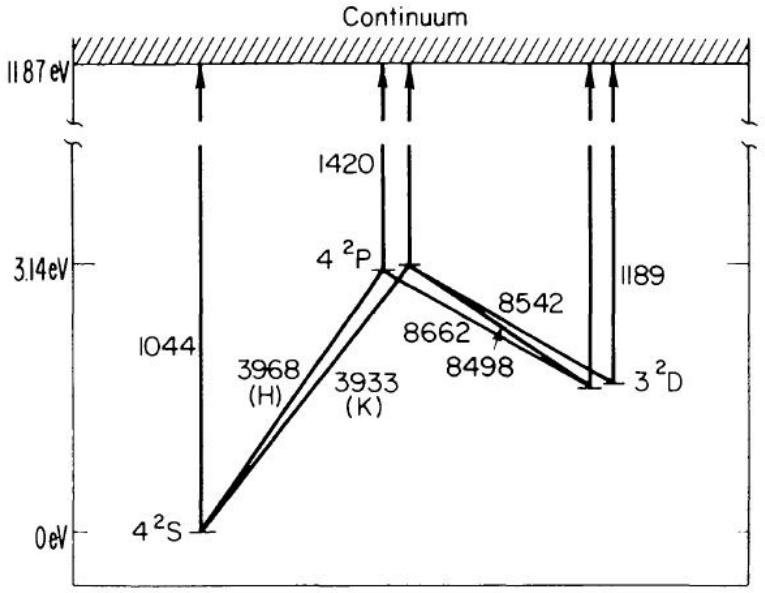

Figure 2.9: Energy level diagram for CaII. From Linsky et al. (1979a).

the stars considered show a clear filled-in absorption line profile or even notable emission reversal. Moreover, Chmielewski (2000), studied a sample of 40 stars, measuring the behaviour of the central depression (CD) of the 8542 line, founding a correlation between the observed CD and the classical chromospheric indicator. Subsequently, Busà et al. (2003) introduced two new activity indicators: The R_{IRT} index, given by difference between the observed CD and the theoretical NLTE profile CD, convolved for the rotation:

$$R_{IRT} \equiv CD_{conv}\,(NLTE) - CD_{obs}$$

and the core-residual EWs of CaII IRT, given by the area of the positive profile obtained as the difference between the theoretical profile and the observed one:

$$\Delta W_{IRT} = EQW_{NLTE-core} - EQW_{obs-core}$$

Moreover, the ΔW_{IRT} is almost linearly correlated with the excess in the CaII H and K doublet (see section 2.3.6).

2.3.5 CaII H and K lines

The strongest spectral features observable from the ground are the resonant lines of CaII, called H and K by Fraunhofer in 1814. They have been longer studied and are known to be good indicators for solar chromospheric activity. As seen in section 2.3.4, they are formed in the transition between the lower level $4^2S_{1/2}$ and the upper levels $4p^2P_{1/2,3/2}$ (Figure 2.9). The characteristic features of CaII K line are represented in Figure 2.10. The K_1 are the absorption minima of the CaII lines and are formed in the temperature-minimum region,

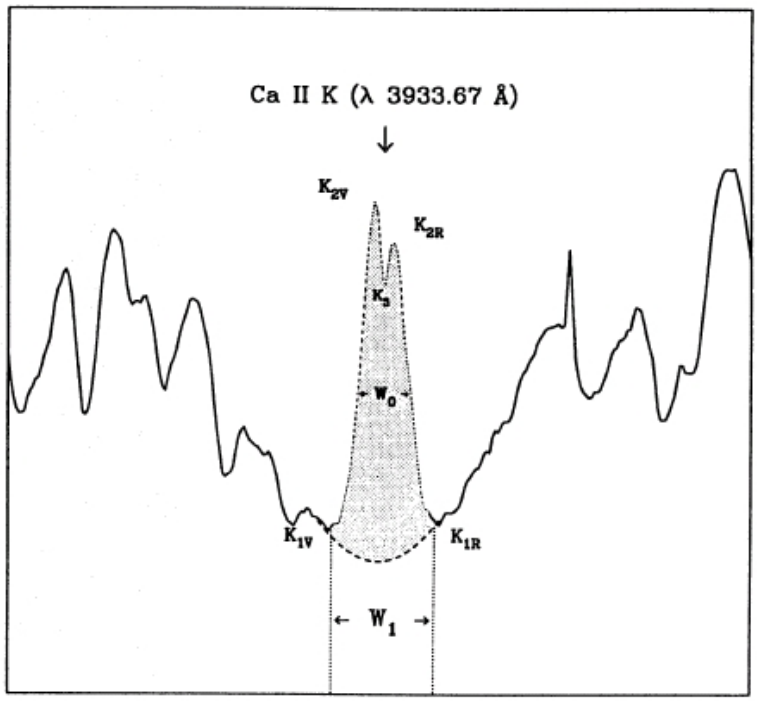

Figure 2.10: Characteristic features and widths of CaII K profiles. W_1 is the K_1 minimum feature separation; W_0 is the full width at half maximum. From Montes et al. (1994).

due to their large opacities. With K_{1V} and K_{1R} are indicated the K_1 minimum in the violet and red part of the spectrum. The emission maxima K_{2V} and K_{2R} are formed between the first chromospheric rise and the beginning of the chromospheric plateau. The absorption core K_3 is formed from the temperature plateau up to the transition region. The presence of emission in the core is a diagnostic of magnetic activity in the chromospheres of late-type stars (the region of chromosphere where these features are formed is shown in Figure 2.2). The central reversal in K_3 occur because the line center is formed high in the chromosphere, where the electron density is too small to maintain LTE, and photon scattering causes the line-center excitation temperature to be much smaller than the local kinetic temperature (Avrett, 1985). For these reasons, study the positions of these features allow us to measure the level of chromospheric activity in the stars analysed.

Observation in these lines date back to the beginning of the last century with the works of Eberhard & Schwarzschild (1913), who noted the presence of pronounced emission features in these lines in spectra of Arcturus and other stars. Afterward, an extensive collection of data on CaII emission have been obtained, mainly through the work of Olin Wilson and his collaborators. In 1966 Wilson began the program of monitoring the integrated H and K emission fluxes at MWO, in order to evidence the chromospheric activity in late-type stars (Wilson, 1978). Following Wilson's retirement, the so-called "HK Project" continued under the direction of S. Baliunas until the end of 2003, with the purpose of establishing a

solar-stellar connection.

The early Mount Wilson observations revealed a linear relation, called Wilson-Bappu relationship (Figure 2.11(a)), between the absolute magnitude and the logarithm of the K line emission widths for G and later stars, dwarfs, and giants alike:

$$M_V = 27.59 - 14.94 \log W_0(K)$$

The half-intensity width W_0 is correlated to the visual magnitude without dependence on intensity or spectral type, and this emission is greater in brighter stars. The separation between K_1 minima and K_2 maxima decreases to the increasing of K_3 central reversal, that is connected to the rise of activity level (Wilson & Vainu Bappu, 1957). Pace et al. (2003) suggested that this relation can be used to infer cluster distances, though it contains too much scatter to be useful for individual stellar distances.

Baliunas et al. (1998) found that 60% of stars in the MWO survey exhibited periodic, cyclic variations, 25% showed irregular or aperiodic variability and 15% had flat activity records (Figure 2.11(b)). This general distribution was also found in the more recently Solar-Stellar Spectrograph (SSS) program at Lowell Observatory(Hall et al., 2007).

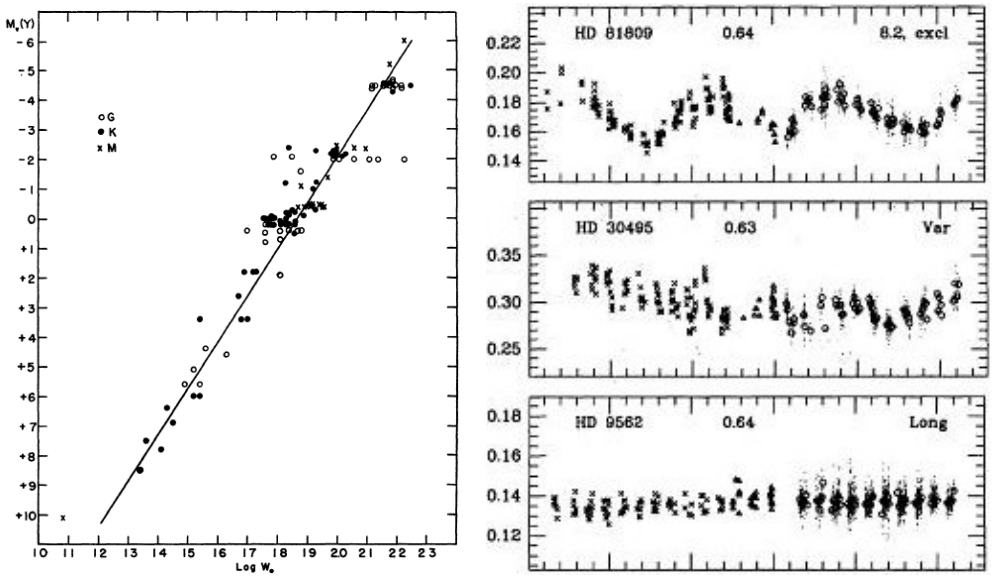

(a) (b)

Figure 2.11: (a) Wilson-Bappu effect: logarithm of CaII emission linewidth (abscissa) plotted against the Yerkey spectroscopic absolute magnitude. Stars are grouped for spectral type G, K or M. From Wilson & Vainu Bappu (1957). (b) Time series from the MWO HK Project, illustrating periodically variable (top), irregular (center), and flat (bottom) chromospheric activity, expressed in terms of the dimensionless S index (that will be defined in section 2.4), running from 1966 − 1991. From Baliunas et al. (1995)

2.3.6 Connections between activity indicators

During the years, different relationships have been found between the chromospheric indicators and since the most studied are the CaII H and K lines, the connection are usually referred to these ones.

The MgII h and k activity index in cool stars is found to be similar to the CaII one. This is because these lines form approximately in the same region. Their relation is of interest for the interpretation of the chromospheric and transition region fluxes. Oranje & Zwaan (1985) found a relation that connects the two fluxes:

$$\mathrm{F_{MgII}} = \alpha\,(\mathrm{F_{CaII}} - \beta(\mathrm{B-V}))$$

where α is a coefficient that does not vary too much with $\mathrm{B-V}$ and $\beta(\mathrm{B-V})$ is function of $\mathrm{B-V}$. This relation has also been studied by Rutten et al. (1991); Schrijver (1987); Schrijver et al. (1992). The main difference between the CaII H and K and the MgII h and k is that in the former the continuum is not negligible and the line absorption wings produces a minimum flux even without a chromospheric contribution, in the latter the underlying continuum is negligible and the measured flux originates almost exclusively in the line cores.

The H_α shows a relation between its chromospheric fluxes and that in the H and K CaII lines and usually their fluxes are used interchangeably as activity indicators. Most works where this relation has been observed (Strassmeier et al., 1990; Montes et al., 1995b; Robinson et al., 1990; Giampapa et al., 1989) found it by using averaged fluxes for both the calcium and the hydrogen lines, which were not obtained simultaneously, and were even collected from different sources. Thatcher & Robinson (1993), instead, used simultaneous observations, but they observed each star only once. More recently, Cincunegui et al. (2007) found a strong correlation between the mean fluxes of H_α and CaII H and K, for each star observed and concluded that this relationship is due to the dependence of the mean fluxes on stellar colours. They also discovered that in general the activity measured in H_α is not always equivalent to the one measured in the CaII lines for the whole sample of stars considered by them. Also for the CaII IRT, Busà et al. (2007) found that $\Delta\mathrm{W_{IRT}}$ is tightly correlated with $\log \mathrm{R_{HK}}$.

Since all the lines considered are formed in the chromosphere, it is evident that these indicators are related each other. However, since each one of them is formed in a different region with respect to the others, in different part of the spectrum, and gives different information, the choice of the appropriate indicator is strictly connected to what aspect of the chromosphere one decides to highlight. Furthermore, several studies (i.e., Rutten et al., 1991; Zwaan, 1991, and references therein) have shown that chromospheric emissions are also

strongly correlated to the coronal emissions for stars with spectral types from mid F to mid K. Main-sequence stars and evolved stars follow the same relationship between the stellar surface fluxes emitted in X-rays and in the CaII H and K line cores, independent of spectral type, provided that a minimum flux density (which depends on spectral type, and perhaps weakly on luminosity class) is subtracted from the observed value. Schrijver (1993) argues that the non-linearity of the stellar CaII - X-ray relationship is caused by the non-linear dependence of CaII K line-core emission on the mean magnetic flux density, as observed in solar active regions (Schrijver et al., 1989) and seen in model calculations by, e.g., Solanki et al. (1991), while the X-ray flux density is proportional to the magnetic flux density (Schrijver, 1987). Schrijver (1983) found a relationship between measures for coronal and chromospheric emission, independent of stellar parameters, and flux densities, using data of EINSTEIN/IPC and Mt. Wilson:

$$F_X \propto \Delta F_{CaII}^{1.67}$$

Finally, Mamajek & Hillenbrand (2008) have recently found a better relationship, using the chromospheric and coronal data of a sample of solar type stars with known rotation periods and chromospheric and X-ray activity levels, cross-correlating them (see Figure2.12) and leading to the relation:

$$\log R'_{hk} = (-4.54 \pm 0.01) + (0.289 \pm 0.015)\big(\log(L_X/L_{bol}) + 4.92\big) \tag{2.5}$$

that has been derived empirically and which can relate each other those quantities (L_X and R'_{hk} is adimensional and gives a measure, respectively, of the activity level in the corona and in the chromosphere, the meaning of the R'_{hk} and will be described in section 2.4.1). Specifically, the coronal and chromospheric activity indicators, which generally decline with advancing age, are either dependent on or constant with age for solar-type PMS stars (e.g. Mamajek & Hillenbrand, 2008).

2.4 CaII H and K lines indicators and their methods of measure

Since the Mt. Wilson survey, different authors studied the CaII H and K lines, providing different techniques to measure their emission. Each of these methods can be used separately from the others, having distinctive features and limitations that I will be described better in the following sections.

2.4.1 Mt Wilson method

The first index used to study the CaII H and K lines and the chromospheric activity, was introduced by Wilson (1968). He defined a dimensionless flux index F as the ratio of the sum

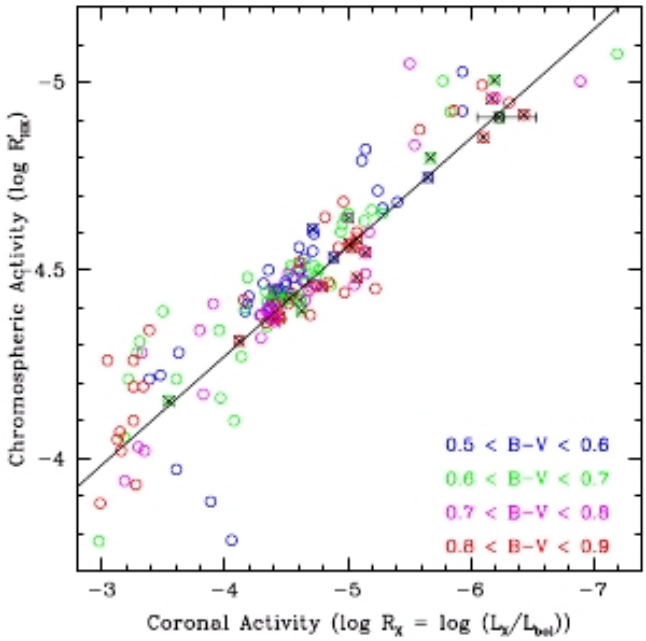

Figure 2.12: $R_X = \log L_X/L_{bol}$ vs. R'_{hk} for stars of solar-type stars with known rotation periods and chromospheric and X-ray activity levels. Different bin of $B - V$ have been considered. From Mamajek & Hillenbrand (2008).

of H and K line core flux to that in two nearby continuum bands, measuring that fluxes with a photometer called "HKP-1". Subsequently, the HKP-1 photometer was replaced in 1977 by the spectrophotometer "HKP-2", but both instruments measured activity in the same way and were satisfactorily cross-calibrated in terms of a new activity index S. The passbands of the H-K spectrometer has a triangular shape as function of wavelength, with a FWHM=1.09 Å, wide enough to admit all the chromospheric emission in the H and K lines but also to includes some flux of the stellar photosphere, in particular outside the H_1 and K_1 minima, as one can note in Figure 2.13. Using the stellar counts, Vaughan et al. (1978) introduced the

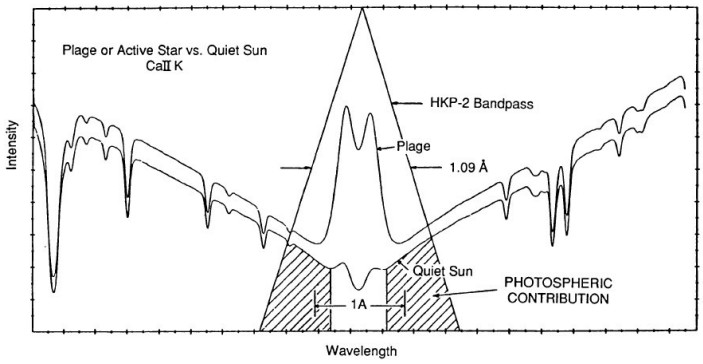

Figure 2.13: Triangular H-K photometer profile superimposed on profiles of the solar CaII K line for the quiet Sun and for a solar plage. From Duncan et al. (1991).

following quantities:

$$C_{RV} \equiv 2.5 \log_{10} \frac{N_R}{N_V} \tag{2.6}$$

and:

$$S \equiv \alpha \frac{(N_H + N_K)}{(N_V + N_R)} \tag{2.7}$$

where N_H, N_K,N_V and N_R refer to the number of counts, corrected with the respect to the background, in the H and K bands and in the reference bands on the violet and red side of the H-K regions (R-Band 4001.067-3991.067Å, V-band 3911.062-3891.067Å), and α is a normalising correction factor, derived for each observing night from the observation of standard stars to remove instrumental noise, that in their case was approximately 2.4. Then, S is a dimensionless ratio of the emission in the line cores to that in two nearby continuum bandpasses on either side of the H and K lines.

The C_{RV} ratio is useful as a colour index for some stars but not for others. Vaughan & Preston (1980) noted that in the plot C_{RV} vs. $B - V$ (Figure 2.14) the two quantities are

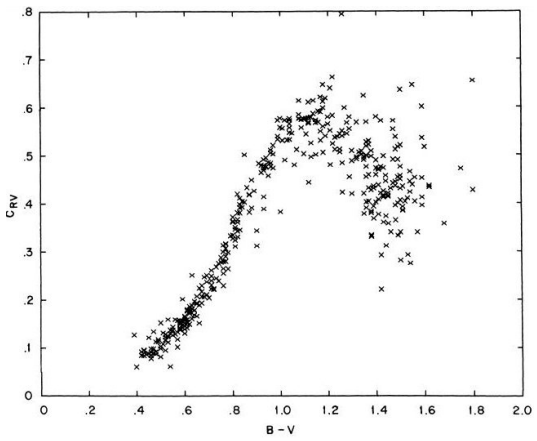

Figure 2.14: Relation between the C_{RV} index and $B - V$. From Vaughan & Preston (1980).

well correlated for $B - V \leq 1.0$, but for $B - V > 1.0$ the correlation is very poor and the red stars appear increasing blue (in terms of C_{RV}). This behaviour probably is connected to the line blanketing present in the coolest stars and suggest that S may not be a useful index for the red stars. The S index also includes a photospheric contribution in the line core bandpasses and depends on chromospheric radiation, but also on photospheric emission in the neighboring line wings, which is a function of spectral type, as pointed out by Hartmann et al. (1984). Middelkoop (1982) removed the colour term from S converting it into a physical quantity using a correction factor:

$$\log C_{cf} = 1.13 \cdot (B - V)^3 - 3.91 \cdot (B - V)^2 + 2.84 \cdot (B - V) - 0.47 \tag{2.8}$$

which depend only on $B - V$ (that works well for $0.45 \leq B - V \leq 1.5$):

$$R_{HK} = 1.340 \times 10^{-4} C_{cf} S \tag{2.9}$$

where R_{HK} is the fraction of stellar luminosity which appear as emission in the H and K lines and that is:

$$R_{HK} = F_{HK}/\sigma T_{eff}^4 \tag{2.10}$$

and F_{HK} represents the total flux per cm^2 at the stellar surface in the H and K passband. The function C_{cf} was determined from Mt. Wilson observations of stars in the solar neighborhood by comparison of the fluxes in the two "continuum" channels of the H-K photometer to the bolometric flux inferred from the measured colour of each star and its visual magnitude.

The triangular profiles used to integrate the line fluxes F_{HK} include some flux outside the K_1 minima, which is formed in the stellar atmosphere below the temperature minimum and that does not respond to the magnetic flux through the underlying photosphere. This flux of photospheric origin, usually indicated as F_{HK}^0, introduces a dependence on stellar colour and in order to obtain the net chromospheric line flux it has to be subtracted to F_{HK}, giving :

$$F_{HK}^{'} = F_{HK} - F_{HK}^0 \tag{2.11}$$

and the chromospheric flux ratio as:

$$R_{HK}^{'} = F_{HK}^{'}/\sigma T_{eff}^4 \tag{2.12}$$

$R_{HK}^{'}$ is proportional to that fraction of the nonradiative energy flux in the convective zone which is converted into chromospheric heating. The flux F_{HK} could be reproduced by residual H-K emission in stars whose magnetic activity is so low in order to contribute negligibly to the total observed H-K flux. However, even the most inactive stars still have some residuals chromospheric emission, then is better to subtract off the contribute of photosphere, leaving the chromospheric emission, that in the solar case is closely related to the surface magnetic flux. Moreover, for the Sun, the integrate emission intensity inside the K_1 minima closely approximates the total net radiative loss in the K line above the temperature minimum (Noyes, 1983; Hartmann et al., 1984; Noyes et al., 1984). Noyes et al. (1984) assumed that the photospheric contribution depends only on $B - V$, independently from chromospheric activity, in order to subtract the same value in all the stars with the same spectral type (assumption reasonable since the intensity increase in the wings is less than that of the line cores and that permit a simple derivation of the subtraction term).

The flux interior the H_1 and K_1 minimum give an estimation of the total radiative losses in the CaII lines. The subtraction of the photospheric contribution from the total H-K emission R_{HK} does not have a large effect for active stars, but is more important for less chromospherically active ones, where is necessary to carry out model chromosphere calculations.

2.4.2 Linsky's method

Unlike the bandpass method introduced by Wilson (1968) and his successors, Linsky et al. (1979b) used another method, reducing their spectra to relative intensities and then converting them to absolute surface fluxes, in order to compare the observation with lines profiles and line flux computed from chromospheric models of these stars. They wrote the stellar surface flux as:

$$\mathcal{F}(\Delta\lambda) = \mathrm{f}(\Delta\lambda)\left(\frac{\mathrm{d}}{\mathrm{R}}\right)^2 = \mathrm{f}(\Delta\lambda)\left(4.125\cdot 10^8/\phi'\right)^2 \tag{2.13}$$

where d is the distance, R is the stellar radius, $\mathrm{f}(\Delta\lambda)$ is the flux observed at Earth, and ϕ is the angular diameter in milliarcseconds. They found a relation between $\log\phi'$ and $\mathrm{V}-\mathrm{R}$ and considering a $\Delta\lambda = 50$ Å between $3925-3975$ Å they obtain:

$$\log\mathcal{F}(\Delta\lambda) = 8.264 - 3.076(\mathrm{V}-\mathrm{R}) \text{ for } \mathrm{V}-\mathrm{R} < 1.30 \tag{2.14}$$

$$\log\mathcal{F}(\Delta\lambda) = 5.500 - 0.944(\mathrm{V}-\mathrm{R}) \text{ for } \mathrm{V}-\mathrm{R} > 1.30 \tag{2.15}$$

$\mathrm{V}-\mathrm{R}$ colour are taken by Johnson et al. (1966), but when these colours are unavailable they estimates $\mathrm{V}-\mathrm{R}$ by measured value of $\mathrm{B}-\mathrm{V}$ or spectral type.

Using these calibration relations and the adopted values of $\mathrm{V}-\mathrm{R}$, they derived the surface flux in the $3925-3975$ Å bandpass for each star to place the relative flux spectra on the absolute surface flux scale. Then, $\mathcal{F}(\mathrm{K}_1)$ and $\mathcal{F}(\mathrm{H}_1)$ have been calculated, considering the total surface flux above the zero flux level between the K_1 or H_1 minimum features.

The determination of the total radiative loss in these two lines is important in order to derive the net cooling rate in the chromosphere due to these lines. These cooling rates are defined as:

$$\mathcal{F}'(\mathrm{H}_1) = \mathcal{F}(\mathrm{H}_1) - \mathcal{F}_{\mathrm{RE}}(\mathrm{H}_1) \tag{2.16}$$

$$\mathcal{F}'(\mathrm{K}_1) = \mathcal{F}(\mathrm{K}_1) - \mathcal{F}_{\mathrm{RE}}(\mathrm{K}_1) \tag{2.17}$$

The terms $\mathcal{F}_{\mathrm{RE}}(\mathrm{H}_1)$ and $\mathcal{F}_{\mathrm{RE}}(\mathrm{K}_1)$ are the H_1 and K_1 indices for radiative equilibrium model atmosphere with no chromosphere. Kelch et al. (1979) computed them for for 13 main sequence stars obtaining the results showed by Linsky et al. (1979b) as in Figure 2.15:

In this approach, the direct excess radiative loss is obtained by subtracting the radiative equilibrium (RE) profile (derived from the LTE line blanked RE model of Kurucz) from the empirical one. A theoretical model has been constructed in order to match the observed line emission core. The difference between the "empirical" and "RE" profiles represent the direct excess of chromospheric radiation loss in the line core.

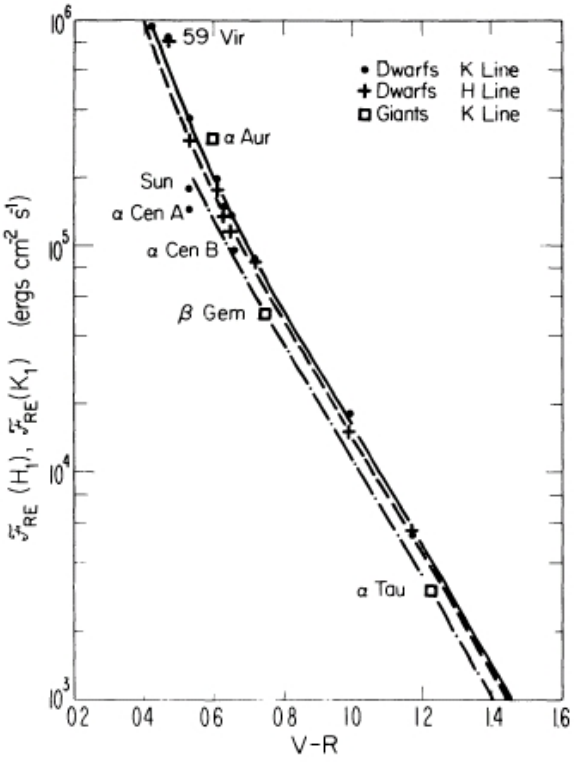

Figure 2.15: H_1 and K_1 indices for radiative equilibrium model atmospheres with no chromospheres, using the observed wavelengths of the H_1 and K_1 features to define the spectral bandpasses. The computed indices are taken from Kelch et al. (1979). The solid line is the estimated curve for $\mathcal{F}_{\rm RE}(K_1)$ for dwarfs, the dashed line is the $\mathcal{F}_{\rm RE}(H_1)$ for dwarfs, and the dot-dashed line is $\mathcal{F}_{\rm RE}(K_1)$ for giants. From Linsky et al. (1979b).

$\mathcal{F}_{\rm RE}(H_1)$ and $\mathcal{F}_{\rm RE}(K_1)$ can be estimated from Figure 2.15, which was obtained from Linsky et al. (1979b), using the computed indices taken from Kelch et al. (1979). Once that $\mathcal{F}'(H_1)$ and $\mathcal{F}'(K_1)$ have been found, it is possible to derive R_{HK}:

$$R_{HK} = \frac{\mathcal{F}'(H_1) + \mathcal{F}'(K_1)}{\sigma T_{\rm eff}^4} \tag{2.18}$$

estimating $T_{\rm eff}$ by the mean (V-R, $T_{\rm eff}$) relation of Johnson et al. (1966). R_{HK} is the chromospheric radiative loss in the H and K lines normalised to the total surface luminosity of the star.

The expression of $\mathcal{F}(K_1)$ and $\mathcal{F}(H_1)$ are defined by Linsky & Ayres (1978) (see also Strassmeier et al. (2000)) as the total surface flux above the zero flux level between the K_1 and H_1 minimum features, and are expressed as:

$$\mathcal{F}(K_1) = \frac{50\mathcal{F}}{f_{50}} f(K_1) \quad ; \quad \mathcal{F}(H_1) = \frac{50\mathcal{F}}{f_{50}} f(H_1) \tag{2.19}$$

where $\mathcal{F}$ is given by Equation 2.13, f_{50} is the integrated flux in $\Delta\lambda = 50$Å $f(K_1)$ and $f(H_1)$ the integrated fluxes between the minimums H_1 and K_1 (both in not normalised spectra). The precision of $\Delta\lambda(K_1) = \lambda(K_{1R}) - \lambda(K_{1V})$ depends on where the minima are setted and also depends by the instrumental resolution, as defined by Strassmeier et al. (1990). The red

and the violet K_1R and K_1V points of the central CaII K emission, determine the wavelength boundaries for their flux integration.

The area considered for the integration is represented in Figure 2.16. On the left, there is the integration band between the K_1 minima and on the right there is the 50Å bandpass. In some cases, especially for the supergiants, the location of these minima are uncertain, owing to asymmetries in the emission features, and the subjective determination of their wavelengths may increase the uncertainty of the adopted indices.

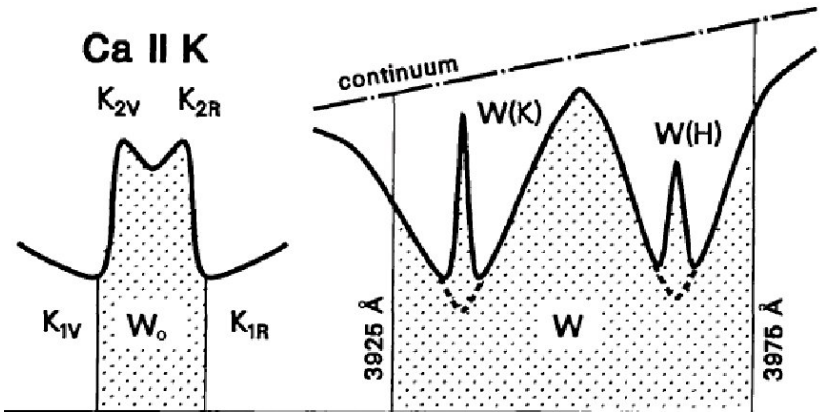

Figure 2.16: Left graph: Red(R) and violet (V) K_1 points of the central CaII K emission determine the wavelength boundaries for integration (dotted area W_0). The bottom indicate the zero flux level. Right graph: integration boundaries of the $\Delta\lambda = 50$Å bandpass needed for the flux calibration procedure. W(H) and W(K) are the equivalent widths of the K and H emission lines measured above the pseudocontinuum, while W is the equivalent width within the 50Å bandpass, including W(H) and W(K). From Strassmeier et al. (1990)

2.4.3 Profile fit method

The method of fitting have been introduced by Blanco et al. (1974) and then recovered by Fernández-Figueroa et al. (1994). In this technique, the emission fluxes of the CaII H and K lines ($F_{obs}(H;K)$) is obtained by the reconstruction of the absorption profile below the emission peak, following this method. The wing profiles are extrapolated toward the line center in order to define the level of the photosphere, as in Figure 2.17. Despite some authors (Linsky & Ayres, 1978) assume that this method overestimate the photospheric contribution, Fernández-Figueroa et al. (1994) state that it can be applied when the H1 and K1 minima have non zero intensity. Moreover, the authors affirm that this procedure is the only one that can be used with binary systems, due to the complication in the analysis, because the emission of the active component is contaminated by the non-active one. In the cases in which there is only one emission component, the profile reconstruction can be performed easily, otherwise, a deblend is necessary.

In this method, the Earth-observed flux $F_{obs}(H;K)$ is converted to the stellar surface flux $F_S(H;K)$ using the radius and the distance, otherwise, they used a linear relationship between

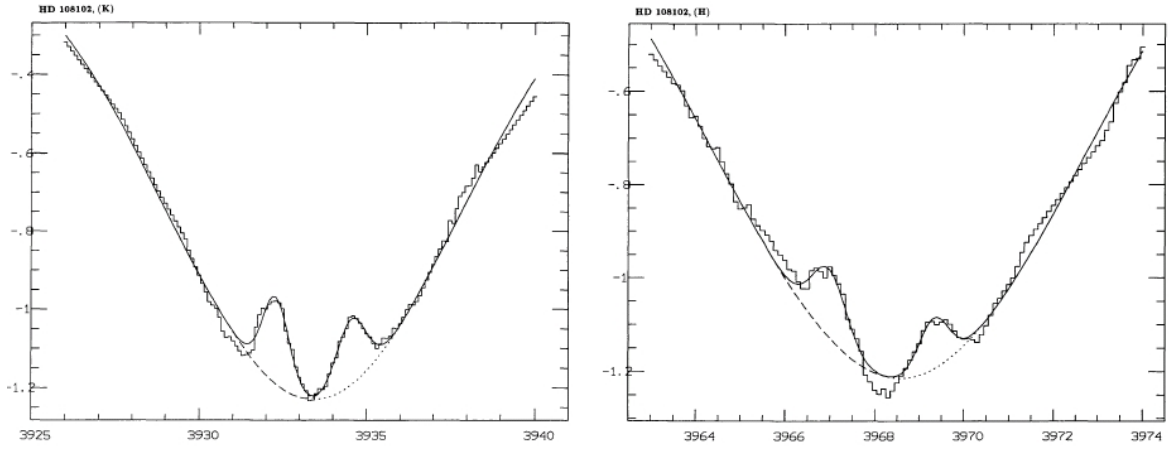

Figure 2.17: Gaussian fits to the CaII H and K for HD108102. The dotted and dashed lines are the Gaussian fits and the continuous line is the observed spectrum. From Fernández-Figueroa et al. (1994).

the absolute surface flux at 3950 Å and the colour index V-R of Pasquini et al. (1988). They give a parameter C(K) defined as:

$$C(K) = \frac{F_{obs}(K)}{F_T(K) - F_{obs}(K)}$$

where $F_T(K)$ is the total CaII K emission line flux above the zero flux level, whereas $F_{obs}(K)$ is the flux above the pseudocontinuum.

Obviously, as the authors confirm, uncertainties in the measurements of the fluxes can be due to different sources. First of all, the level of the pseudocontinuum can be erroneously defined if the emission peak is centered at the same wavelength of the absorption line, since in this case the reconstruction of the absorption profile is subjective. Another problem can be due to the presence of the emission of H_ϵ, that can contaminate the CaII H line. Moreover, there are some errors connected to the accuracy of the factor $(R/d)^2$ derived by Pasquini et al. (1988). For all these reasons, Fernández-Figueroa et al. (1994) estimate the total error with an upper bound of 25%.

2.4.4 Spectral subtraction method

The method of the subtraction technique was developed by Montes et al. (1995a) and subsequent papers (Montes et al., 1997, 1998, 2000; Gálvez et al., 2007, 2009), and permits to determine the chromospheric contribution by subtracting the underlying photospheric contribution. This technique has been already used for the H_α lines (Montes et al., 1995c) and different attempts for the CaII H and K have been made in the past (Catalano, 1979; Thatcher & Robinson, 1993; Strassmeier, 1994; Griffin et al., 1994).

This technique consists of the subtraction of a stellar spectrum constructed from artificially rotationally broadened, radial-velocity shifted, and weighted spectra of inactive stars

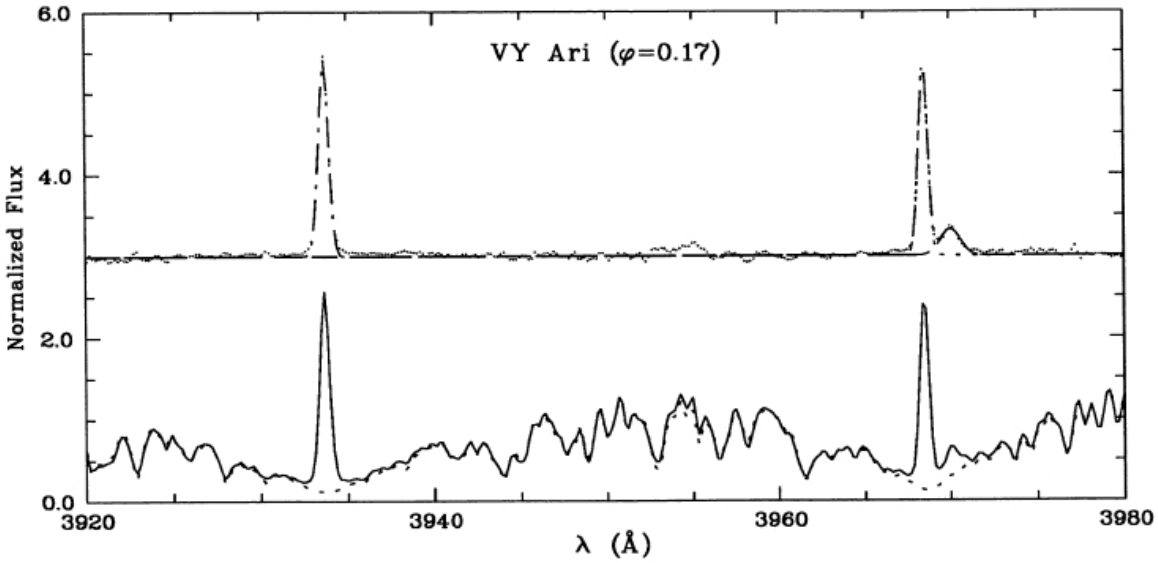

Figure 2.18: CaII H an K observed spectra of VY Ari and a reference stars of G8IV spectral type. From Montes et al. (1995c).

chosen to match the spectral types and luminosity classes of star studied (Figure 2.18). With the subtraction, a residual spectrum of the contribution of CaII H and K line is obtained. The excess emission EW(H;K) is defined as the equivalent width measured in the subtracted spectrum, and it is finally corrected for the contribution of the total continuum, using the relations of Pasquini et al. (1988), as a function of $V - R$. This one differs from the relation derived by Linsky et al. (1979b).

Montes et al. (1995a) applied this method for measuring the EW in binary systems and compared the results with those obtained by profile fitting (see Figure 2.19). Both methods give similar results, though the subtraction technique produce somewhat larger EWs. Since 1997, the Hall (1996)relation has been used instead of the Pasquini et al. (1988) one. The flux relation with $B - V$ is expressed as:

$$\log \mathcal{F}_{c,\lambda 3950} = [8.22 - 1.995(B - V)] \pm 0.045$$

valid for $-0.1 \leq B - V \leq 1.2$ and applicable for the dwarfs only. The final flux of each line is obtained considering the EW multiplied for the flux correction:

$$\mathcal{F}_{H;K} = \mathcal{F}_{c,\lambda 3950} \cdot EW(H;K)$$

In this way, one can obtain the same index introduced by Wilson $R'_{hk} = F'_{HK}/\sigma T^4_{eff}$ where $F'_{HK} = F'_H + F'_K = \mathcal{F}_H + \mathcal{F}_K$, because $\mathcal{F}_H$ and $\mathcal{F}_K$ have already been corrected for the photospheric contribution.

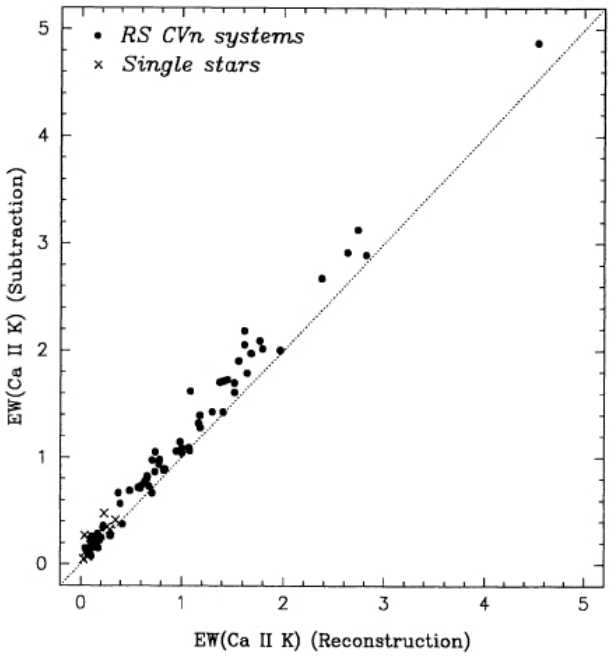

Figure 2.19: Relation between the excess CaII K emission EW measured by reconstruction of the absorption line and using the spectral subtraction technique. From Montes et al. (1995c).

2.4.5 Considerations about the methods

The Wilson's method requires a calibration using standard stars to determine the α coefficient. Unfortunately, this is not possible with VLT/GIRAFFE since no standard star can be observed together with cluster's stars.

The subtraction method is effective for stars with known luminosity and spectral type and requires the definition of some reference stars. Since astrophysical parameters in open clusters' stars are often not well determined, this approach may not be feasible. Alternatively, the profile fitting method could be used, but this seems to underestimate the emission.

The most feasible method seems therefore the Linsky et al. (1979b) one, used also by Strassmeier et al. (2000), which does no require any comparison with standard star but only the conversion to absolute flux that can be done using stellar colours. This is the method that I applied to VLT/GIRAFFE spectra of stars in NGC2516.

Chapter 3

Description of the clusters

3.1 The open cluster NGC2516

The southern open cluster NGC 2516 is a well study open cluster of intermediate-age. Located in Carina, it was discovered by Abbe Lacaille in 1751-1752. Since there are many bright stars in this cluster and the age is close to that of Pleiades it is also called the "southern Pleiades" by Eggen (1972). The basic information about the cluster are listed in Table 3.1

Table 3.1: Basic parameters of NGC2516. Data are taken from Cox (2000) except for the distance modulus (Jeffries et al., 2001), and the reddening and metallicity (Terndrup et al., 2002).

BASIC PARAMETERS OF NGC 2516	
RA(J2000)	$7^h58^m07^s$
DEC(J2000)	$-60°45.2'$
Galactic longitude l	$273.8°$
Galactic latitude b	$-15.9°$
Distance modulus $(V - M_V)$	7.85 ± 0.05[mag]
Metallicity [Fe/H]	0.01 ± 0.07
reddening $E(B - V)$	0.12 ± 0.02 [mag]

In Figure 3.1, I plot the stars of the NGC2516 for which the chromospheric index and the lithium abundance. The image is taken from the Aladin [1] archive and displayed using the Aladin tool.

NGC 2516 has a mass about twice that of the Pleiades, and many stars have been photometrically observed. Photometric studies of early-type cluster members were presented by Cox (1955),Eggen (1972) and Dachs & Kabus (1989). More recent photometric surveys that cover also low mass stars are from Jeffries et al. (2001); Sung et al. (2002); Irwin et al. (2007) and Terndrup et al. (2002).

The NGC metallicity has been determined by different authors (Cameron, 1985; Jeffries et al., 1997; Pinsonneault et al., 1998; Jeffries et al., 1998; Terndrup et al., 2002) and found to be close to solar. As underlined by Terndrup et al. (2002), the cluster age from the main-sequence

[1] http://aladin.u-strasbg.fr/aladin.gml

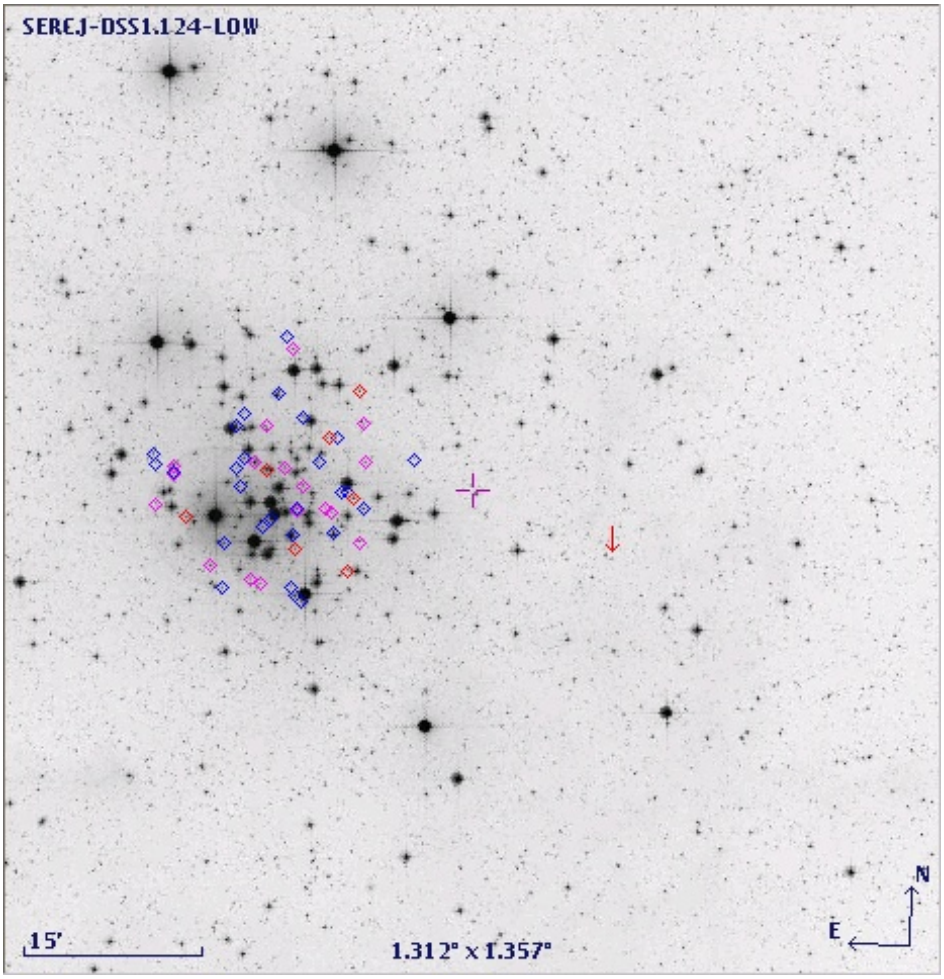

Figure 3.1: Stars of NGC2516. In blue are active stars for which I measured the chromospheric index R'_{hk}, in red are stars with lithium line visible, and in pink there are stars common in both surveys. The image is taken from the SERC observing program, using the filter J-DSS1 at 0.468 μm and achieved by using Aladin.

turnoff depends sensitively on the metallicity. If NGC 2516 is near solar metallicity, then it should have an age of 140 Myr, but it would have an age about 180 Myr for [Fe/H] ≈ 0.3, a difference of 30%. The abundance of NGC 2516 has been derived in different papers (Jeffries et al., 1998; Terndrup et al., 2002) and it is close to the solar one. Beryllium observations, instead, have been done by Randich et al. (2007). Jeffries et al. (1998) assume that it have a significantly lower metallicity than other well-studied clusters, between $-0.1 <$ [Fe/H] < 0.0. Moreover, they noticed that for the late G/early K stars, where a scatter is present in the Li abundances, the most rapid rotators are least Li-depleted.

Other information about the cluster have been acquired by Robichon et al. (1999), that determined the distance using Hipparcos parallaxes, Meynet et al. (1993), that measured turn-off masses, reddening and distance modulus of NGC 2516 and other open galactic clusters. King (1978), instead, derived the proper motion membership probability of 117 bright stars of this cluster. Jeffries et al. (1998) determined rotational rates and Li abundances of F/G

stars and then González & Lapasset (2000) measured radial velocities of bright stars near the main-sequence turnoff. Their works have been extended by Terndrup et al. (2002).

Also the chromospheric and coronal activity has been studied for this cluster. Several X-ray surveys have been performed with ROSAT (Dachs & Hummel, 1996; Jeffries et al., 1997; Micela et al., 2000), Chandra (Harnden et al., 2001; Damiani et al., 2003; Wolk et al., 2004) and XMM-Newton (Sciortino et al., 2001; Marino et al., 2006; Pillitteri et al., 2006), while chromospheric activity was studied by (Hawley et al., 1999) that measured the activity strength in H_α for low mass stars. A measure of CaII activity and rotation in two evolved stars of this cluster was performed by Pasquini et al. (2000). A most recent survey of CaII IRT emission in low mass stars has been done by Jackson & Jeffries (2010).

The star of this clusters, observed by FLAMES, have been identified using the coordinates given in the FITS header, and then searching the correspondent star with SIMBAD. The members found are listed, with the correspondent radius of the query, in the Table 3.2, together with photometry of and radial velocities (see caption for the references). In Table 3.3 the stars of NGC2516 for which I have X data and lithium abundances are listed.

Table 3.2: Members of NGC2516. In the first column there the band of flames in which the stars have been observed, in the second the numeration from Jeffries et al. (2001). δr(asec) is the difference in arcsecond between the RA and DEC of the header (third and fourth columns) and that ones of Jeffries et al. (2001). Vmag, B-V and V-I are from Jeffries et al. (2001). B(*) is the binarity as found by Jeffries et al. (2001) (Y means binary, N not binary). V_{rad}, $v \sin i$ and their errors are from Terndrup et al. (2002) and Jeffries et al. (1998). B(**) are from Damiani et al. (2003) and give the binarity as B(*).

Band	JTH	δr(asec)	RA	DEC	Vmag	B-V	V-I	B(*)	V_{rad}	e(V_{rad})	v sin i	e(v sin i)	B(**)
CaII	4670	0.308	7 56 36.82	-60 43 37.60	14.131	1.067	1.199	N					
CaII	5702	0.200	7 57 5.94	-60 43 41.20	14.149	0.613	0.785	N					
CaII	5833	0.202	7 57 9.38	-60 48 2.70	12.437	0.602	0.718	N	24.0	3.1	37.7		
CaII	5862	0.192	7 57 9.97	-60 44 10.20	13.289	0.732	0.843	N	24.8	0.9	15.4	1.3	
CaII	5901	0.161	7 57 10.83	-60 50 50.11	12.954	0.671	0.8	N	24.8	1.5	15.3		
both	6029	0.384	7 57 14.15	-60 40 52.46	12.24	0.674	0.769	Y	22.8	0.6	12.6	1.0	Y
both	6106	0.207	7 57 16.24	-60 47 13.63	12.035	0.537	0.652	N					N
CaII	6144	0.184	7 57 17.50	-60 38 11.01	12.287	1.22	1.24	N					
both	6157	0.270	7 57 17.73	-60 53 15.05	13.593	0.561	0.69	N					
CaII	6263	0.138	7 57 20.75	-60 46 44.39	14.184	0.903	1.007	N	23.3	0.6	$\leq$6		
CaII	6307	0.075	7 57 21.74	-60 55 20.21	14.38	0.874	1.048	N	0.8	0.7	$\leq$7		
CaII	6331	0.179	7 57 22.17	-60 52 5.80	14.296	0.706	0.826	N					
LiI	6373	0.454	7 57 23.15	-60 49 38.57	11.32	0.517	0.659	Y					Y
CaII	6452	0.143	7 57 25.21	-60 46 47.29	13.047	0.684	0.794	N	23.9	1.3	10.5	1.6	N
CaII	6501	0.212	7 57 26.43	-60 49 13.00	12.812	0.703	0.846	Y	-22.3	1.5	$\leq$8		
CaII	6605	0.237	7 57 29.37	-60 50 10.29	13.643	0.812	0.96	Y					Y
both	6649	0.237	7 57 30.91	-60 48 31.77	14.037	0.817	0.979	N	5.1	0.5	7.0	0.0	N
CaII	6676	0.090	7 57 31.53	-60 42 10.79	14.287	0.938	1.007	N	24.7	0.6	$\leq$6		
CaII	6705	0.107	7 57 32.19	-60 44 13.19	13.968	1.022	1.108	Y	91.3	0.8	$\leq$7.0		
LiI	6724	0.17	7 57 32.76	-60 53 49.03	14.009	1.043	1.112	Y	77.0	0.6	7.0	0.0	
CaII	6852	0.199	7 57 36.08	-60 48 12.70	13.73	0.809	0.907	N	22.5	0.7	$\leq$7		
CaII	6880	0.248	7 57 36.65	-60 42 16.70	13.293	0.814	0.875	N	23.4	0.8	$\leq$7		
CaII	6994	0.205	7 57 39.68	-60 35 8.70	14.138	0.654	0.767	N					
CaII	7104	0.164	7 57 42.71	-60 44 20.69	12.682	0.636	0.75	N	25.9	0.8	21.6	1.2	
CaII	7312	0.112	7 57 47.91	-60 56 12.99	13.839	0.831	0.922	N	24.1	0.6	$\leq$7		
CaII	7466	0.176	7 57 52.32	-60 46 26.20	13.187	1.446	1.391	N					
CaII	7485	0.259	7 57 52.89	-60 55 44.19	11.801	0.771	0.819	N					

Table 3.2: (continued)

Band	JTH	δr(asec)	RA	DEC	Vmag	B-V	V-I	B(*)	V_{rad}	e(V_{rad})	v sin i	e(v sin i)	B(**)
both	7564	0.241	7 57 54.76	-60 51 44.88	13.991	1.101	1.166	Y					
both	7585	0.458	7 57 55.37	-60 48 27.18	12.905	0.719	0.876	Y	30.4	1.2	26.3	1.7	Y
CaII	7594	0.262	7 57 55.61	-60 52 57.90	12.66	1.16	1.228	N					
CaII	7595	0.207	7 57 55.62	-60 40 39.19	12.632	0.602	0.699	N					N
CaII	7619	0.161	7 57 56.11	-60 54 59.00	14.322	0.935	1.008	N	25.1	0.4	9.7	1.3	
CaII	7621	0.214	7 57 56.14	-60 36 41.49	13.809	1.18	1.259	N					
CaII	7650	0.126	7 57 56.83	-60 50 33.81	12.706	0.62	0.768	N	65.6	1.9	32.4	3.4	N
CaII	7676	0.117	7 57 57.62	-60 49 46.70	13.417	0.605	0.739	N					
LiI	7743	0.381	7 57 59.30	-60 56 53.42	12.647	0.655	0.802	Y	23.5	1.2	24.4	2.1	Y
LiI	7784	0.529	7 58 0.36	-60 35 53.11	12.977	1.458	1.472	N					
CaII	7864	0.168	7 58 2.39	-60 46 47.29	12.068	0.603	0.741	Y	27.4	0.9	24.2	2.2	Y
both	7941	0.801	7 58 4.67	-60 35 03.81	13.081	0.677	0.771	N					
CaII	7962	0.169	7 58 5.25	-60 47 40.30	11.96	0.535	0.646	N					
CaII	7967	0.155	7 58 5.30	-60 45 3.29	12.696	0.637	0.743	N	23.2	1.0	18.3	4.6	
CaII	7998	0.248	7 58 6.17	-60 48 32.99	13.332	1.25	1.292	N					
CaII	8099	0.222	7 58 8.85	-60 44 40.19	12.22	0.56	0.676	N					N
CaII	8139	0.173	7 58 9.86	-60 34 0.202	14.239	0.809	0.891	N					
CaII	8205	0.149	7 58 11.54	-60 45 47.80	14.054	0.621	0.783	N					
CaII	8262	0.187	7 58 12.89	-60 38 52.79	14.215	0.95	0.982	N	13.8	0.3	7.3		
CaII	8270	0.327	7 58 13.15	-60 49 24.30	12.166	1.206	1.14	N					
LiI	8340	1.509	7 58 14.71	-60 45 17.98	10.117	0.149	0.168	N					
both	8411	0.656	7 58 16.81	-60 54 52.58	13.964	0.866	0.944	N					N
CaII	8435	0.301	7 58 17.48	-60 50 5.69	13.914	1.44	1.916	N					
CaII	8458	0.215	7 58 18.01	-60 45 15.29	11.465	0.533	0.665	Y	20.8	5.0			Y
CaII	8536	0.184	7 58 20.31	-60 41 39.80	12.871	0.66	0.76	N	24.7	0.7	10.1	1.1	
LiI	8660	0.149	7 58 23.59	-60 37 21.98	12.354	0.571	0.672	N					N
both	8689	0.364	7 58 24.46	-60 54 34.12	13.933	0.966	1.046	Y	-0.4	0.5	7.0	0.0	Y
both	8725	0.463	7 58 25.80	-60 44 45.03	9.836	1.361	1.33	N					
CaII	8923	0.207	7 58 30.74	-60 46 1.00	13.974	1.031	1.099	Y					

Table 3.2: (continued)

Band	JTH	δr(asec)	RA	DEC	Vmag	B-V	V-I	B(*)	V_{rad}	e(V_{rad})	v sin i	e(v sin i)	B(**)
LiI	9048	0.392	7 58 33.27	-60 49 25.48	10.813	0.298	0.361	N					N
CaII	9054	0.198	7 58 33.39	-60 44 27.39	12.841	0.691	0.836	Y	27.6	1.0	22.6	1.0	Y
CaII	9140	0.235	7 58 35.72	-60 46 52.50	13.405	0.736	0.838	N	23.2	1.1	16.4	2.2	N
CaII	9146	0.169	7 58 35.87	-60 40 40.69	14.125	1.041	1.12	Y					
LiI	9175	0.247	7 58 36.45	-60 50 18.36	11.675	0.585	0.695	Y					Y
CaII	9286	0.138	7 58 39.05	-60 45 21.69	14.24	0.93	1.0	N	25.0	0.4	7.6	1.2	
CaII	9328	0.179	7 58 40.05	-60 41 42.90	12.212	0.561	0.673	N					N
CaII	9449	0.179	7 58 42.65	-60 42 38.19	14.182	0.723	0.82	N					
CaII	9465	0.117	7 58 43.26	-60 55 25.69	13.84	0.818	0.963	N	25.9	1.8	47.9	1.6	N
CaII	9475	0.112	7 58 43.49	-60 51 42.40	13.699	0.832	0.964	Y	68.1	0.6	<7		
both	9852	0.210	7 58 52.29	-60 53 37.69	12.142	0.659	0.758	Y	24.4	0.4	10.9	1.0	Y
LiI	9882	0.513	7 58 52.99	-60 36 10.59	9.781	0.185	0.239	Y					Y
LiI	10021	0.359	7 58 56.64	-60 54 09.36	13.91	1.221	1.264	N					
both	10315	0.260	7 59 5.26	-60 50 04.08	10.407	0.648	0.725	N					
both	10390	0.419	7 59 7.36	-60 44 20.19	12.029	0.654	0.98	N	38.3	0.5	8.8	0.5	
both	10526	0.573	7 59 10.89	-60 49 40.86	13.954	0.62	0.735	N					
both	10863	0.501	7 59 21.32	-60 46 02.80	12.341	0.569	0.695	N					N
both	10894	0.434	7 59 22.14	-60 45 26.72	11.873	0.616		N					N
CaII	11233	0.177	7 59 32.09	-60 48 45.00	13.879	0.834	1.019	Y	-4.9	1.2	15.8	1.9	Y
CaII	11304	0.216	7 59 34.02	-60 45 18.40	14.282	0.928	1.007	N					
LiI	11307	0.261	7 59 34.08	-60 42 58.34	13.701	0.741	0.838	N					
CaII	11366	0.271	7 59 36.45	-60 44 31.69	12.898	0.827	0.956	Y					Y

Table 3.3: Members of NGC2516 for which have been found data in the X band and about the Lithium abundance. In the first column there is the number used the numbering system of Jeffries et al. (2001). In the second column there are the log L_X for stars in which it as been detected or not (flag in column three). In this second case it represents an upper limit. The fourth column is the F_X measured in $(ct/s/cm^2)$, and in the fifth the $\log L_x/L_{bol}$. All these data are from Damiani et al. (2003). In the sixth there is the $\log L_x/L_{bol}$ from Pillitteri et al. (2006). From the seventh colum there are the equivalent widths of the Li and their errors, the abundances and their errors, and in the last there is $\log \frac{L_X}{L_{bol}}$. All these data are from Jeffries et al. (1998).

JTH	$\log L_x$	flag	F_X	$\log L_x/L_{bol}$ (Damiani2003)	$\log L_x/L_{bol}$ (Pillitteri2006)	EW(LiI)	eEw(LiI)	logNLi	eNLiI+	eNLiI-	$\log L_x/L_{bol}$ (Jeffries98)
5702		?	5.32								
5833	29.31	u									
5862		?	4.79	-4.37		125	8	2.8	0.06	-0.06	-3.89
5901	29.36	u		-4.58		88	28	2.77	0.17	-0.2	-4.01
6029	29.99	d	15.65								
6106	29.34	d	4.14								
6263	29.19	d	3.16	-4.04		136	13	2.36	0.07	-0.08	-4.76
6452	29.4	d	5.1	-4.26		54	33	2.54	0.25	-0.43	-3.93
6501	29.08	u		-4.75	-5.24	33	37	0.0	0.0	0.0	-4.12
6605	29.2	d	3.19								
6649	29.94	d	19.4								
6676	29.03	u		-4.01		134	13	2.25	0.07	-0.08	-3.83
6705	28.91	u			-4.63						
6852	29.16	d	2.93	-4.11		131	22	2.61	0.11	-0.12	-3.28
6880	28.98	u		-4.76	-5.21	-5	27	2.09	0.0	0.0	-4.37
7104	29.35	d	4.53								
7312		?	1.49	-3.93		140	15	2.6	0.08	-0.09	-5.05
7485		?	4.97								
7585	30.13	d	25.29								
7595	29.45	d	5.39								
7619		?	4.56								
7650	29.57	d	7.54								
7864	30.11	d	24.74								
7941	29.66	u									

Table 3.3: (continued)

JTH	log L_x	flag	F_X	log L_x/L_{bol} (Damiani2003)	log L_x/L_{bol} (Pillitteri2006)	EW(LiI)	eEw(LiI)	logN(Li)	eNLiI+	eNLiI-	log L_x/L_{bol} (Jeffries98)
7962	29.11	d	2.48								
7967	29.25	d	3.6	-4.37		28	26	2.65	0.0	0.0	-3.16
8099	29.77	d	11.2								
8262	29.19	u			-3.98						
8270		?	2.42								
8340					-6.16						
8411		?	1.46								
8435		?	1.99								
8458	30.09	d	20.81	-4.31		52	10	2.94	0.1	-0.12	-4.05
8536	28.98	d	1.92	-4.59		93	11	2.92	0.08	-0.08	0.0
8689		?	1.83								
8923	28.84	d	1.4		-3.4						
9054	30.03	d	18.28								
9140	30.05	d	19.71	-3.45		176	33	3.01	0.15	-0.15	-4.25
9146	29.08	u			-4.64						
9286	28.95	d	1.8								
9328	29.58	d	7.19								
9465	30.07	d	23.81								
9475	29.0	u		-4.25	-4.95	14	20	0.0	0.0	0.0	-4.37
9852	29.52	d	7.19								
10863	29.4	d	4.77								
10894		?	7.33								
11233		?	34.62	-3.05		237	29	3.03	0.13	-0.13	
11304	29.41	u			-4.67						
11307					-5.05						
11366		?	31.42								

3.2 The open cluster NGC3766

NGC 3766, is a young open star cluster located in the Carina complex, discovered by Abbe Lacaille on March 5, 1752 from South Africa and it is known to contains an unusually large number of Be stars (Slettebak, 1985). In Table 3.4 are listed the basic information about this cluster, while in Figure 3.2 I plotted the stars of the NGC3766 for which I measured the lithium abundance on an archive image of Aladin, by using its tool.

Table 3.4: Basic parameters of NGC3766. Data are taken from WEBDA, except for reddening and distance modulus (Moitinho et al., 1997).

BASIC PARAMETERS OF NGC3766	
RA(J2000)	$11^h36^m14^s$
DEC(J2000)	$-61°36'30''$
Galactic longitude l	294.117°
Galactic latitude b	−0.030°
Distance	1.74 kpc
Reddening E(B − V)	0.20 ± 0.10 [mag]
Distance modulus $(V - M_V)$	11.73 ± 0.33 [mag]

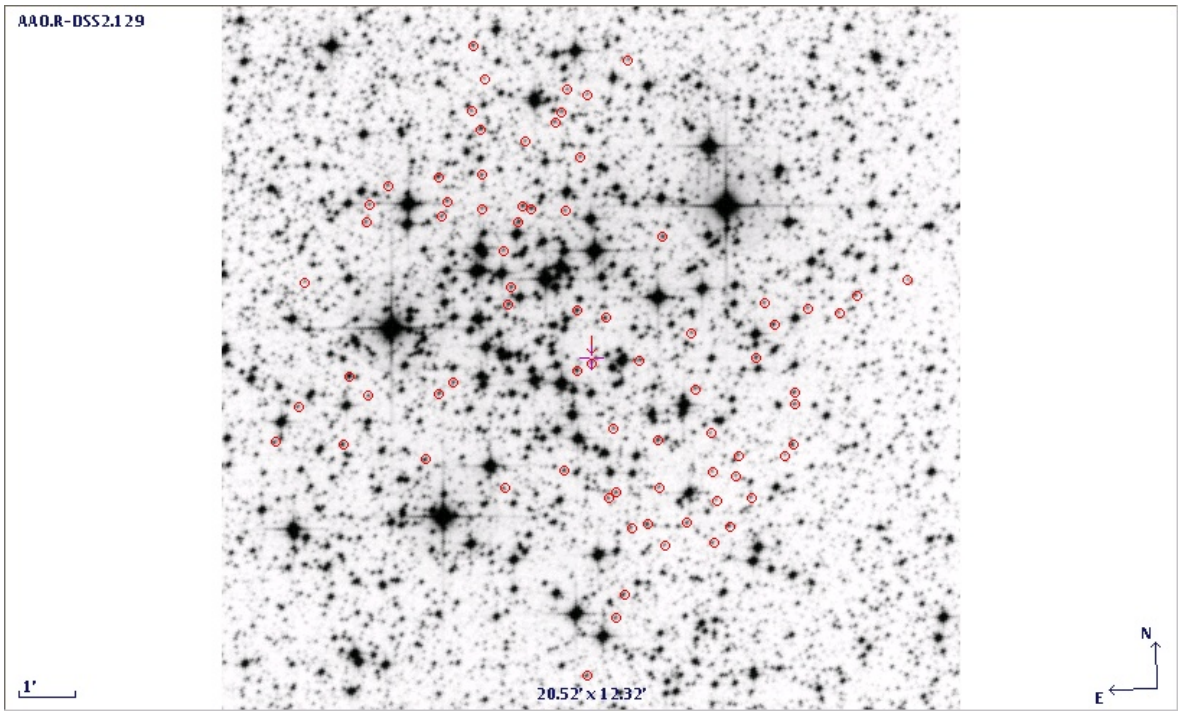

Figure 3.2: Stars of NGC3766. In red are stars observed in the survey of FLAMES from 27 January to 11 February 2009 for the abundance of lithium has been observed.The image is taken from the AAO observing program, using the filter R-DSS2 at 0.64 μm and achieved by using Aladin.

The cluster has been the target of numerous photometric studies (Yilmaz, 1976; Shobbrook, 1985, 1987; Moitinho et al., 1997; Tadross, 2001). Unfortunately, despite the abundance of surveys, the cluster's age and distance remain uncertain; measurements of its age

range from 14.5 to 25 Myr, and its distance is between 1.5 and 2.2 kpc (McSwain, 2008, and references therein).

The reddening and distance modulus determined by different authors are not in particular good agreement. For example, WEBDA[2] gives a reddening of 0.175 and a distance modulus of 11.75 (without including errors), while Moitinho et al. (1997) provides $E(B-V) = 0.20 \pm 0.10$, a distance modulus of $(V-M_V) = 11.73 \pm 0.33$ and an age of about 24 Myr. McSwain (2008), instead, analysed 47 members of NGC 3766, providing improvements to the reddening and distance, finding $E(B-V) = 0.22 \pm 0.03$ and $(V-M_V)_0 = 11.6 \pm 0.2$, respectively, at a distance of 1.9 to 2.3 kpc. A measure of the parallax has been done by Robichon et al. (1999) and is of $\pi = 1.36 \pm 0.63$mas.

The photometric information about this cluster, for stars in which I measured the lithium EW, is listed in Table3.5, using VRI photometry of Messina, S. (private communication).

[2] http://www.univie.ac.at/webda/navigation.html

Table 3.5: VRI photometry for NGC 3766. Numbering system and V,R,I colour are from Messina, S. (private communication).

N	RA	DEC	V	eV	R	eR	I	eI	V-R	e(V-R)	V-I	e(V-I)	R-I	e(R-I)
12	11 35 36.48	-61 38 53.52	15.300	0.018	15.007	0.029	14.450	0.019	0.293	0.034	0.850	0.026	0.557	0.034
17	11 35 37.68	-61 39 3.96	17.694	0.104	17.207	0.067	16.517	0.044	0.487	0.123	1.177	0.112	0.690	0.080
20	11 35 42.96	-61 39 46.79	16.437	0.037	16.069	0.039	15.431	0.012	0.368	0.053	1.006	0.038	0.638	0.0400
23	11 35 46.32	-61 40 15.96	15.152	0.020	14.987	0.028	14.527	0.0040	0.165	0.034	0.625	0.020	0.46	0.028
29	11 35 48.72	-61 40 32.88	16.365	0.024	16.014	0.049	15.392	0.035	0.351	0.054	0.972	0.042	0.621	0.060
32	11 35 18.72	-61 36 5.03	17.778	0.117	17.333	0.064	16.501	0.051	0.445	0.133	1.277	0.127	0.832	0.081
57	11 35 35.99	-61 38 11.03	16.175	0.042	15.812	0.034	15.212	0.004	0.363	0.054	0.962	0.042	0.600	0.034
61	11 36 8.16	-61 42 46.43	15.685	0.020	15.384	0.031	14.785	0.009	0.301	0.036	0.900	0.021	0.599	0.032
62	11 35 45.12	-61 39 23.41	17.119	0.028	16.634	0.049	15.905	0.033	0.485	0.056	1.213	0.043	0.729	0.059
65	11 35 47.99	-61 39 48.23	17.380	0.091	16.938	0.045	16.263	0.031	0.442	0.101	1.116	0.096	0.674	0.054
66	11 35 35.99	-61 37 58.79	15.608	0.019	15.290	0.037	14.713	0.032	0.318	0.041	0.894	0.037	0.576	0.048
77	11 35 44.64	-61 39 2.16	16.359	0.024	15.893	0.037	15.277	0.039	0.466	0.044	1.081	0.045	0.615	0.053
78	11 35 52.56	-61 40 10.92	16.041	0.023	15.690	0.040	15.084	0.010	0.351	0.046	0.957	0.025	0.605	0.041
79	11 36 3.59	-61 41 47.77	16.151	0.035	15.816	0.035	15.294	0.003	0.335	0.049	0.856	0.035	0.522	0.035
80	11 35 26.40	-61 36 19.44	15.906	0.024	15.515	0.032	14.856	0.004	0.391	0.040	1.050	0.024	0.659	0.032
89	11 35 29.04	-61 36 36.72	16.751	0.037	16.374	0.043	15.636	0.014	0.377	0.056	1.114	0.039	0.738	0.045
90	11 35 55.92	-61 40 33.59	17.139	0.030	16.653	0.042	16.022	0.029	0.486	0.051	1.117	0.041	0.631	0.051
95	11 36 2.16	-61 41 23.64	15.489	0.034	15.174	0.040	14.601	0.019	0.315	0.052	0.888	0.038	0.572	0.044
109	11 35 48.48	-61 39 17.99	17.065	0.040	16.543	0.049	15.872	0.011	0.522	0.063	1.193	0.041	0.670	0.050
126	11 35 58.32	-61 40 10.57	15.492	0.020	15.159	0.041	14.565	0.031	0.333	0.045	0.927	0.036	0.594	0.051
129	11 35 33.59	-61 36 30.96	17.117	0.047	16.667	0.044	16.032	0.015	0.450	0.064	1.085	0.049	0.635	0.046
140	11 35 48.48	-61 38 38.05	17.322	0.050	16.770	0.050	16.097	0.037	0.552	0.070	1.225	0.062	0.673	0.062
144	11 36 0.72	-61 40 13.81	16.372	0.038	15.951	0.038	15.315	0.010	0.421	0.053	1.057	0.039	0.636	0.039
145	11 35 41.52	-61 37 20.64	15.491	0.018	15.090	0.033	14.525	0.013	0.401	0.037	0.966	0.022	0.565	0.035
148	11 35 56.39	-61 39 32.76	16.915	0.030	16.424	0.041	15.690	0.021	0.491	0.050	1.225	0.036	0.734	0.046
161	11 35 38.64	-61 36 46.79	15.358	0.018	15.041	0.030	14.474	0.003	0.317	0.034	0.883	0.018	0.567	0.03
164	11 35 34.56	-61 36 5.76	16.858	0.028	16.368	0.057	15.536	0.048	0.489	0.063	1.321	0.055	0.831	0.074
188	11 35 39.84	-61 36 23.77	16.549	0.026	16.259	0.042	15.675	0.004	0.289	0.049	0.873	0.026	0.584	0.042
192	11 35 56.39	-61 38 43.09	15.625	0.035	15.223	0.029	14.551	0.007	0.402	0.045	1.074	0.035	0.671	0.029

Table 3.5: (continued)

N	RA	DEC	V	eV	R	eR	I	eI	V-R	e(V-R)	V-I	e(V-I)	R-I	e(R-I)
196	11 35 50.64	-61 37 50.87	16.417	0.025	15.954	0.039	15.254	0.013	0.463	0.046	1.163	0.028	0.700	0.041
198	11 36 2.878	-61 39 36.36	16.055	0.030	15.719	0.035	15.120	0.008	0.336	0.046	0.935	0.031	0.599	0.035
205	11 36 3.843	-61 39 42.12	16.534	0.034	16.052	0.044	15.411	0.022	0.482	0.055	1.123	0.040	0.640	0.049
271	11 35 50.88	-61 36 52.19	17.108	0.072	16.539	0.042	15.804	0.025	0.569	0.083	1.303	0.076	0.734	0.048
299	11 36 10.32	-61 39 11.16	15.677	0.022	15.321	0.030	14.741	0.018	0.356	0.037	0.935	0.028	0.579	0.034
308	11 35 58.56	-61 37 18.48	15.913	0.049	15.604	0.035	15.099	0.019	0.309	0.060	0.814	0.080	0.505	0.04
315	11 36 2.87	-61 38 29.39	16.740	0.028	16.283	0.047	15.591	0.029	0.457	0.054	1.149	0.040	0.692	0.055
354	11 36 19.20	-61 39 27.00	16.398	0.025	15.940	0.047	15.223	0.041	0.458	0.053	1.175	0.048	0.717	0.062
362	11 36 5.76	-61 37 19.56	16.866	0.028	16.375	0.055	15.744	0.036	0.491	0.061	1.121	0.045	0.630	0.065
373	11 36 7.92	-61 37 26.76	14.927	0.020	14.612	0.028	14.048	0.016	0.315	0.034	0.878	0.025	0.564	0.032
388	11 36 3.36	-61 36 33.11	15.382	0.022	15.014	0.028	14.418	0.022	0.368	0.035	0.963	0.031	0.595	0.035
399	11 35 54.48	-61 35 10.32	16.041	0.030	15.661	0.033	15.039	0.017	0.380	0.044	1.002	0.034	0.622	0.037
422	11 36 7.44	-61 36 24.12	14.668	0.015	14.463	0.025	13.972	0.004	0.205	0.029	0.696	0.015	0.491	0.025
484	11 36 30.72	-61 38 53.52	15.025	0.031	14.822	0.029	14.335	0.015	0.203	0.042	0.689	0.034	0.486	0.032
524	11 36 26.16	-61 37 33.95	16.471	0.027	15.986	0.042	15.274	0.005	0.485	0.049	1.197	0.027	0.711	0.042
527	11 36 17.52	-61 36 14.76	15.448	0.021	15.055	0.028	14.509	0.015	0.393	0.035	0.939	0.025	0.546	0.031
535	11 36 28.32	-61 37 45.12	15.695	0.020	15.383	0.033	14.806	0.021	0.312	0.038	0.888	0.028	0.577	0.039
546	11 36 17.04	-61 35 56.75	16.078	0.030	15.663	0.040	15.054	0.015	0.415	0.049	1.023	0.033	0.609	0.042
551	11 36 8.64	-61 34 39.35	17.108	0.040	16.724	0.046	16.025	0.024	0.384	0.060	1.083	0.046	0.699	0.051
584	11 36 6.24	-61 33 43.56	16.714	0.118	16.271	0.047	15.569	0.011	0.443	0.127	1.145	0.118	0.701	0.048
601	11 36 17.99	-61 35 18.25	17.050	0.072	16.719	0.046	15.994	0.007	0.331	0.085	1.055	0.072	0.724	0.046
602	11 36 13.68	-61 34 35.39	15.567	0.021	15.194	0.030	14.594	0.019	0.373	0.036	0.973	0.028	0.600	0.035
614	11 36 14.87	-61 34 32.16	15.429	0.018	15.180	0.030	14.646	0.003	0.249	0.034	0.783	0.018	0.534	0.03
618	11 36 42.72	-61 38 34.07	14.890	0.015	14.666	0.026	14.216	0.014	0.224	0.030	0.674	0.020	0.450	0.029
622	11 35 58.56	-61 32 3.84	17.355	0.030	16.808	0.042	16.026	0.015	0.547	0.051	1.329	0.033	0.782	0.044
636	11 36 38.63	-61 37 44.40	16.575	0.043	16.127	0.037	15.352	0.017	0.448	0.056	1.223	0.046	0.775	0.040
645	11 36 4.80	-61 32 38.77	17.345	0.032	16.871	0.059	16.248	0.038	0.474	0.067	1.097	0.049	0.623	0.070
657	11 36 9.59	-61 33 6.12	16.231	0.023	15.813	0.040	15.200	0.015	0.418	0.046	1.031	0.027	0.612	0.042
659	11 36 8.64	-61 32 56.04	16.635	0.036	16.191	0.050	15.557	0.043	0.444	0.061	1.078	0.056	0.633	0.065

Table 3.5: (continued)

N	RA	DEC	V	eV	R	eR	I	eI	V-R	e(V-R)	V-I	e(V-I)	R-I	e(R-I)
669	11 36 20.88	-61 34 33.24	16.805	0.032	16.359	0.040	15.804	0.027	0.446	0.051	1.001	0.041	0.554	0.048
674	11 36 7.68	-61 32 32.64	16.966	0.070	16.520	0.066	15.983	0.038	0.446	0.096	0.982	0.079	0.537	0.076
676	11 36 41.28	-61 37 22.80	13.620	0.009	13.600	0.017	13.248	0.005	0.019	0.019	0.371	0.010	0.352	0.017
681	11 36 14.16	-61 33 24.84	17.427	0.053	16.935	0.070	16.279	0.051	0.492	0.087	1.148	0.073	0.656	0.086
703	11 36 20.63	-61 33 58.32	16.242	0.024	15.849	0.042	15.200	0.024	0.393	0.048	1.042	0.033	0.649	0.048
712	11 36 52.55	-61 38 28.68	15.973	0.027	15.518	0.036	14.936	0.012	0.455	0.044	1.036	0.029	0.581	0.037
716	11 36 26.88	-61 34 40.08	16.492	0.043	16.136	0.043	15.509	0.005	0.356	0.060	0.983	0.043	0.626	0.043
723	11 36 15.60	-61 34 48.72	15.188	0.029	14.992	0.028	14.492	0.004	0.196	0.040	0.696	0.029	0.500	0.028
725	11 36 48.96	-61 37 52.69	16.553	0.065	16.081	0.037	15.448	0.020	0.472	0.074	1.104	0.068	0.632	0.042
728	11 36 25.92	-61 34 24.23	16.223	0.023	15.905	0.038	15.383	0.013	0.318	0.044	0.839	0.026	0.521	0.040
758	11 36 20.63	-61 33 10.08	14.777	0.018	14.640	0.026	14.209	0.006	0.137	0.031	0.568	0.018	0.431	0.026
770	11 36 27.12	-61 33 58.32	14.857	0.018	14.678	0.026	14.211	0.017	0.179	0.031	0.645	0.024	0.467	0.031
802	11 36 21.84	-61 32 51.36	16.663	0.026	16.262	0.052	15.602	0.029	0.401	0.058	1.060	0.038	0.659	0.059
826	11 36 19.68	-61 32 17.88	17.369	0.055	17.004	0.061	16.381	0.034	0.365	0.082	0.987	0.064	0.622	0.069
843	11 36 37.92	-61 34 42.59	16.676	0.028	16.288	0.045	15.681	0.007	0.388	0.053	0.995	0.028	0.607	0.045
855	11 36 34.56	-61 34 5.159	16.320	0.023	15.976	0.039	15.445	0.034	0.344	0.045	0.875	0.041	0.531	0.051
858	11 36 37.44	-61 34 24.96	16.813	0.026	16.350	0.039	15.662	0.015	0.463	0.046	1.151	0.030	0.688	0.041
871	11 36 47.28	-61 35 42.72	17.785	0.073	17.184	0.046	16.526	0.063	0.601	0.086	1.259	0.096	0.658	0.078
883	11 36 21.12	-61 31 43.33	16.001	0.024	15.618	0.033	15.023	0.025	0.383	0.040	0.977	0.034	0.595	.0410

Chapter 4

Data acquisition and reduction

The data of this work consist of spectra for the cluster NGC2516 around the CaII H and K lines and the LiI doublet. The observations of NGC3766 were carried out only in the lithium doublet region. In the first section I will describe the spectrograph FLAMES and its instruments, while in the second one I will explain the reduction technique.

4.1 ESO Observatory Spectrograph FLAMES

FLAMES (Fibre Large Array Multi- Element Spectrograph) is the multi-object, intermediate and high resolution spectrograph of the Very Large Telescope (VLT), mounted at the Nasmyth A platform of UT2-Kueyen. It consists principally consist of:

- A Fibre Positioner (OzPoz) hosting two plates: one plate observes and the other positions the fibres for the subsequent observations;
- A medium-high resolution optical spectrograph, Giraffe, with three types of feeding fibre systems: Medusa , IFU, ARGUS;
- A link to the UVES spectrograph (Red Arm) via 8 single fibres of 1 asec entrance aperture.

All the data of this thesis have been acquired with the Giraffe-Medusa fibre system, which observing modes are listed in Table 4.1:

Table 4.1: Instrument setups in FLAMES ((*) In HR mode, the resolution and spectral coverage depend on setting used.(**) λ is the desired observing wavelength.)

Spectrograph	Mode	Number of Objects	Aperture (")	Resolution (*)	Spectral Band [nm] (**)
Giraffe	Medusa	132(w.sky fibres)	1.2	12000-24000	$\lambda/12 - \lambda/24$
Giraffe	Medusa	132(w.sky fibres)	1.2	7000	$\lambda/9.5$

4.1.1 The Fiber Positioner (OzPoz)

The OzPoz fibre positioner (Figure 4.1) works in the following way: while one plate is observing, the other one is positioning the fibres for the subsequent observations, in order to reduce the dead time between two observations. Both plates host the 132 Giraffe Medusa buttons.

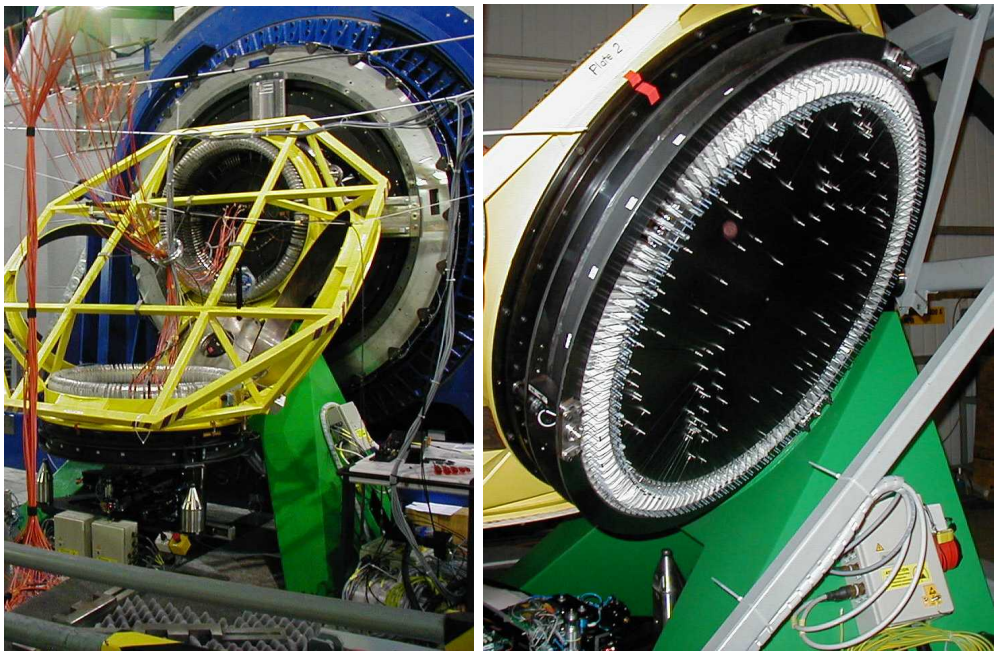

Figure 4.1: left: View of the Giraffe spectrograph with Ozpoz. Right: View of the back of one Ozpoz plate where all the fibres are attached with magnetic buttons.

4.1.2 The Giraffe Spectrograph

Giraffe (its name comes from the original design concept, where it was standing vertically on a platform) is a medium-high resolution (R = 7 500 − 30 000) spectrograph (Figure 4.2), that can cover the entire visible range 3700 - 9000 Å, but not at the same time. The grating setups are available in High and Low Resolution (in Table 4.2 are shown the configurations used in this thesis) but each object can be only observed in a single echelle order at once. The high resolution has 316 lines/mm with 63.5 blaze grating, while the low one has 600 lines/mm with 34.0 blaze grating. Five additional fibres allow simultaneous wavelength calibration of every exposure. The Medusa fibers allow up to 132 separate objects (including sky fibres). Two separate sets of Medusa fibers exists, one per positioner plate. Each fiber has an aperture of 1.2 asec on the sky. Giraffe is equipped with a 2K×4K EEV CCD (15 μm pixels) and the spatial scale is 0.3 asec/pixel.

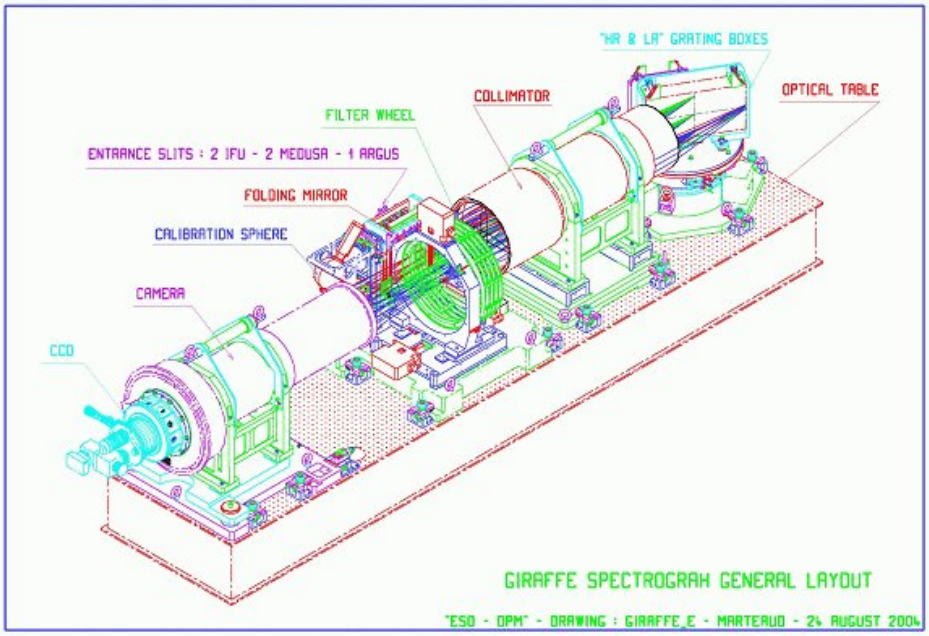

Figure 4.2: General layout of the Giraffe spectrograph.

Table 4.2: Giraffe Resolution Mode setups. F is the filter number; θ is the angle of diffraction with the grating normal; Ord is the working echelle order; Wl start, center, end are wavelengths at the edges and center of the CCD; Band is the covered spectral passband; R is the resolving power obtained in Medusa mode.

F	θ	Ord	p2pp name	ETC name	Wl start	Wl center	Wl end	Band	R
2	58.2	14	H395.8	HR2	385.4	395.8	404.9	19.5	19600
6	34.9	3	L682.2	LR6	643.8	682.2	718.4	74.6	8600

4.2 Giraffe data reduction

In the following subsections I will describe the procedure and the software used for the data reduction of the two open clusters, NGC2516 and NGC3766 (a pipeline specifically developed for the FLAMES-Giraffe spectra).

Data of the cluster NGC2516 consist of archive spectra retrived all from ESO Archive, taken around the CaII H and K lines (VLT programme 072.D-0160A), covering the wavelength range between 385.4 to 404.9 nm, with a resolution R$\sim$19600 and 30 min exposures, acquired on the 2004-03-04. The configuration is centered at RA(J2000) = $07^{\rm h}58^{\rm m}06.5^{\rm s}$ and DEC(J2000) = $-60^{\rm d}45^{\rm m}58.2^{\rm s}$.

Spectra around the lithium doublet (VLT programme 076.C-0384A) cover the wavelength range between 643.8 nm and 718.4 nm, with R$\sim$8000, acquired from the 2006-03-01 to the 2006-03-03, with the configuration centered at RA(J2000) = $07^{\rm h}58^{\rm m}06.1^{\rm s}$ and DEC(J2000) = $-60^{\rm d}45^{\rm m}29.1^{\rm s}$, and $\sim$60 seconds exposures. Ten observation have been made.

The observations of NGC3766 were carried out in Service Mode from 27 January to 11

February 2009 using FLAMES, selecting candidate members on the MS with $11 < V < 18$ (Figure 3.2), with a resolving power of R $\sim$ 8000, and 45 min exposures. The configuration centered at RA(J2000) = $11^h36^m10.3^s$ and DEC(J2000) = $-61^d36^m53.7^s$.

4.2.1 girBLDRS and Gasgano pipeline tasks

The data reduction of CaII H and K spectra of NGC2516 was performed using the Giraffe BaseLine Data Reduction Software (girBLDRS) pipeline [1], version 1.13, developed at Geneva and Paris Observatories, for which I followed the standard procedure (Blecha & Simond , 2004), removing the instrumental profile from the observed data, subtracting the bias and dividing by the normalised flat-field. All these operations have been carried out using pre-existing file, included in the pipeline.

The bias and the dark reduction can be performed using the master files given in the tables of girBLDRS and the tasks called *biasmast* and *darkmast*. It is not necessary to build new bias master files since model of bias is adjusted using the pre/over scan areas of science image. Then, I produced with the task *locMast* the localization necessary to any extraction, the model of the transverse PSF and the spectroscopic extracted (called "narrow") flat field.

I adjust the slit geometry calibration files by using the *wcalMast* pipe, in order to get full master wavelength solution from raw ThAr exposures, then I proceeded with the data reduction, by extracting the calibration frames with the tasks *extract*: flat-field and wavelength Th-Ar calibration, as well as science exposures. The extracted flat-fields were divided, and the wavelength calibration applied. After the extraction, the spectra were rebinned into a constant wavelength increment (0.005 nm) and also the scattered light was removed.

Since sky subtraction was not part of the pipeline procedure, it was achieved by taking the average of groups of sky spectra and averaging these to form a master sky spectrum that has been smoothed and then subtracted from each target spectrum. This has not been applied to the lithium spectra of NGC2516, since the SNR was too low. Extracted spectra of NGC2516 in the region of 50Å centered at 3950Å have been plotted in Figure B.1. Finally, the normalisation has been performed with the IRAF[2] continuum tasks.

The FITS header of every FLAMES-Giraffe file contains all information related to the fibres in two FITS extension tables:

1. the *OzPoz table*: it relates objects on the sky and fibre buttons in OzPoz;

2. the *Fibre table*: it relates the fibre buttons on OzPoz and the fibre positions in the slits.

[1] `http://girbldrs.sourceforge.net/`
[2] Image Reduction and Analysis facility, `http://iraf.noao.edu/`

Moreover, an *Objects table* enumerates the stars observed, together with the calibration lamps and grid sky observations. Using the girBLDRS tasks, I extracted these tables in order to identify each star observed and associate to it its correspondent spectrum. Thanks to the coordinates given in the objects table I associated the correspondent star by using SIMBAD (see Table 3.2).

All the Li spectra, both of NGC2516 and NGC3766 were reduced with the ESO pipeline implemented in Gasgano, that used the same procedure described before. Gasgano, is a Java-based data file organizer developed and maintained by ESO. It manage and organize the astronomical data observed and produced by VLT telescopes with a graphics-based software tool, in order to view data files produced by the VLT Control System. I used it to reduce data in the lithium band since the old girBLDRS pipeline cannot recognize the table format of the new ESO fits tables.

The data reduction in the lithium band with Gasgano [3] was performed following the standard procedure: bias subtraction, flat-field correction, wavelength calibration, and optimal spectrum extraction. It is similar to the Geneva pipeline, except for the presence of a more user-friendly interface.

As said before, the gridsky subtraction has been made making a mean of all the sky spectra and than smoothing it, then subtracted to the target. Finally, I normalised using the task continuum of IRAF.

4.2.2 Continuum normalisation

Continuum normalisation has been performed using the IRAF *continuum* task. In the lithium band the normalisation is straightforward. On the contrary, the region of CaII H and K range is very difficult to normalise because there is no well defined continuum visible anywhere. This is evident from Figure 4.3, where I show the synthetic spectra of two cool stars, produced with SYNTHE (Kurucz, 1993) (the procedure is described in Chapter 5), using the atmospheric model of Castelli & Kurucz (2004), with their superimposed continua. It is clear that in this spectral range, and expecially in the coolest star, the synthetic continuum is much higher than one would infer by a standard fitting normalisation. I should know the distance of each star and derive the absolute flux in order to compare the observed and the synthetic spectrum using the same scale.

Therefore, since I will need to compare the observed spectra with the models in this spectral range (as will be described in Chapter 5), I decided to perform the continuum normalisation of the synthetic spectra by means of the *continuum* task of IRAF.

[3] http://www.eso.org/sci/data-processing/software/pipelines/giraffe/giraf-pipe-recipes.html

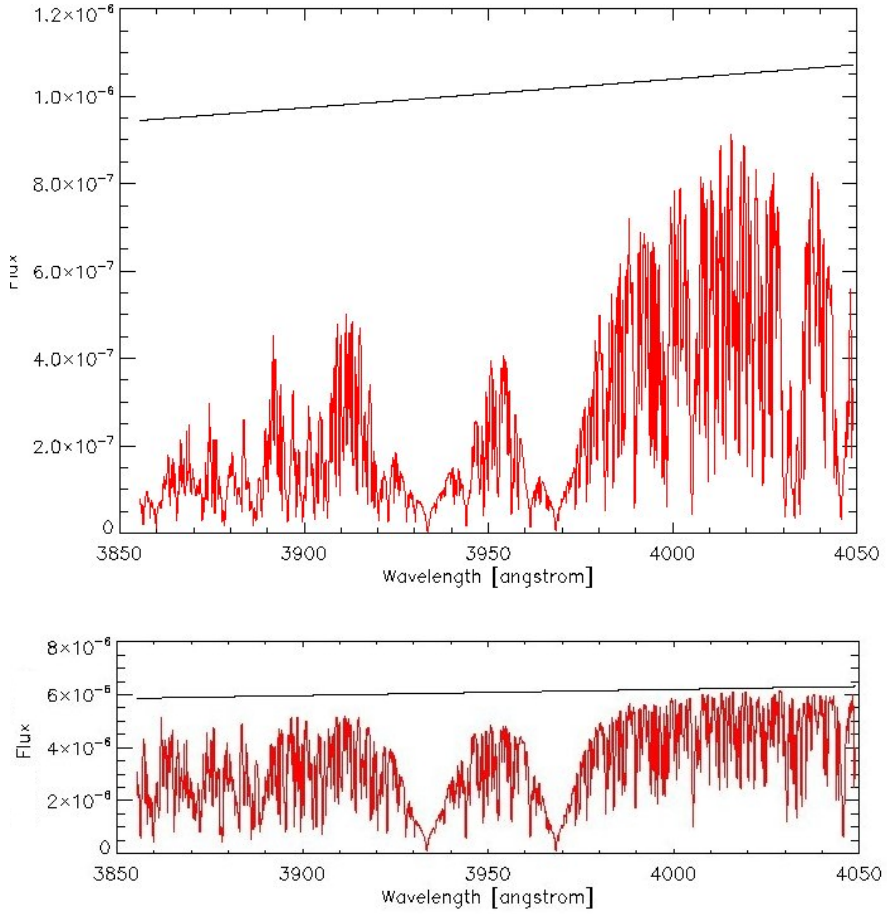

Figure 4.3: Top: Synthetic spectrum of a cool star with $T_{eff} = 4500$ K, $\log g = 4.5$, [Fe/H] = 0.0. The black line represents the continuum, the red spectra the absolute flux. Bottom: Synthetic spectrum of a star with $T_{eff} = 6000$ K, $\log g = 4.5$, [Fe/H] = 0.0 and its continuum flux (in black).

A test of the synthetic spectra normalisation is shown in Figure 4.4, upper panel, where I selected a low activity level star that I expect to be well described by a LTE radiative-equilibrium spectrum like the Kurucz one. In the figure, the black line represents the spectrum of the observation normalised with IRAF, the blue line is the synthetic spectrum normalised with IRAF, and the red line represents the Kurucz residual flux, calculated dividing the synthetic flux of Kurucz with its synthetic continuum.

In Figure 4.5 I plotted in red the residuals obtained considering the difference between the observed spectrum of a non active star and the Kurucz spectrum normalised with IRAF continuum task, while in blue I plotted the residuals between the observed and the synthetic spectrum normalised with the synthetic continuum. Furthermore, two linear fit for the residuals are overplotted. For the Kurucz spectrum normalised with its continuum I obtain $\chi^2 = 0.026$, while for the Kurucz spectrum normalised with IRAF continuum I have $\chi^2 = 0.027$ (detailed parameters of the fits are shown in table 4.3).

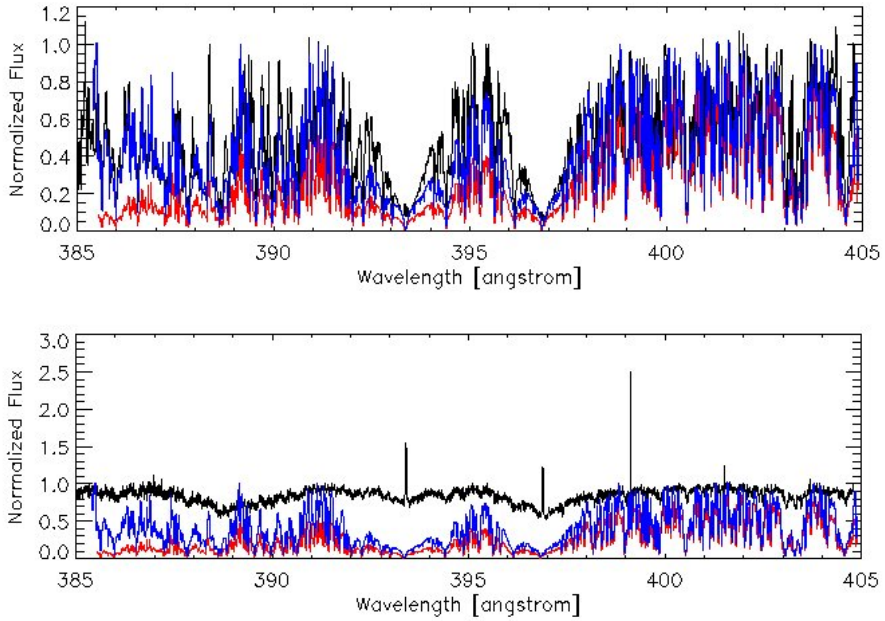

Figure 4.4: Normalised spectra of two stars of NGC2516 cluster (the non active star JTH 8725 in the top and the active star JTH8435 in the bottom), with temperature (calculated by $B-V$) closer to 4500, compared with the synthetic spectrum of a cool star with $T_{eff} = 4500$, $\log g = 4.5$, $[Fe/H] = 0.0$. The spectrum of the stars, normalised with IRAF, is black, in red there is the relative flux, calculated dividing the absolute synthetic flux of Kurucz with its synthetic continuum, in blue there is the absolute synthetic spectrum normalised with IRAF. The bottom spectrum is distant form the Kurucz spectra due to the presence of activity.

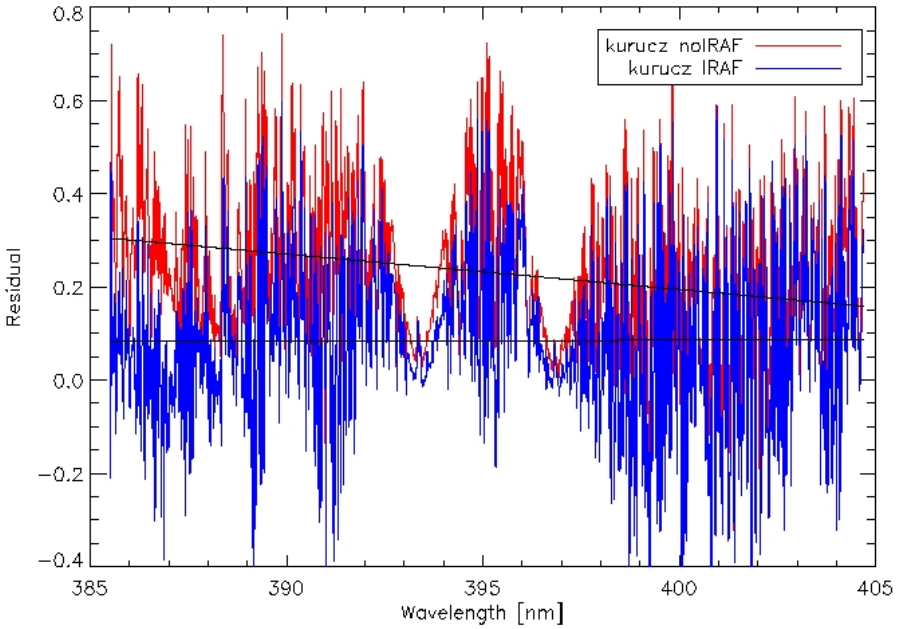

Figure 4.5: Residuals between the non active star, used as test, and the Kurucz spectra, normalised with IRAF continuum task (in blue), and with its continuum (in red). The two black lines represent a fit to the residuals.

Table 4.3: Coefficients and correspondent χ^2 and σ for the two calculated residuals. NoIRAF is the Kurucz spectrum normalised with its continuum, WithIRAF is the Kurucz spectrum normalised with IRAF continuum task.σ_a,σ_b are the errors on a and b respectively .

Spectra	fit coefficients	χ^2	standard deviations
NoIRAF	$a = -0.076, b = 3.231$	0.026	$\sigma_a = 0.0026$, $\sigma_b = 0.977$
WithIRAF	$a = +0.002, b = 0.013$	0.027	$\sigma_a = 0.002$, $\sigma_b = 0.724$

The fitting result shows that the synthetic spectrum normalised with IRAF continuum task best reproduces the observations.

Chapter 5

Parameters Determination

The knowledge of effective temperature (Teff), the surface gravity (g) and the metallicity [Fe/H] is essential to characterise the observed stars and to derive further quantities such as a chromospheric activity index and the Li abundance. This work has been done by comparing the observed equivalent widths (EW) of the spectral lines with those predicted by spectrum synthesis. The input data required for this procedure are: a model atmosphere corresponding to the atmospheric parameters ($T_{\rm eff}$, $\log g$, [Fe/H]) of the star; a set of EW for the lines being analysed.

In the first section I describe how I built a grid of synthetic spectra using (Kurucz, 1993) models. In the second section I describe how I derived the errors for the equivalents widths measured. Finally, in the third I explain the parameters determination by means the comparison with the models.

5.1 Grid of synthetic spectra

The models used in this thesis are based on a grid of ATLAS9 1D-LTE model atmospheres (Kurucz, 1993), widely used in widely used in stellar physics. Kurucz model atmospheres follow the assumptions of plane parallel and homogeneous layers, hydrostatic equilibrium, steady state, LTE and radiative and convective equilibrium. Models computed with the same values of $T_{\rm eff}$ and $\log g$ differs for chemical composition and in the mixing length parameter. In order to compute a synthetic stellar spectrum one needs a model that provides the structure of the atmosphere and describes quantitatively how physical quantities vary throughout the atmospheric layers.

My computation are based on Kurucz model atmospheres (derived by Castelli & Kurucz (2004) by using atlas) with 250 K, 0.5 dex, and 0.5 dex steps in $T_{\rm eff}$, [Fe/H], and $\log g$, respectively. Since the temperature spacing of 250K was high for my purposes, I decided to reduce the spacing step to 100K in order to achieve a better description of the system in the space of parameters, leaving the other parameters unvaried. The models were calculated

using the standard solar metallicity ODFs (Opacity Distribution Functions). The abundances of each model are explicitly set to the solar values (Kurucz 1993) for each element. All models were calculated with a constant microturbulent velocity of ∼2 km/s.

In order to determine the T_{eff} necessary to derive the R'_{hk} for the stars of NGC2516, I I built a grid of synthetic spectra over the FLAMES-Giraffe domain in the HR2 band (see Table 4.2). This grid has been calculated using the SYNTHE code (Kurucz, 1993, and later upgrades) from the LTE model atmospheres of Castelli & Kurucz (2004) computed with the ATLAS9 code.

Since I want to analyse only the cool stars of the clusters, and considering that the stars of the sample are dwarfs and they are main sequence stars, therefore I made this grid using the following restrictions: a range from 4000 K to 7000 K with a step of 100 K in effective temperature, a range from 3.5 to 5.0 with a step of 0.5 in surface gravity $\log g$ and [Fe/H] = 0 for the metallicity. All the spectra have been convolved to the FLAMES resolution at the HR2 band (R = 19600). As can be seen in Figure 4.4, the region of the spectrum in which there is not the contribute of the H and K lines wings, is approximately from 3990 to 4040 Å. The lines in this range have been identified (see Table 5.1) by means of Kurucz file output. I analysed in details the lines in this range in order to study their dependence on temperatures and gravities. In Figure 5.1, left panel, I show the synthetic spectra obtained for a fixed T_{eff} and five $\log g$ values, while on the right the synthetic spectra for $\log g = 4.5$ and five values of T_{eff} are shown.

In order to choose the best diagnostic for temperature and/or gravity , the sensitivity of the lines in the range 3990-4040 Å (table 5.1) have been investigated measuring their equivalent widths (EWs) in a grid of synthetic spectra.

The EW (or W) represents the strength of an absorption line, and it is defined as the width, in wavelength units, that a rectangular stripe of height F_c, in intensity units, would have if it had the same area as the actual line. The EW is defined as:

$$EW = \int_{\Delta\lambda} \frac{F_c(\lambda) - F(\lambda)}{F_c(\lambda)} d\lambda \tag{5.1}$$

where $F_c(\lambda)$ is the flux of the continuum, and $F(\lambda)$ is the flux elsewhere in the line. The Figure 5.2 (a) puts in evidence the relationship between the equivalent width and the shape of the line, for a normalised line profile. I calculated the EW using IDL[1].: the center of the line is found as the wavelength corresponding to the minimum, the edges of integration are found as the wavelengths corresponding to the flux maxima closest to the center. The method is shown in Figure 5.2(b). I measured the EW for all the detectable lines in the range 3990-4040

[1]Interactive Data Language: `http://www.ittvis.com/ProductServices/IDL.aspx`

Table 5.1: Principal lines identified for a synthetic spectrum with T_{eff} 4500 K and $\log g = 4.5$ in the range from 3990 and 4040 Å. In the first column there is the wavelength, in the second the correspondent element and in the third the oscillator strength $\log g_f$.

Wavelength (Å)	element	$\log g_f$	Wavelength (Å)	element	$\log g_f$
3990.33	TiI	-1.353	4015.37	TiI	-0.160
3991.11	CrI	0.252	4015.47	FiI	-0.783
3991.66	CrI	-0.599	4016.42	FeI	-1.600
3992.84	CrI	-0.434	4016.60	CrI	-0.673
3993.10	FeI	-1.460	4017.12	FeI	-1.992
3994.11	FeI	-1.470	4017.46	FeI	-0.676
3994.67	TiI	-0.705	4017.77	TiI	-0.120
3995.30	CoI	-0.220	4018.10	MnI	-0.309
3995.98	FeI	-1.450	4018.27	FeI	-1.360
3996.96	FeI	-0.840	4019.04	FeI	-2.780
3997.39	FeI	-0.390	4020.39	ScI	0.204
3997.90	CoI	-0.870	4020.89	CoI	-2.070
3998.05	FeI	-0.910	4021.86	FeI	-0.660
3998.64	TiI	-0.056	4022.21	FeI	-2.657
3998.72	VI	0.480	4022.98	NdII	-0.200
3998.97	TiI	-0.337	4023.40	CoI	-1.546
3999.03	NiI	-0.464	4023.68	ScI	0.322
4000.46	FeI	-1.630	4024.09	FeI	-2.300
4001.10	FeI	-2.757	4024.57	TiI	-0.981
4001.66	FeI	-1.880	4025.00	CrI	-0.577
4002.08	FeII	-3.472	4025.78	NiI	-0.777
4002.47	TiI	-0.100	4026.16	CrI	-5.016
4003.76	FeI	-1.290	4026.43	MnI	-0.520
4004.98	FeI	-2.174	4027.03	CoI	-2.873
4005.38	FeI	-2.208	4027.67	NiI	-0.640
4006.31	FeI	-0.990	4028.34	TiII	-1.000
4006.62	FeI	-1.371	4029.62	FeI	-1.939
4007.27	FeI	-1.300	4030.18	FeI	-2.310
4008.05	TiI	-0.106	4030.75	MnI	-0.470
4008.93	TiI	-1.072	4031.75	TiI	-0.325
4009.66	TiI	-1.837	4032.63	FeI	-2.440
4010.17	FeI	-1.790	4033.07	MnI	-4.120
4010.75	FeI	-3.674	4034.48	MnI	-0.811
4011.41	FeI	-2.400	4035.72	MnI	-0.190
4011.53	TiI	-1.400	4036.37	FeI	-2.840
4012.39	TiII	-1.610	4037.12	FeI	-0.708
4013.25	TiI	-0.620	4038.26	NiI	-1.005
4013.78	FeI	-2.149	4038.62	FeI	-1.886
4014.53	FeI	-0.200	4039.09	CrI	0.390

Å in the whole model grid. Figure 5.3 shows the measured EW versus model temperature for a selected set of lines.

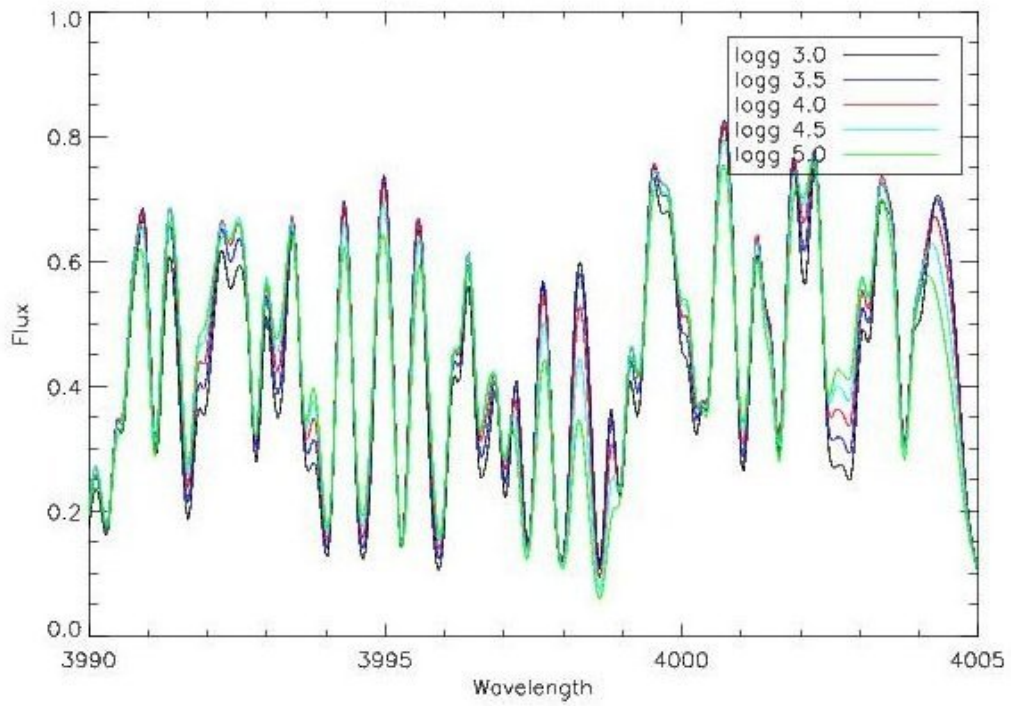

(a)

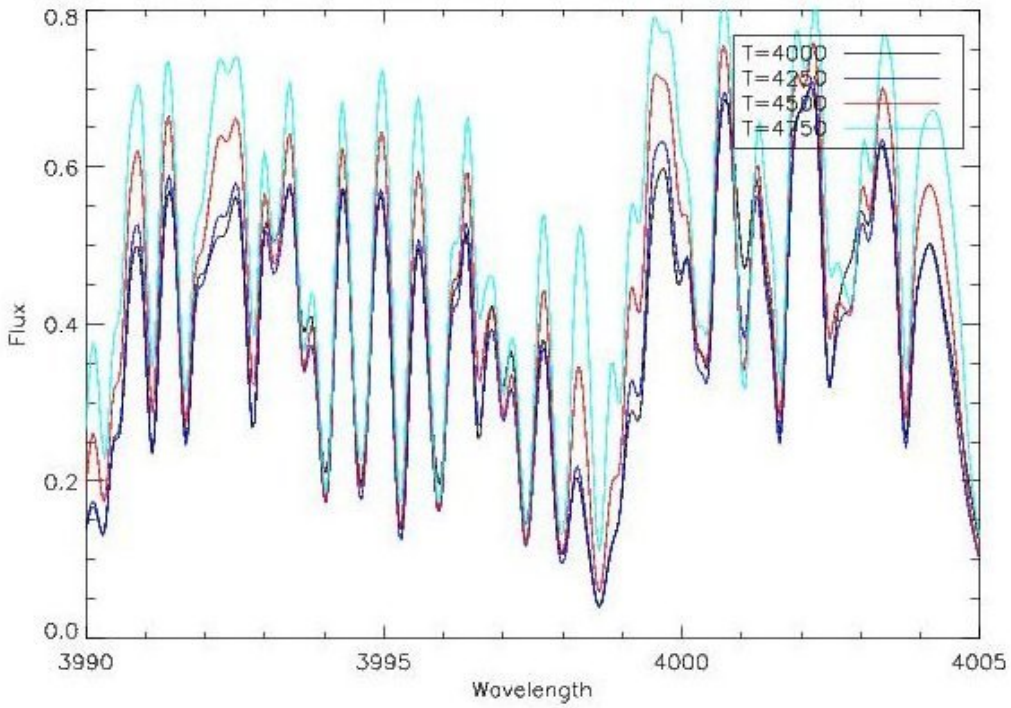

(b)

Figure 5.1: Overplot of synthetic spectra obtained with SYNTHE, with fixed temperature (a) or gravity (b), in the range from 3990 and 4005 Å. (a): The temperature is fixed at $T_{eff} = 4500$K, varying the $\log g$ from 3.0 to 5.0 (b): The gravity is fixed at $\log g = 4.5$ varying the temperature from 4000 to 4750 K.

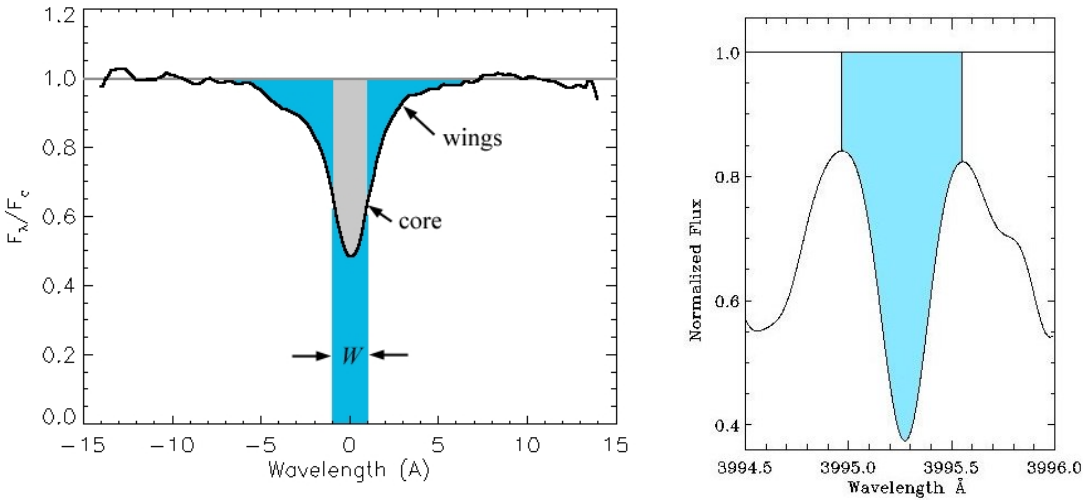

(a) (b)

Figure 5.2: (a) Normalised line profile and equivalent width. The blue-shaded region above the line has the same area as the blue-shaded region below the line, so the equivalent width has the same area as the line itself. (b) Area measured to calculate the EW.

5.2 Errors on equivalents widths

In order to valuate how well I can determine the astrophysical parameters, I need to know which is the precision in the measure of EW in the observed spectra. I measured the EW and their errors, for a sample of stars spectra of NGC2516 cluster (Table 5.4). Following Busà et al. (2007), I assumed:

$$\mathrm{r}(\lambda) \equiv \frac{\mathrm{F}(\lambda)}{\mathrm{F_c}(\lambda)} \tag{5.2}$$

According to Equation 5.1 I get:

$$\mathrm{EW} = \int_{\Delta\lambda} (1 - \mathrm{r}(\lambda))\, \mathrm{d}\lambda \tag{5.3}$$

The uncertainty associated to EW can be derived from the general formula of error propagation, assuming that the main source of error is the statistical noise in the observed normalised profile. From the Equation 5.2:

$$\begin{aligned}
\sigma^2(\mathrm{r}(\lambda)) &= \left(\frac{\partial r(\lambda)}{\partial(F(\lambda))}\right)^2 \sigma^2(F(\lambda)) + \left(\frac{\partial r(\lambda)}{\partial(F_c(\lambda))}\right)^2 \sigma^2(F_c(\lambda)) = \\
&= \frac{F^2(\lambda)}{F_c^2(\lambda)} \frac{\sigma^2(F(\lambda))}{F^2(\lambda)} + \frac{F^2(\lambda)}{F_c^2(\lambda)} \frac{\sigma^2(F_c(\lambda))}{F_c^2(\lambda)} = \\
&= r^2(\lambda) \left[\frac{\sigma^2(F(\lambda))}{F^2(\lambda)} + \frac{\sigma^2(F_c(\lambda))}{F_c^2(\lambda)}\right]
\end{aligned}$$

Since the S/N ratio of the spectrum is $S/N \equiv F_c/\sigma[F_c]$, the above equation becomes:

$$\sigma^2(\mathrm{r}(\lambda)) = \frac{\mathrm{r}^2(\lambda)}{(\mathrm{S/N})^2} \left(1 + \frac{\mathrm{F_c^2}(\lambda)}{\mathrm{F}^2(\lambda)} \frac{\sigma^2[\mathrm{F}(\lambda)]}{\mathrm{F_c}(\lambda)}\right) \tag{5.4}$$

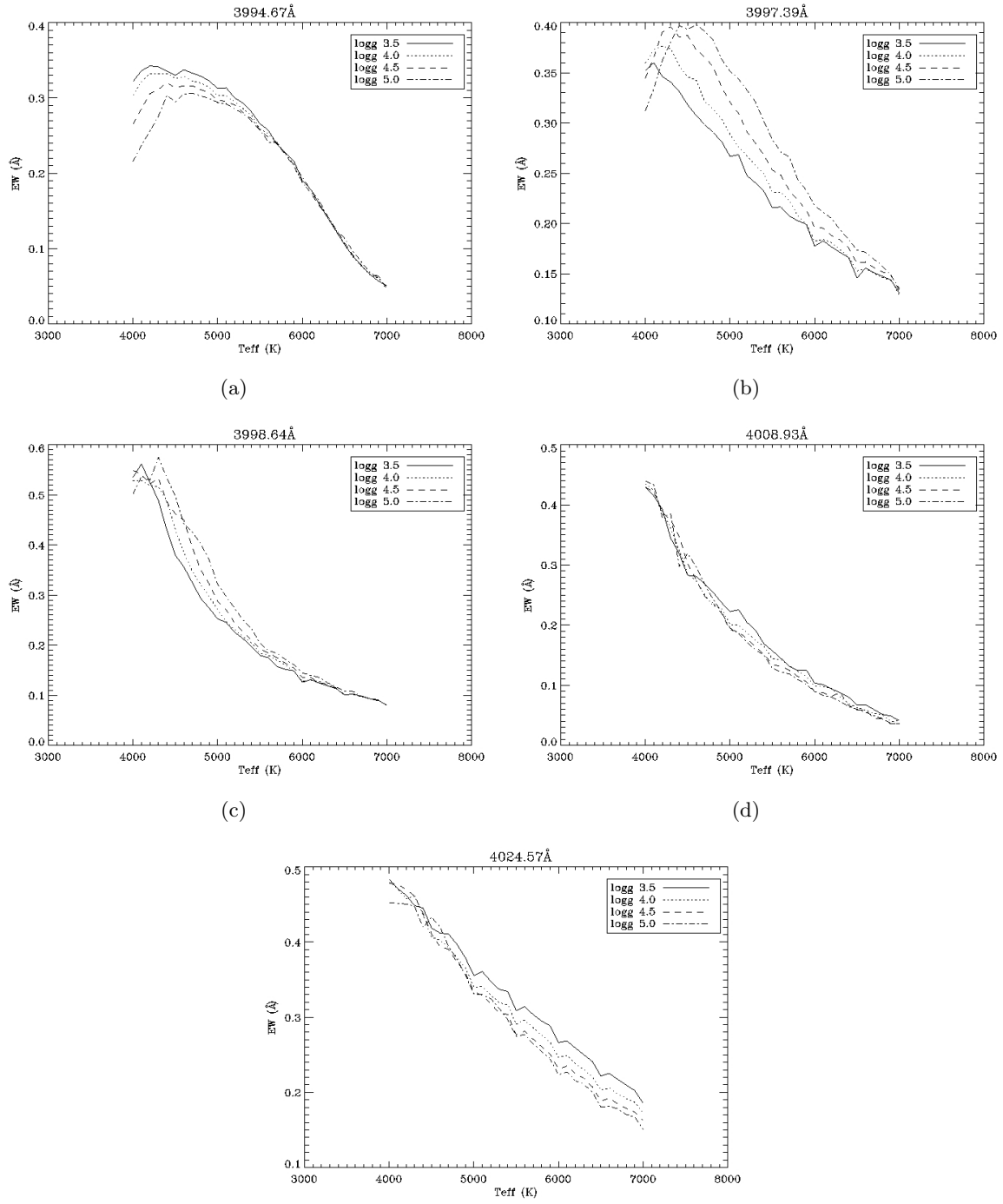

Figure 5.3: Equivalent widths as a function of temperature. The lines are at: (a)3994.67Å, (b)399739 Å, (c)3998.64 Å, (d) 4008.93 Å, 4024.57Å.

Finally, assuming a Poisson error statistics for flux errors, $\sigma^2[\mathrm{F}(\lambda)] \propto \mathrm{F}(\lambda)$, which means $\sigma^2[\mathrm{F}(\lambda)]/\mathrm{F}(\lambda) = \sigma^2[\mathrm{F_c}]/\mathrm{F_c}$, I obtain:

$$\sigma^2(\mathrm{r}(\lambda)) = \frac{\mathrm{r}(\lambda)(1+\mathrm{r}(\lambda))}{(\mathrm{S/N})^2} \tag{5.5}$$

In a numerical integration scheme with prescribed weights, w_i, the residual EW defined in Equation 5.4 is computed as follows:

$$\mathrm{EW} \simeq \Delta\lambda - \sum_{\mathrm{i}} \mathrm{w_i r}(\lambda_\mathrm{i})\delta\lambda \tag{5.6}$$

where $\delta\lambda$ is the wavelength spectral sampling, and the index i runs over the range of line core wavelengths. It follows that:

$$\sigma^2(\mathrm{EW}) = \left(\frac{\partial \mathrm{EW}}{\partial \mathrm{r}(\lambda)}\right)^2 \sigma^2(\mathrm{r}(\lambda)) + \left(\frac{\partial \mathrm{EW}}{\partial \lambda}\right)^2 \delta\lambda^2 = \delta\lambda^2 \sum_{\mathrm{i}} \mathrm{w_i^2}\sigma^2(\mathrm{r}(\lambda_\mathrm{i})) \tag{5.7}$$

In a trapezoidal scheme, $w_i = 1$ for all i, except for the first and last points, where w=1/2.

Once calculated the EW and the correspondent error for each line, I derived the mean error on the measure of EW. I selected lines whose mean error correspond in EW correspond in the EW vs. $\mathrm{T_{eff}}$ relationship a variation of 200 K. Table 5.2 lists the mean value of EW with the mean value of the error on EW. In the first column there is the central wavelength

Table 5.2: Line sensibility for temperature, found for the curve at $\log \mathrm{g} = 4.0$.

λ(Å)	$\overline{\mathrm{EW}}$ (Å)	$\overline{\sigma^2(\Delta\mathrm{EW})}$ (Å)	ΔT(K)
3994.67	0.084	0.005	45
3997.39	0.167	0.010	150
3998.64	0.155	0.011	115
4008.93	0.142	0.012	160
4024.57	0.207	0.012	70

of the lines considered, in the second the mean value of $\overline{\mathrm{EW}}$ and in the third its error $\overline{\sigma^2(\Delta\mathrm{EW})}$. In the fourth column there is the sensitivity on the temperature, derived from the correspondent error on the EW. Figure 5.3 shows the EWs vs. $\mathrm{T_{eff}}$ for the lines selected, in which is rappresented the EW as function of $\mathrm{T_{eff}}$, the ΔT value of Table 5.2, for each line has been derived considering the temperature range correspondent for $\overline{\mathrm{EW}}$ and $\overline{\mathrm{EW}} + \overline{\sigma^2(\Delta\mathrm{EW})}$. Figure 5.3 gives the temperature precision that I can aspect from the correspondent line. I selected lines at: 3994.67, 3997.39, 3998.64, 4008.93 and 4024.57 ÅÅ. Conservatly, I assume that the precision on the inferred temperatures will be of about 200 K.

I did the same analysis for the sensibility of $\log \mathrm{g}$. The lines that show a variation for $\Delta \log \mathrm{g}$ no more than 0.5 are at 3997.39, 3998.64 and 4024.57 ÅÅ

Table 5.3: Line sensibility for $\log \mathrm{g}$.

λ(Å)	$\overline{\mathrm{EW}}$ (Å)	$\overline{\sigma^2(\Delta\mathrm{EW})}$ (Å)	$\Delta \log \mathrm{g}$
3997.39	0.167	0.010	0.5
3998.64	0.155	0.011	0.5
4024.57	0.207	0.012	0.5

5.3 Parameters determination from the EW analysis

The astrophysical parameters of the observed sample, have been determined by comparison between observed and synthetic EWs of the above selected lines.

The estimation of the best model has been done considering the following procedure. For each star, I determined the EW in the different lines, then I made the difference between these ones and the EW for the lines selected of the model. After, I made a weighted mean for each model using the differences for each line, as in equation :

$$\overline{\Delta \mathrm{EW}_{\mathrm{Modelj}}} = \Sigma_{\lambda_\mathrm{i}} \frac{|\Delta \mathrm{EW}_{\lambda_\mathrm{i}}| \cdot \mathrm{w_i}}{\mathrm{N}_{\lambda_\mathrm{i}}} \tag{5.8}$$

where $\Delta \mathrm{EW}_{\mathrm{Modelj}}$ is the medium of the EW differences for each model j, $\Delta \mathrm{EW}_{\lambda_\mathrm{i}}$ is the difference for the between the EW of the star and the model calculated for each line λ_i, w_i is the weight and $\mathrm{N}_{\lambda_\mathrm{i}}$ is the total number of lines. I repeated this procedure for the whole grid of the models and I selected as the best model to reproduce the observation the one with the lowest value of $\overline{\Delta \mathrm{EW}}$.

In order to verify the consistency of this method, I did a test using a solar spectrum at high resolution [2] and applying to it an instrumental broadening similar to the Giraffe one. I used a combination of the lines 3994.67, 3997.39 and 4027.03 ÅÅ, giving them a weight of 1. In this way I obtained a temperature of 5800 ± 200 K and $\log \mathrm{g} = 5.0 \pm 0.5$, compatible with the solar values. In Figure 5.4 are plotted the EWs, of the three lines used for the solar test, for the Sun spectrum (blue) and the synthetic spectrum at 5800 K (red) and $\log \mathrm{g} = 5.0$ derived from the procedure.

Once I made the test for the Sun, I repeated the procedure for the stars of the clusters. Since I know the B − V values for most of the stars of the cluster, I used the relations given by Gray (2005) to estimate the value of the photometric temperature and exclude the stars with $\mathrm{T_{phot}} > 7000$K:

$$\log \mathrm{T_{eff}} = 3.981 + 0.0142\,(\mathrm{B-V}) + 16.3618\,(\mathrm{B-V})^2 + 81.8910\,(\mathrm{B-V})^3 + 161.5076\,(\mathrm{B-V})^4 \tag{5.9}$$

for $\mathrm{B-V} < 0.00$, and for $0.00 \leq \mathrm{B-V} \leq 1.5$:

$$\log \mathrm{T_{eff}} = 3.981 - 0.4728\,(\mathrm{B-V}) + 0.2434\,(\mathrm{B-V})^2 - 0.0620\,(\mathrm{B-V})^3 \tag{5.10}$$

From these relations, I derived the error on the $\mathrm{T_{eff}}$, using the propagation of error formula and assuming no errors on the coefficients of Equations 5.9 and 5.10. I assume $\mathrm{x} = \mathrm{B-V}$ obtaining:

$$\delta \mathrm{T} = \frac{\partial \mathrm{T}}{\partial \mathrm{x}} \delta \mathrm{x} = \mathrm{T} \ln 10\ (0.0142 + 2 \cdot 16.3618\mathrm{x} + 3 \cdot 81.8910\mathrm{x}^2 + 4 \cdot 161.5076\mathrm{x}^3) \delta \mathrm{x} \tag{5.11}$$

[2] `http://bass2000.obspm.fr/solar_spect.php`

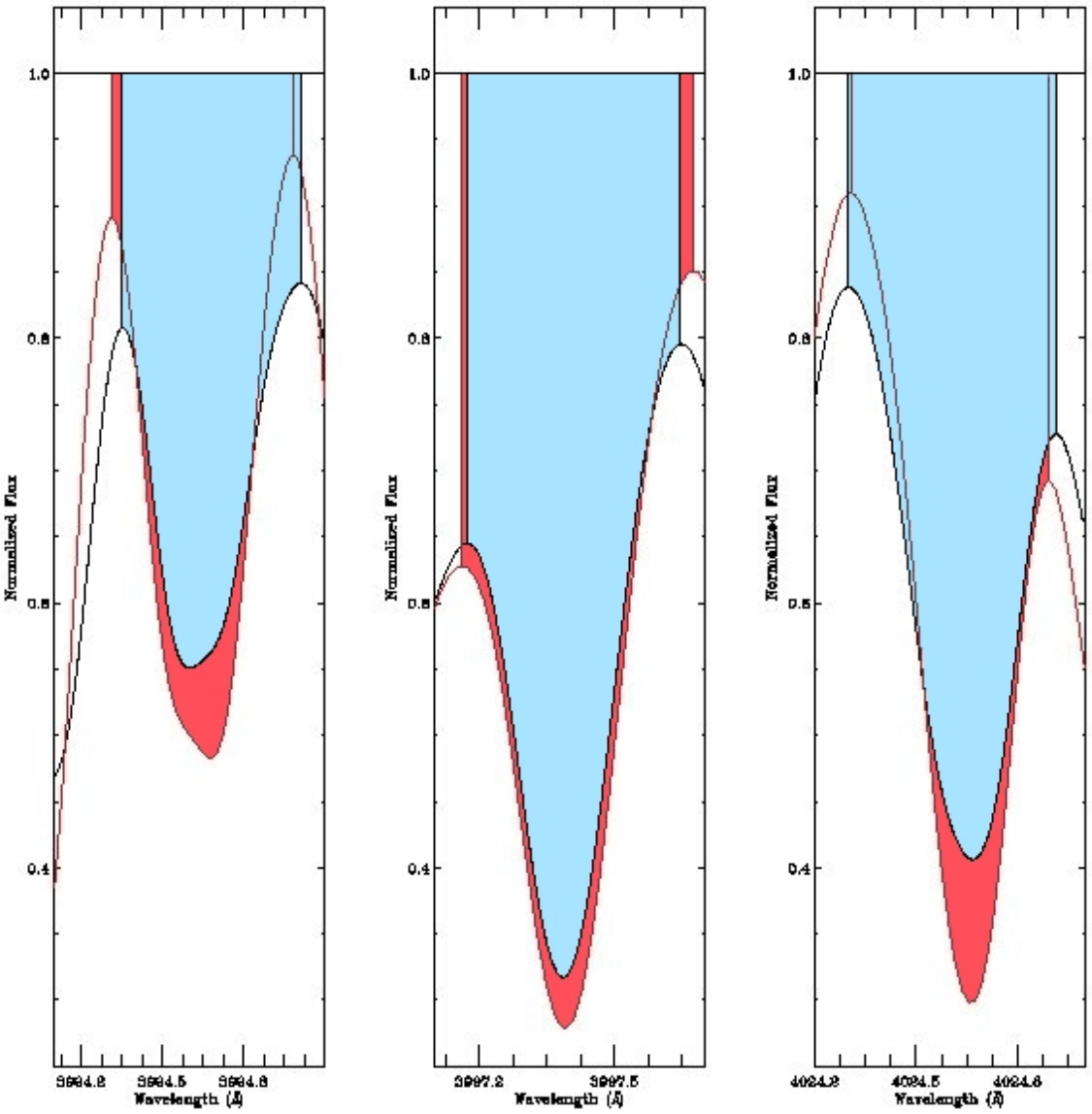

Figure 5.4: EW widths for the spectrum of the Sun (blue) and a synthetic spectrum of 5800 K (red) and $\log g = 5$

for $B - V < 0.00$ and for $0.00 \leq B - V \leq 1.5$:

$$\delta T = \frac{\partial T}{\partial x}\delta x = T \ln 10 \ (-0.4728 + 2 \cdot 0.2434x - 3 \cdot 0.0620x^2)\delta x \tag{5.12}$$

Photometric temperatures have been used as a first estimate of temperature in the parameters determination procedure. The parameters of the stars' cluster have been derived using the lines of Table 5.2, given a different weight to each line. I assumed a weight 1 for the lines that give useful information, and 0 to the others. In particular, for stars with $T_{phot} < 5800$K I considered the lines 3997.39, 3998.64, 4008.93 Å while for $T_{phot} > 5800$K I considered the lines 3994.67, 3997.39, 4024.57 Å. Stellar parameters obtained for all the stars are listed in Table 5.4, together with the photometric temperature and the difference between photometric

and spectroscopic temperatures.

The derived spectroscopic temperatures have been plotted versus the photometric temperatures in Figure 5.3 (left). It is worth to note that, most of the spectroscopic temperatures obtained are greater than the photometric ones. For some stars of the cluster, the residuals (Figure 5.3 (right)) show a difference greater than 200K. For this reason I realised that the use of this range to made a determination of the stellar parameters is not a good choice, and if possible, it is better to consider a different one. However, in the case of Giraffe spectra in the HR2 band, only a reduced part of the spectrum is available for this kind of analysis, and probably the use of a photometric temperature, if the colour indices are available, could gives a more precise estimation.

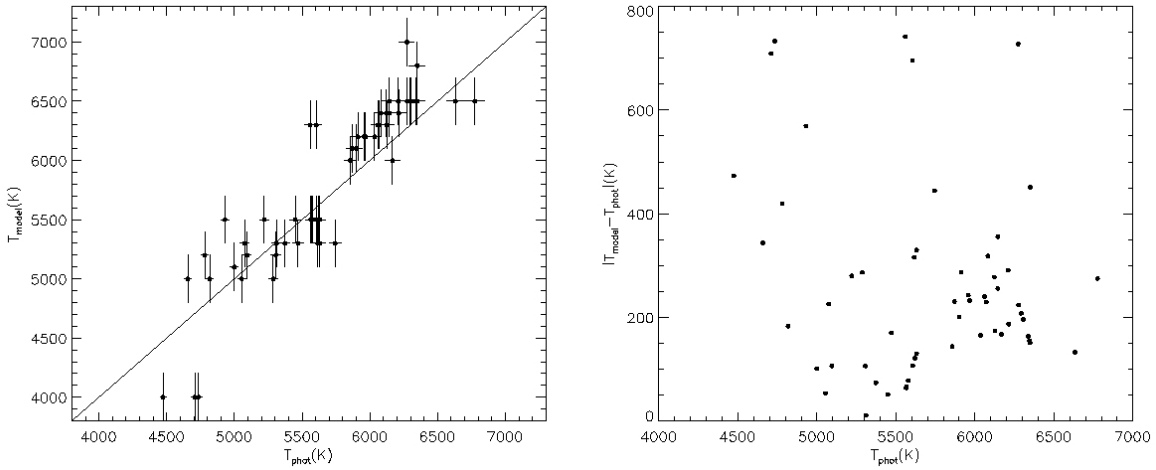

Figure 5.5: Left: Scatter plot of the photometric temperature (abscissa) and the temperature found in the model (ordinate). Right: Residuals between the photometric temperature and the temperature derived from the models vs. the photometric temperature.

Table 5.4: Model which best reproduce the stars of the cluster NGC2516. In the first three columns there are the name, the photometric temperatures and errors for the stars of the cluster NGC 2516, derived from (Jeffries et al., 2001). In the fourth column there is the name of the derived model and in the last column there is the absolute value of the difference between the spectroscopic temperature, derived from the model, and the photospheric temperature.

JTH	T_{phot}	$e(T_{phot})$	modelname	ΔT	JTH	T_{phot}	$e(T_{phot})$	modelname	ΔT
4670	4999.04	29.0747	5100g4.0ap00k0	100.960	7621	4780.50	25.8072	5200g3.5ap00k0	419.502
5626	6774.65	68.8876	6500g5.0ap00k0	274.646	7676	6336.84	57.8715	6500g5.0ap00k0	163.160
5702	6304.32	57.0738	6500g5.0ap00k0	195.676	7864	6345.03	58.0731	6500g5.0ap00k0	154.966
5833	6349.15	58.1743	6500g5.0ap00k0	150.854	7941	6059.70	51.1779	6300g5.0ap00k0	240.303
5862	5869.47	46.7397	6100g5.0ap00k0	230.531	7967	6209.45	54.7642	6500g5.0ap00k0	290.553
5901	6081.52	51.6957	6400g5.0ap00k0	318.484	7998	4656.65	24.2951	5000g3.5ap00k0	343.350
6029	6070.58	51.4360	6300g5.0ap00k0	229.418	8139	5630.00	41.3768	5500g3.5ap00k0	130.005
6106	6632.41	65.2561	6500g4.5ap00k0	132.408	8205	6272.26	56.2903	7000g5.0ap00k0	727.736
6144	4708.82	24.8986	4000g5.0ap00k0	708.818	8270	4733.62	25.2028	4000g5.0ap00k0	733.619
6263	5373.54	35.9884	5300g3.5ap00k0	73.5415	8411	5470.25	37.9701	5300g3.5ap00k0	170.251
6307	5448.90	37.5269	5500g3.5ap00k0	51.1035	8536	6122.10	52.6633	6400g4.5ap00k0	277.895
6331	5957.25	48.7701	6200g4.5ap00k0	242.752	8689	5220.06	32.9921	5500g3.5ap00k0	279.938
6452	6034.51	50.5824	6200g5.0ap00k0	165.490	8725	4473.15	22.5974	4000g4.5ap00k0	473.153
6501	5967.61	49.0120	6200g5.0ap00k0	232.386	8923	5074.65	30.3545	5300g3.5ap00k0	225.349
6605	5621.25	41.1862	5500g3.5ap00k0	121.247	9140	5856.29	46.4376	6000g4.5ap00k0	143.711
6649	5606.74	40.8714	5500g3.5ap00k0	106.740	9146	5053.32	29.9866	5000g3.5ap00k0	53.3198
6676	5286.63	34.2675	5000g3.5ap00k0	286.629	9286	5306.12	34.6481	5200g3.5ap00k0	106.122
6705	5094.08	30.6941	5200g3.5ap00k0	105.922	9449	5899.43	47.4292	6100g4.5ap00k0	200.569
6852	5630.00	41.3768	5300g3.5ap00k0	330.005	9465	5603.85	40.8088	6300g4.5ap00k0	696.150
6880	5615.43	41.0599	5300g3.5ap00k0	315.433	9475	5563.88	39.9482	5500g3.5ap00k0	63.8833
6994	6144.56	53.2010	6500g5.0ap00k0	355.440	9852	6125.83	52.7524	6300g5.0ap00k0	174.170
7104	6213.32	54.8580	6400g4.5ap00k0	186.676	10315	6167.25	53.7460	6000g4.5ap00k0	167.250
7312	5566.71	40.0088	5500g3.5ap00k0	66.7124	10390	6144.56	53.2010	6400g4.5ap00k0	255.440
7485	5744.54	43.9072	5300g3.5ap00k0	444.536	10526	6276.25	56.3874	6500g5.0ap00k0	223.754
7564	4930.48	27.9762	5500g3.5ap00k0	569.520	10894	6292.25	56.7784	6500g5.0ap00k0	207.750
7585	5912.89	47.7401	6200g4.5ap00k0	287.110	11233	5558.24	39.8275	6300g4.5ap00k0	741.761
7594	4817.34	26.3079	5000g3.5ap00k0	182.656	11304	5311.03	34.7445	5300g3.5ap00k0	11.033
7595	6349.15	58.1743	6800g5.0ap00k0	450.854	11366	5578.06	40.2524	5500g3.5ap00k0	78.062

Chapter 6

Analysis

In this Chapter I present the analysis made on NGC2516 and NGC3766. In the first section I discuss the NGC2516 memberships, after deriving the radial velocities for the stars studied. In the second section I derived the chromospheric indices R'_{hk} by means method of Linsky et al. (1979b). In the third section I made a test using some stars' spectra observed by FEROS[1] to compare the R'_{hk} derived by using the method of Linsky et al. (1979b) with the one of Noyes et al. (1984). Finally, in the last two sections I describe the lithium abundance derivation for both clusters NGC2516 and NGC3766.

6.1 Membership and radial velocities of NGC2516

The first step to determine the physical parameters of an open cluster is to select probable members in the vicinity of this cluster. Various methods based on the analysis of positions, proper motions, radial velocities, magnitudes and their combinations have been proposed to determine the members of open clusters. These methods can be divided into two main groups: photometric and kinematic (Cabrera-Cano & Alfaro, 1990). The statistical analysis of proper motions is the most widely used method, but, unfortunately, few clusters have a large, homogeneous radial velocity database to allow a detailed analysis of the entire cluster. It is well known that the proper motion analysis is, up to now, the most valuable criterion to establish membership probabilities in open clusters (Cabrera-Cano & Alfaro, 1985). However, these methods need high precision proper motion data and these ones also need several decades to be accurately measured. Colour-magnitude diagrams or colour-colour diagrams are used to derive the fundamental parameters of clusters, and in general, are also used to determine the membership of clusters (Meibom, 2000). However, it is much more difficult to determine the members of cluster just based only on colour-magnitude diagrams or colour-colour diagrams without knowing any physical parameters of cluster.

[1]FEROS is an high-resolution(R$\sim$48,000) astronomical Échelle spectrograph operating at ESO, providing in a single spectrogram the complete spectral coverage from 350nm to 920nm.

For the open cluster NGC2516, I collected the information found by different authors in Table 6.1. The proper motion probability are from (King, 1978) (taken from WEBDA), the photometric membership is from Jeffries et al. (2001) and Damiani et al. (2003) and the rotational membership is taken from Terndrup et al. (2002) and Jeffries et al. (1998).

Furthermore, I determined the radial velocities of NGC2516's stars considering stars in the CaII band (not for the ones observed in the lithium band due to the low time of exposure). The mean value for the radial velocity cluster, determined by different authors, is listed in Table 6.2. Radial velocities of the cluster have been computed using the function giCrossC of the GIRAFFE girBLDRS pipeline, which takes a template spectrum and cross-correlates it with each observed star. I made a cross-correlation between all the observed spectra and three different synthetic templates spectra corresponding to a F0 (for $B - V < 0.44$), G2 (for $0.44 < B - V < 0.68$) and K0 (for $B - V > 0.68$) spectral type stars. The results for stars where the V_{rad} has been determined are in Table 6.3. The radial velocities calculated have been used to shift the stars to the rest reference system. As an example, the portion of the spectra from 4030 to 4037 Å is plotted in Figure A.1.

In Figure 6.1 are plotted stars of Table 6.3 with two gaussian fit with two different mean and standard deviation. The dotted fit is obtained considering the mean and the standard

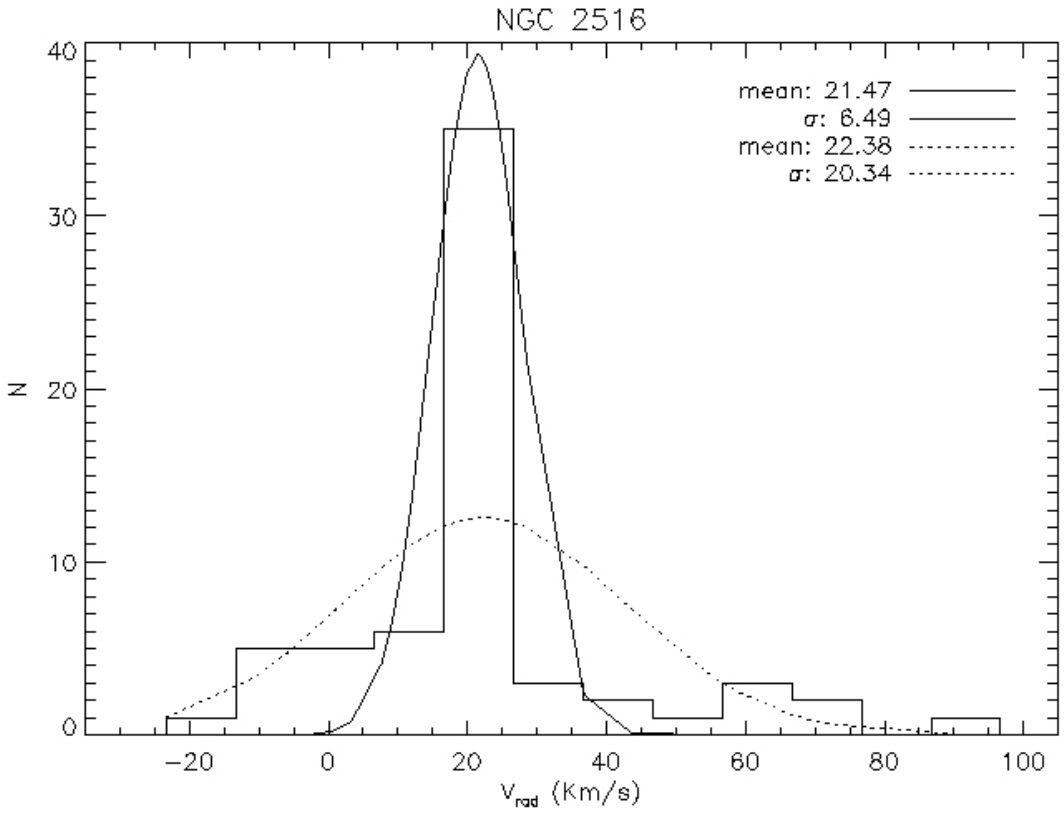

Figure 6.1: Radial velocity distribution of the stars of the cluster NGC2516 for which the radial velocity has been determined.

Table 6.1: In the first two columns there are the numbering system and the photometric membership of (Jeffries et al., 2001), in the third column there is the rotational membership of Terndrup et al. (2002) and Jeffries et al. (1998), while in the fourth column gives the membership of Damiani et al. (2003), where N means not member and Y member. PM is the membership probability derived from the proper motion(King, 1978) as found in WEBDA.

N	Jeffries	Terndrup	Damiani	PM	N	Jeffries	Terndrup	Damiani	PM
4670	N				7967	Y	Y	Y	
5626	Y				7998	N			
5702	N		N		8099	Y			
5833	Y	Y			8139	N			
5862	Y	Y	Y		8172	Y			
5901	Y	Y			8205	N			
6029	Y	Y	Y		8262	Y	N		
6106	Y		Y		8270	N		N	
6144	N				8340	Y			0.99
6157	N				8411	Y		Y	
6263	Y	Y	Y		8435	N		N	
6307	N	N			8458	Y	Y	Y	0.99
6331	N				8536	Y	Y	Y	
6373	Y	Y		0.98	8660	Y	Y		
6452	Y	Y	Y		8689	Y	N	Y	
6501	Y	N			8725	N			0.0
6588	N				8920	Y			
6605	Y		Y		8923	Y		Y	
6649	Y	N	Y		9048	Y	Y		0.99
6676	Y	Y			9054	Y	Y	Y	
6705	Y	N			9140	Y	Y	Y	
6724	Y		N		9146	Y			
6852	Y	Y	Y		9175	Y	Y		0.98
6880	Y	Y			9286	Y	Y	Y	
6994	N				9328	Y		Y	
7104	Y	Y	Y		9449	N			
7312	Y	Y	Y		9465	Y	Y	Y	
7466	N				9475	Y	N		
7485	N		N		9696	Y			
7564	N				9852	Y	Y	Y	
7585	Y	Y	Y		9882	Y	Y		0.99
7594	N				10021	N	Y		
7595	Y		Y		10315	N			0.0
7619	Y	Y	Y		10390	N	N		
7621	N				10526	N			
7650	Y	N	Y		10863	Y		Y	
7676	N				10894	Y		Y	
7743	Y	Y	Y		10940	N			
7784	N				11233	Y		Y	
7864	Y	Y	Y		11304	Y			
7941	Y				11307	Y	Y		
7962	Y		Y		11366	N		N	

Table 6.2: Radial velocity study for the cluster NGC2516. In the first column there is the name of the author, in the second there is the mean value of V_{rad}. and in the third there is the number of stars studied.

Author	$V_{rad}[Km/s]$	N
Jeffries et al. (1998)	23.8 ± 0.3	24
González & Lapasset (2000)	22.0 ± 0.2	22
Terndrup et al. (2002)	24.2 ± 0.2	57

deviation of all the stars in Table 6.3. Then, I considered only the stars in the range [$\bar{x}-\sigma$, $\bar{x}$ $+\sigma$], obtaining the solid line fit. The stars studied by Terndrup et al. (2002) (Table 3.2) have been correlated with the ones calculated by means the giCrossC task of GIRAFFE (Table 6.3) and the cross-correlation is showed in Figure 6.2. I can see that except for three stars (that could be binary stars not resolved), the others shows a good agreement with the sample of Terndrup et al. (2002).

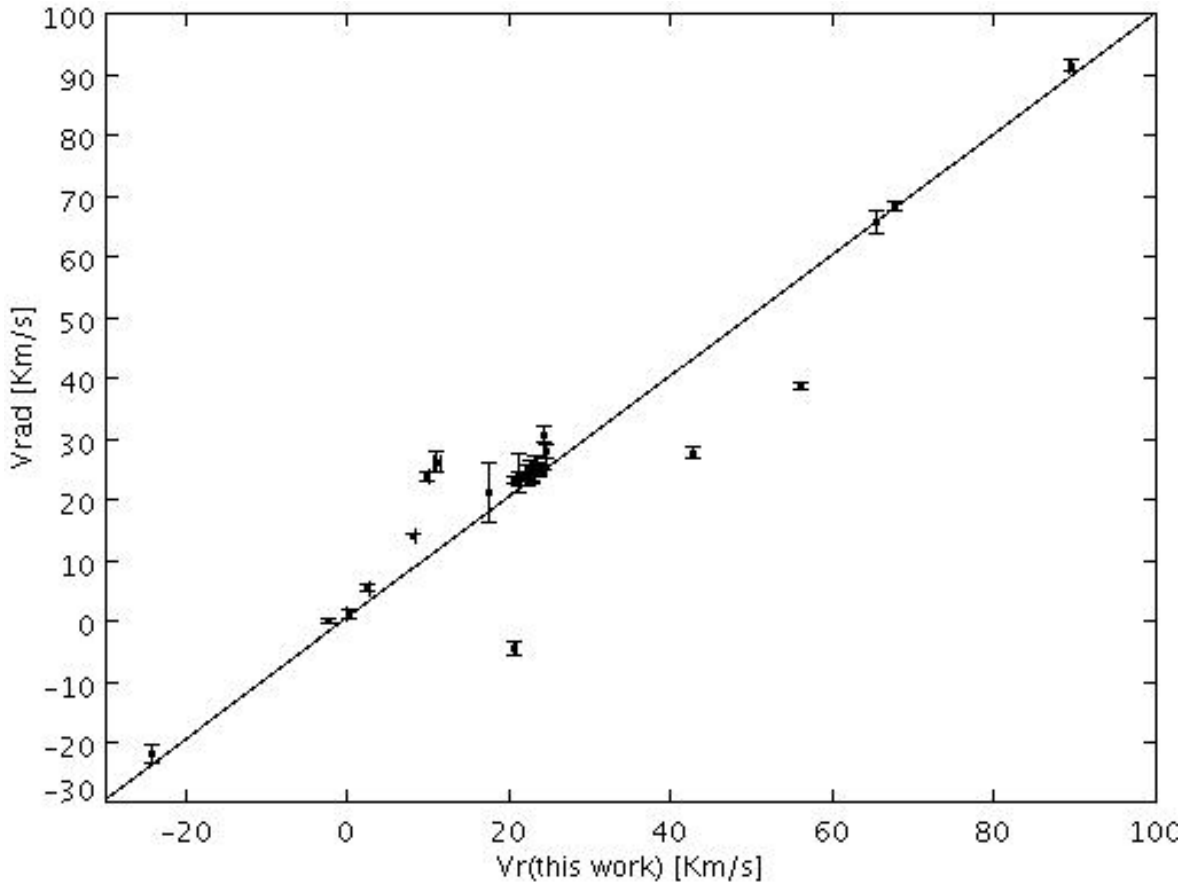

Figure 6.2: Cross correlation between the radial velocities calculated by Terndrup et al. (2002) and Jeffries et al. (1998) with the ones found by the task giCrossC.py of girBLDRS.

Considering the different membership listed in Table 6.1 and the information about the binarity exposed in Table 3.2. I can deduce which stars are not members of the cluster and binaries. In Table 3.2 there are in the first column the numbering system of Jeffries et al.

(2001), and inthe second and third the V_{rad} and their errors as found using the task giCrossC.

Table 6.3: Stars of the clusters NGC 2516 for which the V_{rad} and associated errors for our targets have been determined. In the first column there is the number in the nomenclature of Jeffries et al. (2001), and in the second and third the V_{rad} and their errors as found using the function giCrossC. **Bold** are binary stars stars as already derived by Jeffries et al. (2001). ~~Struck-out~~ stars have been rejected because their velocity is significantly different to the medium velocity found by Terndrup et al. (2002) and in this table, or because they are considered as not member in Table 6.1. This suggests the possibility that they are binary stars or not members of the cluster.

JTH	V_{rad}	$e(V_{rad})$	JTH	V_{rad}	$e(V_{rad})$	JTH	V_{rad}	$e(V_{rad})$
~~4670~~	59.298	0.091	7312	24.558	0.048	**8536**	23.478	0.042
~~5702~~	-4.307	0.114	7466	12.132	0.042	~~8689~~	-1.48	0.072
5833	22.025	0.072	~~7485~~	18.182	0.023	~~8725~~	10.292	0.009
5862	24.472	0.050	**7564**	19.912	0.051	**8923**	24.409	0.060
5901	23.506	0.036	**7585**	25.141	0.050	**9054**	25.3	0.047
6029	21.436	0.021	7594	28.574	0.032	9140	22.043	0.044
6106	22.912	0.038	7595	22.769	0.046	**9146**	-10.408	0.052
~~6144~~	-1.025	0.028	7619	24.048	0.069	9286	25.248	0.051
6157	16.743	0.158	~~7621~~	54.737	0.045	9328	17.976	0.059
6263	23.769	0.050	~~7650~~	66.296	0.057	9449	28.504	0.040
~~6307~~	0.965	0.075	~~7676~~	-7.432	0.042	9465	11.958	0.427
6331	7.746	0.041	**7864**	43.607	0.032	**9475**	68.716	0.040
6452	22.987	0.029	7941	23.478	0.042	**9852**	23.668	0.021
~~**6501**~~	-23.319	0.022	7967	23.751	0.061	~~10315~~	72.108	0.007
6605	21.853	0.041	~~8139~~	-3.282	0.065	~~10390~~	56.841	0.017
~~6649~~	3.363	0.069	8205	36.627	0.045	~~10526~~	-11.138	0.051
6676	24.641	0.056	~~8262~~	9.024	0.048	10863	25.654	0.071
~~**6705**~~	90.279	0.081	~~8270~~	17.346	0.023	10894	23.461	0.033
6852	23.058	0.037	8411	22.72	0.058	**11233**	21.648	0.072
6880	10.73	0.034	~~8435~~	37.008	0.183	11304	23.319	0.043
~~6994~~	-5.963	0.051	**8458**	18.32	0.092	~~11366~~	23.695	0.048
7104	24.078	0.048						

Finally I compared the stars for which the photometry is available, with the models of Baraffe et al. (1998). I determined the absolute V-band magnitude (M_V), using the observed V-band magnitude (V) and the parallax ($\pi = 2.89 \pm 0.21$mas) of Robichon et al. (1999), and assuming no extinction, it reads:

$$M_V = V + 5\log(\pi) + 5 - 3.1 \cdot E(B-V)$$

In Figure6.3 is plotted the colour-magnitude diagram, together with models of different ages. As one can see, all the isochrones from 100 to 150 Myr fit quite well the main sequence in the range considered. This because the isochrone method is mostly good for PMS cluster, while the age of NGC2516 is estimated to be around 150Myr.

However, one can clearly see which stars are distant enough from the MS to be considered not members or binaries. Most of the cooler stars are too distant from the main sequence,

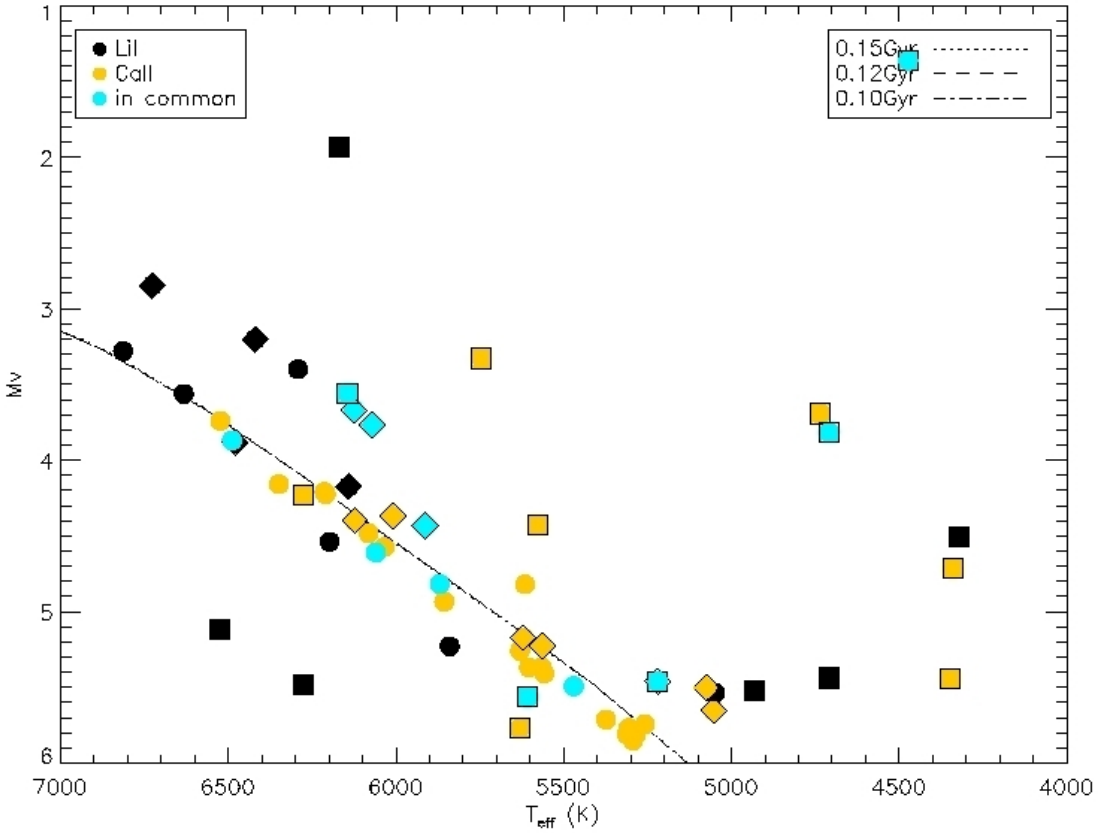

Figure 6.3: NGC2516 HR diagram. Photometry is taken from Jeffries et al. (2001). Black symbols indicate stars for which I measured Li abundance, yellow symbols for CaII H&K measurements, and blue symbols are used for measurements of both. The isochrones computed by Baraffe et al. (1998) at 0.10, 0.12, and 0.15 Gyrs. ♦ are probably binaries while ■ are not members.

and have been considered clearly not members. Stars in a limited range above the MS could be binaries members of the cluster.

6.2 Chromospheric index measurements for NGC2516

The chromospheric index is based on the CaII lines, very sensitive to chromospheric activity and extensively studied. The most sensitive area is comprised between the minima, but it is hard to discriminate it in stars with low activity or with low SNR. The distance between the minima is usually close to 1Å centered in the line core. I calculated the absolute H and K emission line fluxes with the method of Linsky et al. (1979b), as discussed in section 2.4.2. The calculations have been performed using a routine which I wrote in the IDL language.

Like Strassmeier et al. (2000), I obtained all the relative fluxes by integrating the appropriate bandpass between the not-normalised spectrum and zero intensity. The absolute emission line fluxes, $\mathcal{F}$, have been calculated by comparing the ratio of the relative H and K

line flux and the relative 50Å flux with a linear extrapolation of the absolute flux from the $V-R$ colour index relation given by Linsky et al. (1979b) based upon the absolute photometry of Willstrop (1965) (Equations 2.14 and 2.15). The integral f($\Delta\lambda = 50$Å) includes the H and K emission features but the calibration of $\mathcal{F}(\Delta\lambda = 50\text{Å})$ is derived from different kind of stars, selected without much regard to their H and K characteristics.

In order to derive $\mathcal{F}$ absolute fluxes, I used the photometric data of Jeffries et al. (2001). However, since their catalogue does not include $V-R$ colours, these ones have been computed from their $B-V$ colours, correcting them for the reddening, using the $E(B-V) = 0.12$ given by (Terndrup et al., 2002) and then using the conversion table of (Cox, 2000). Using $B-V$ instead of an observed $V-R$ value seems to minimise the effects of cool starspots and it has been shown by many authors (Strassmeier et al., 1994) to be a more consistent description of the unspotted photosphere. I then derived $\mathcal{F}_{\rm H}$ and $\mathcal{F}_{\rm K}$ using Equation 2.19.

After the surface fluxes in the cores of H and K lines have been determined, the flux arising from the underlying photosphere must be subtracted. As demonstrated by Linsky & Ayres (1978), the resulting excess flux is the net chromospheric radiative loss in the H and K lines, respectively. Linsky et al. (1979b) present (see Figure 2.15) the H and K indices for radiative equilibrium model atmospheres $\mathcal{F}^{\rm RE}_{\rm H;K}$ which can be used to derive the radiative losses, representing the purely chromospheric emission flux $\mathcal{F}'_{\rm H;K}$ (Equations 2.16 and 2.17). Furthermore, I compute the sum of the corrected fluxes in the H and K line and express it in units of the bolometric luminosity, using the Equation 5.9 of Gray (2005) to estimate the value of the photometric temperature from $B-V$. At the end I derived:

$$\mathrm{R'_{HK}} = \frac{\mathcal{F}'_{\rm H} + \mathcal{F}'_{\rm K}}{\sigma\ \mathrm{T^4_{eff}}}$$

In Figure 6.4 are shown all the $\log \mathrm{R'_{HK}}$ measurements versus corrected B-V. The plot is annotated with star's name and overplotted is a linear fit obtained. A relation between the two quantities seems to be evident, as assumed by Mamajek & Hillenbrand (2008), but even their dependence is not well parameterized. As one can see, the slope of the fit is negative. As shown in Figure 1.3, the younger clusters seem to have a positive slope, while the old ones, such as M67, have a negative slope. Moreover, since the scatter in young cluster is high, it is difficult to derive the real trend of each cluster. Furthermore, the paucity of the sample studied are in my opinion not enough to establish the real trend of this cluster.

In Figure 6.5 of the data derived for NGC2516 (see Table 6.4) have been compared to the ones of other cluster of different ages, such as Pleiades (130Myr), Hyades (625Myr) and M67 (4Gyr). All the data for these clusters are taken from Mamajek & Hillenbrand (2008). For each cluster I derived the corresponding level of $\log \mathrm{R'_{HK}}$ (horizontal lines), using the relation

between the mean value of $\log R'_{hk}$ and the age given in Mamajek & Hillenbrand (2008):

$$\log R'_{hk} = 8.94 - 4.849 \log \tau + 0.624(\log \tau)^2 - 0.028(\log \tau)^3$$

that is the inverse of

$$\log \tau = -38.053 - 17.912 \log R'_{hk} - 1.6675 \log(R'_{hk})^2$$

τ is the age in years, and the fit is appropriate in the range [-4.0; -5.1] for $\log R'_{hk}$ and [6.7;9.9] for $\log \tau$. These relationships are valid in the range of $0.5 < B-V < 0.9$, and have a precision of 0.2 dex in log Age for stars older than Hyades. With these assumptions I determined from the mean value of the $\log R'_{hk}$ in the range of $B-V$, the chromospheric age, from equation above, obtaining 140Myr. But as explained in section 1.3, for clusters close to the Pleiades' age, the determination of the chromospheric age is quite imprecise. The same problem is with the isochrone age, since the NGC2516's age is greater than 20Myr. For this reason the best way to determine the age for clusters not on the PMS should be the lithium abundances depletion.

In Figure 6.6 are shown the $\log R'_{HK}$ measurements versus projected rotational velocity ($v \sin i$) of stars in NGC2516. As expected, the $\log R'_{HK}$ measurements are correlated with $v \sin i$; the most rapidly rotating stars have, on average, the largest $\log R'_{HK}$ values. However,

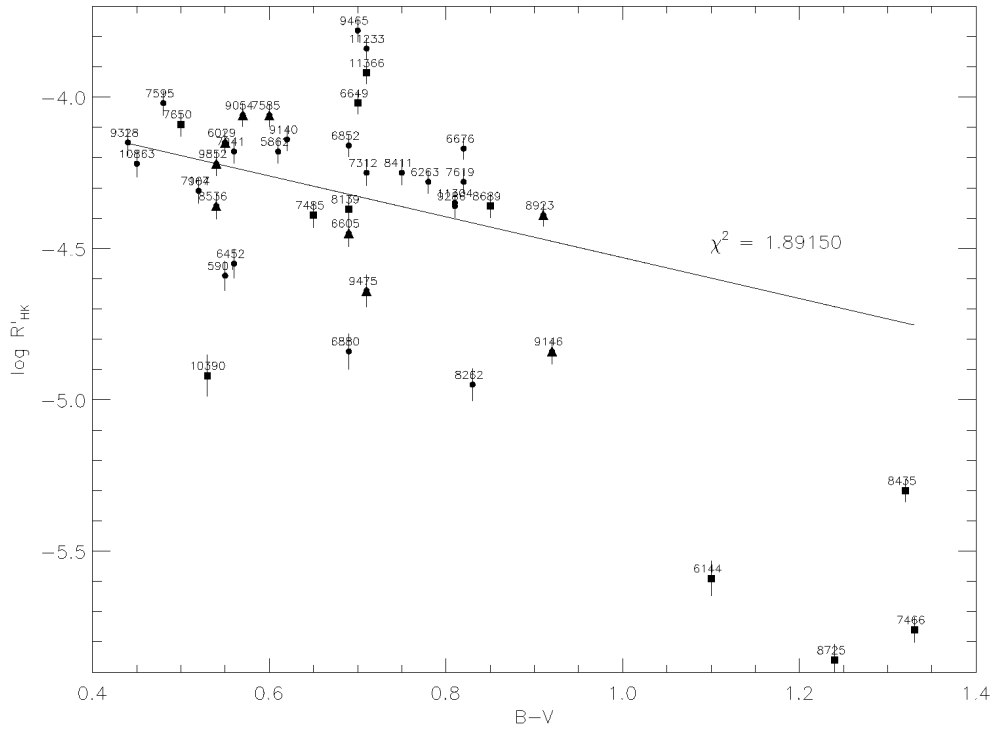

Figure 6.4: CaII H&K emission versus $B-V$. The fit is obtained considering only the members. ■ and ▲ are data of likely non-members and binaries, respectively.

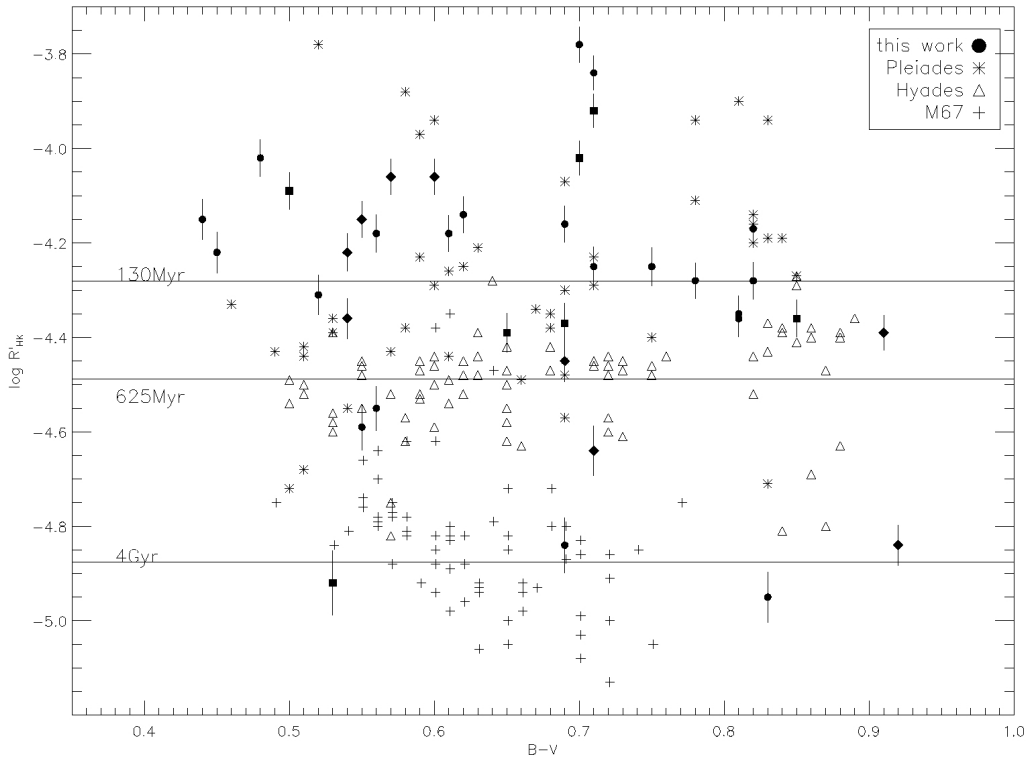

Figure 6.5: CaII H&K emission versus B − V compared with cluster of different ages (data are from Mamajek & Hillenbrand (2008)). ■ and ▲ are data of likely non-members and binaries, respectively.

Figure 6.6 also indicates that once the $v \sin i$ values increase above $\sim 20 \mathrm{kms}^{-1}$, the $\log R'_{HK}$ values stay roughly constant, implying no increase in the CaII H and K emission-line flux toward larger rotation rates.

White et al. (2007) assume that the saturation of the CaII H and K flux seems consistent with other chromospheric and coronal observations of rapidly rotating stars, and is not connected to the method used to derive the $\log R'_{HK}$. Indeed, they used the Mount Wilson method which involves measuring the CaII K and H emission with a triangular passband of specified width. For this reason apparent saturation could be caused by emission-line flux being rotationally broadened outside of this passband, and thus not included in the measurement. But they showed that the technique used to measure the S values begins to miss core emission flux above $v \sin i$ of $\sim 100 \mathrm{kms}^{-1}$. Moreover, I observe the same trend using another method to derive the R'_{HK}. For this reasons, since the saturation observed for R occurs well below this value, I interpret the saturation as a real effect.

In Figure 6.7 I plotted $\log R'_{HK}$ measurements versus the V_{rad} measurements derived in section 6.1. As one can see, most of the stars that show a V_{rad} distant from the mean value of R'_{hk} and V_{rad} of the cluster are not members or binaries. Only two of them seems to stay distant from the other group of stars, even if considered as members.

Table 6.4: Chromospheric activity measured for targets in the open cluster NGC 2516. Columns report: identifier, corrected B − V and e(B − V) from Jeffries et al. (2001). V-R and their errors are derived from B − V. T_{eff} and their errors are determined from B − V and relation of Gray (2005). R'_{hk} is determined as discussed above. H-K is the difference in counts between the H and K lines.

name	B-V_0	V-R	T_{eff}	eT_{eff}	R'_{hk}	eR'_{hk}	log R'_{hk}	e log R'_{hk}	H-K
5862	0.61	0.52	5869.47	46.74	6.63E-5	5.89E-6	-4.18	0.037	-80.54
5901	0.55	0.49	6081.52	51.7	2.55E-5	2.85E-6	-4.59	0.049	-19.36
6029	0.55	0.49	6070.58	51.44	7.1E-5	6.34E-6	-4.15	0.038	-113.92
6144	1.10	0.94	4708.82	24.9	2.57E-6	3.4E-7	-5.59	0.058	-199.71
6263	0.78	0.62	5373.54	35.99	5.22E-5	4.58E-6	-4.28	0.038	-83.17
6452	0.56	0.49	6034.51	50.58	2.79E-5	3.01E-6	-4.55	0.047	29.88
6605	0.69	0.55	5621.25	41.19	3.55E-5	3.53E-6	-4.45	0.043	-36.96
6649	0.70	0.55	5606.74	40.87	9.46E-5	7.98E-6	-4.02	0.037	44.21
6676	0.82	0.65	5286.63	34.27	6.74E-5	5.59E-6	-4.17	0.036	19.34
6852	0.69	0.55	5630.00	41.38	7.0E-5	6.11E-6	-4.16	0.038	-14.46
6880	0.69	0.55	5615.43	41.06	1.44E-5	1.93E-6	-4.84	0.058	-33.8
7104	0.52	0.47	6213.32	54.86	4.94E-5	4.73E-6	-4.31	0.042	-112.48
7312	0.71	0.56	5566.71	40.01	5.57E-5	5.34E-6	-4.25	0.042	-178.18
7466	1.33	1.19	4339.90	21.81	1.73E-6	1.63E-7	-5.76	0.041	-6.88
7485	0.65	0.53	5744.53	43.91	4.11E-5	3.94E-6	-4.39	0.042	-366.5
7585	0.60	0.51	5912.89	47.74	8.66E-5	7.48E-6	-4.06	0.038	8.89
7595	0.48	0.44	6349.14	58.17	9.59E-5	8.68E-6	-4.02	0.039	-739.9
7619	0.82	0.65	5293.92	34.41	5.26E-5	4.72E-6	-4.28	0.039	-212.79
7650	0.50	0.45	6276.25	56.39	8.09E-5	7.26E-6	-4.09	0.039	39.76
7941	0.56	0.49	6059.70	51.18	6.56E-5	5.94E-6	-4.18	0.039	-141.4
7967	0.52	0.47	6209.45	54.76	4.88E-5	4.68E-6	-4.31	0.042	-28.34
8139	0.69	0.55	5630.00	41.38	4.22E-5	4.12E-6	-4.37	0.042	-121.32
8262	0.83	0.66	5257.79	33.71	1.11E-5	1.37E-6	-4.95	0.053	14.24
8411	0.75	0.59	5470.25	37.97	5.62E-5	5.21E-6	-4.25	0.040	-265.71
8435	1.32	1.19	4349.17	21.85	5.04E-6	4.21E-7	-5.3	0.036	-188.51
8536	0.54	0.48	6122.10	52.66	4.32E-5	4.23E-6	-4.36	0.042	-258.86
8689	0.85	0.68	5220.06	32.99	4.36E-5	3.95E-6	-4.36	0.039	-527.04
8725	1.24	1.10	4473.16	22.6	1.38E-6	1.64E-7	-5.86	0.051	-100.78
8923	0.91	0.74	5074.65	30.35	4.04E-5	3.45E-6	-4.39	0.037	-251.3
9054	0.57	0.50	6009.62	50.0	8.71E-5	7.62E-6	-4.06	0.038	-134.49
9140	0.62	0.52	5856.29	46.44	7.22E-5	6.37E-6	-4.14	0.038	-54.68
9146	0.92	0.75	5053.32	29.99	1.46E-5	1.44E-6	-4.84	0.043	2.84
9286	0.81	0.64	5306.12	34.65	4.39E-5	3.86E-6	-4.36	0.038	17.52
9328	0.44	0.40	6524.01	62.52	7.09E-5	6.87E-6	-4.15	0.042	69.86
9465	0.70	0.55	5603.85	40.81	1.66E-4	1.44E-5	-3.78	0.038	-370.41
9475	0.71	0.56	5563.88	39.95	2.27E-5	2.76E-6	-4.64	0.053	-160.23
9852	0.54	0.48	6125.83	52.75	6.01E-5	5.52E-6	-4.22	0.039	-335.09
10390	0.53	0.48	6144.56	53.2	1.2E-5	1.88E-6	-4.92	0.068	-125.17
10863	0.45	0.41	6488.89	61.64	5.97E-5	5.94E-6	-4.22	0.043	3.23
11233	0.71	0.56	5558.24	39.83	1.43E-4	1.19E-5	-3.84	0.036	-408.85
11304	0.81	0.64	5311.03	34.74	4.44E-5	3.89E-6	-4.35	0.038	46.78
11366	0.71	0.56	5578.06	40.25	1.21E-4	1.0E-5	-3.92	0.036	1.21

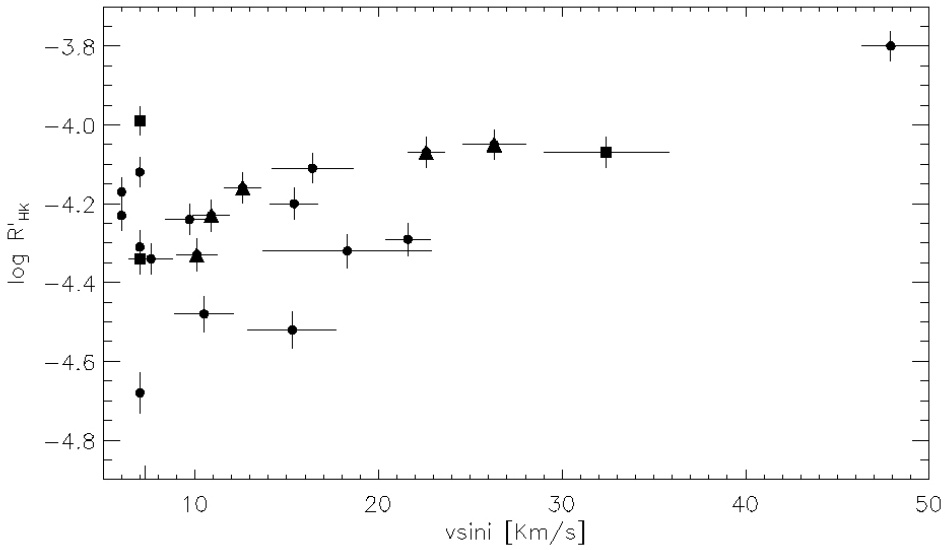

Figure 6.6: CaII H&K emission versus projected rotational velocity v sin i taken from Terndrup et al. (2002). Only names of potentially binaries and non members are plotted. ■ and ▲ are data of likely non-members and binaries, respectively.

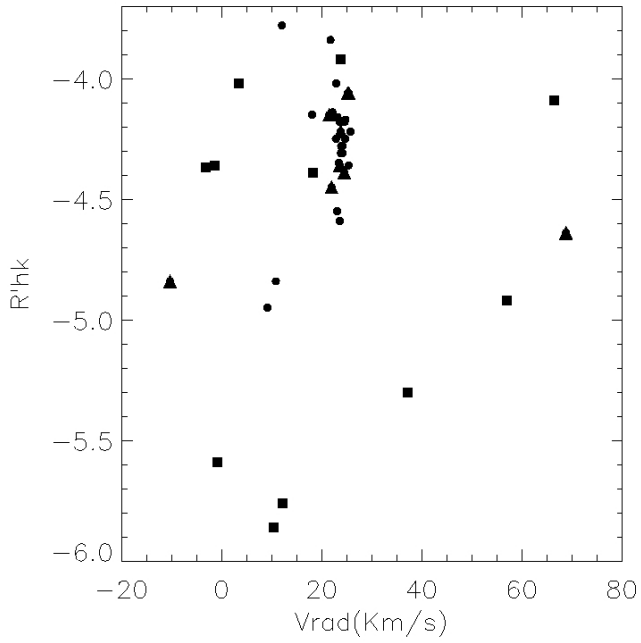

Figure 6.7: CaII H&K emission versus radial velocity defined in section 6.1. Only names of potentially binaries and non members are plotted.■ and ▲ are data of likely non-members and binaries, respectively.

The derived chromospheric index has been compared with the level of coronal activity (Pillitteri et al., 2006). In Figure 6.8 is also plotted the relation of Mamajek & Hillenbrand (2008), from Equation 2.5.The mean value of the $\log R'_{HK}$ derived, seems to overestimate that relation. The reason could be due to different factors. First of all, the data of Pillitteri et al.

(2006) seems to be quite dispersed, as can be seen in Figure 6.9. Secondly, the relation derived by Mamajek & Hillenbrand (2008) is calibrated using chromospheric index derived with the method of Mt.Wilson. Recently, Lubin et al. (2010) measured the relation between star in the Maunder minimum, considering different catalogues of $\log R'_{HK}$ values. They noticed that the measurements of Strassmeier et al. (2000), used in their work, show a value of $\log R'_{HK}$ slightly larger than the other ones. I presume that this could be simply due to the method used to derive the $\log R'_{HK}$. In fact, while Strassmeier et al. (2000) followed the method described in Linsky et al. (1979b), the other authors, cited in Lubin et al. (2010) all used the method of Noyes et al. (1984). Probably the method of Linsky et al. (1979b) underestimate the subtracted photospheric contribution, or conversely, the MW method overestimate it.

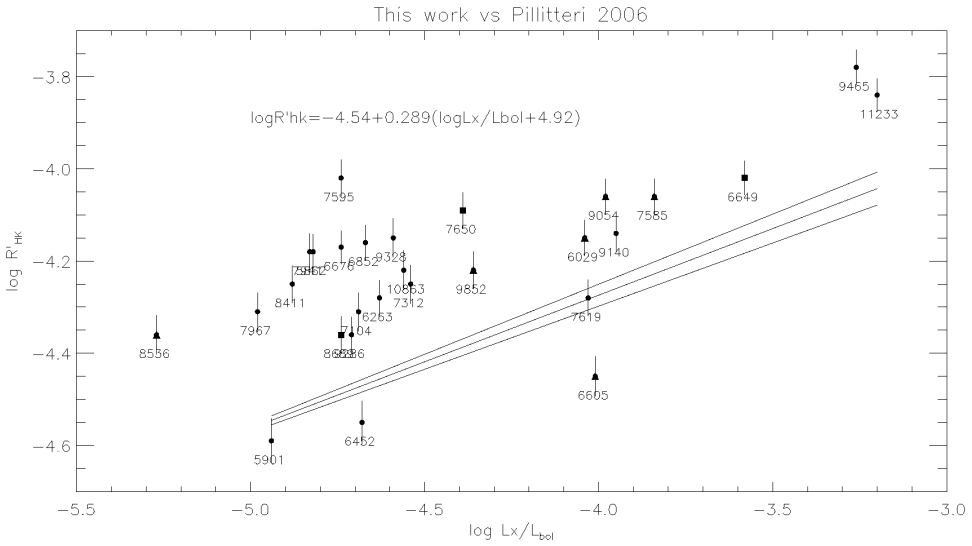

Figure 6.8: Cross correlation between chromospheric and coronal activity. The coronal index are from Pillitteri et al. (2006) ■ and ▲ are data of likely non-members and binaries, respectively.

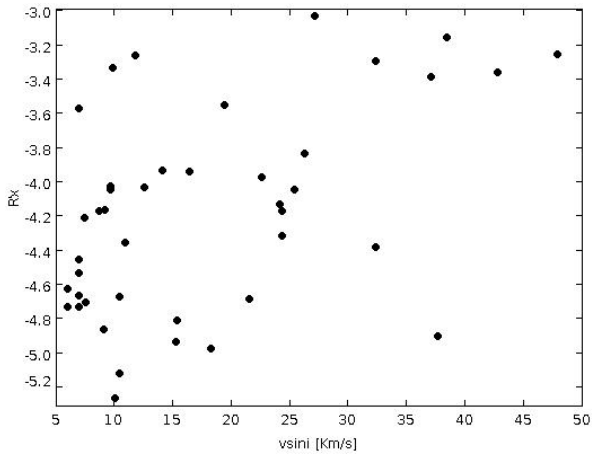

Figure 6.9: Coronal activity versus v sin i. The coronal index are from Pillitteri et al. (2006) while v sin i are from Terndrup et al. (2002). □ and ◊ are data of likely non-members and binaries, respectively.

6.3 Index Calibration

Due to to the presence of overestimation of the chromospheric index, as highlighted in Figure 6.8, I have used some stars' spectra observed by FEROS to derive the $\log R'_{HK}$ with the method of Linsky et al. (1979b) and Noyes et al. (1984). This has been done in order to establish if there is a systematic error in the derivation of the $\log R'_{HK}$ with the method of Linsky et al. (1979b). Using Aladin, I cross-matched the observed stars available with FEROS, with the ones of the catalogue of Duncan et al. (1991), in order to compare the results.

As described in section 2.4.1, the passbands used to estimate the mean flux in the continuum (V and R) are both square and centered at wavelengths of 3891Å and 4001Å respectively. The passbands used to obtain the mean flux in the K and H line cores have triangular profiles with full-width half maximum's (FWHM) of 1.09Å and are centered on the lines themselves at wavelengths of 3933.664Å and 3968.470Å respectively. The activity indicator for FEROS stars has been determined with equation 2.7 (considering $\alpha = 18$) and the reproduced bands are showed in Figure 6.10.

Tinney et al. (2002); Wright et al. (2004) and other authors, that used the Mount Wilson method to determine the R'_{hk} index, have shown that linear calibrations are needed to correct high resolution activity indices onto the Mt Wilson system of measurements of Duncan et al. (1991). I then used the cross-matched stars to do the calibration.

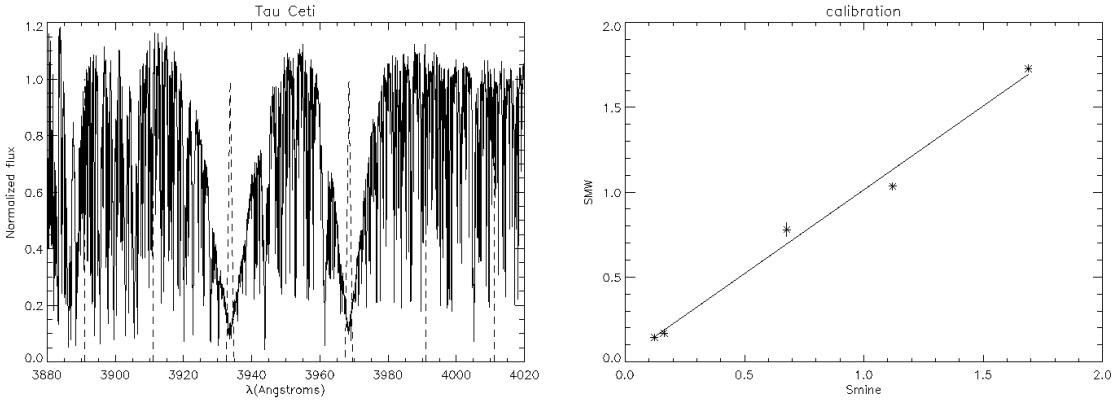

Figure 6.10: Left: Example of one of the FEROS stars used for calibration, with the MW band overplotted. Right: Calibration between the star in which the S index has been measured by Duncan et al. (1991) and mine.

Once that the S index has been calibrated, I converted it in R_{hk} using Equation 2.9 and 2.8, and then I subtracted the photospheric contribute $R'_{hk} = R_{hk} - R_{phot}$ using the formula in the Appendix of Noyes et al. (1984):

$$\log R_{phot} = -4.02 - 1.4(B - V) \tag{6.1}$$

In Table 6.5 are the valued derived for stars observed with FEROS with the ones derived by Duncan et al. (1991). I compared the different values of $\log R'_{HK}$ derived from the S index of Duncan et al. (1991) and by me, using both the method of Linsky et al. (1979b) and MW method. Even if the stars considered are few, the difference obtained with data derived with the MW method and the Linsky method show that the last method seems to give a value for R_{hk} that is higher than the other one. However, a clarification is needed. Usually in all the catalogues in which the CaII H&K lines have been studied, spectra have been normalised not considering the level of continuum. For example, the FEROS spectra show a normalisation, in the region between the H and K lines, that is over the unity. But as explained in Chapter 4, in that region of the spectrum, specially in cooler stars, the level of continuum is very low, due to the presence of a lot of absorption lines. This could be affect the final result.

Moreover, each method subtract in a different way the contribute of the continuum. While in the Linsky's method I consider only a narrow region near the H1,K1 minima, the Mt Wilson's method include in the triangular bandpass a lot of the photospheric contribution, that could be overestimate in the term of correction R_{phot}.

Table 6.5: Stars in which the R'_{hk} index has been measured with the Linsky et al. (1979b)'s method and compared with the same value derived by Duncan et al. (1991).In the first column there is the star's name, B-V magnitude are from Duncan et al. (1991). Effective temperatures were estimated from the relation of Gray (2005), using the B-V. Smine is the S index derived with MW method before the calibration. SMW is the index taken from Duncan et al. (1991). S index is the value obtained after the calibration. Sdiff is the difference between Smine and SMW, while S-SMW is the difference between the index calibrated and SMW. Then there are the $\log R'_{HK}$ derived with the Linsky et al. (1979b)'s method, and the one derived from the conversion of SMW and S. In the last two columns diffRhkMW is the difference between the $\log R'_{HK}$ derived from SMW and the one derived from S, while diffRhkLinsky is the the difference between the $\log R'_{HK}$ derived from SMW and the one derived with the Linsky method.

name	B-V	T_{eff}	Smine	SMW	Sdiff	S	S-SMW	$\log R'_{HK}$			diffRhk	diffRhk
								mine Linsky	MW	mine MW	MW	Linsky
τceti	0.722	5535.85	0.163	0.17	-0.007	0.187	0.017	-4.776 ± 0.131	-4.927 ± 0.011	-4.856 ±0.529	0.071	0.151
GJ281	1.402	4223.81	1.689	1.73	-0.039	1.695	-0.033	-5.269 ± 0.069	-4.718 ± 0.005	-4.727 ±0.189	-0.009	-0.552
EPEri	0.899	5100.6	0.677	0.78	-0.103	0.695	-0.085	-4.259 ± 0.101	-4.278 ± 0.022	-4.333 ±0.302	-0.055	0.018
αBoo	1.157	4610.74	0.122	0.14	-0.022	0.146	0.002	-5.872 ± 0.262	-5.731 ± 0.035	-5.715 ±1.042	0.016	-0.140
Gl393	1.518	4048.45	1.120	1.03	0.086	1.133	0.099	-5.642 ± 0.097	-5.113 ± -	-5.069 ±0.261	0.043	-0.529

6.4 Lithium abundance for NGC2516

The resonance doublet of LiI at 6707.81 Å is an important age diagnostic in late-type stars since it is destroyed by nuclear reactions at the base of the convection zone. It consists of two doublets, one for each of the two isotopes, ^{6}Li and ^{7}Li. For each doublet,the ratio of g_f values of the two components is 2:1, and the stronger ^{6}Li line coincides with the weaker ^{7}Li. Because $^6\mathrm{Li}/^7\mathrm{Li} < 0.1$ in all known cases, it is sufficient to measure only the two components of ^{7}Li even if the doublets are partially resolved (Soderblom et al., 1993b). Often, the blue side of the LiI line is blended with the FeI λ6707.441Å line, either because of rotational broadening ($v \sin i > 8$ Km$\cdot$s^{-1}) or because of inadequate spectroscopic resolution. The wavelength separation between the λ6707.441 Å FeI line and the Li feature is large enough that the two features are not completely resolved even in the best cases of slowly rotating objects (Randich et al., 1997). In these cases, the measured equivalent width (W_λ[LiI + FeI]) can been corrected using the empirical relation of Soderblom et al. (1993a):

$$W_\lambda(6707.441\text{Å}) = 20(B - V) - 3\ \text{mÅ} \tag{6.2}$$

valid for $0.4 \leqslant (B - V) \leqslant 1.4$. According to Soderblom et al. (1993a) this relationship is accurate from 3 to 5 mÅ. Generally, at lower T_{eff}, new lines and molecular bands could appear close to the LiI doublet (Barrado y Navascues & Stauffer, 1996), and also the rotation can contribute to determine with uncertainties the continuum position and the blending with other lines. For the coolest stars, the red side of the lithium line is also blended.

Detecting the Li λ6708 Å feature in young stars is easy, since the W_λ is greater than 100 mÅ, and for this reason the presence of this feature is used as a discriminant for T Tauri stars. While it is difficult to detect in Li-poor stars like the Sun, because is blended with many other lines of comparable strength (Soderblom, 2010).

Ten observations have been made about the NGC2516 open cluster, and I make a mean value of LiI for all the nights, excluding the spectra in which the LiI line can not be easily determined. In Figure 6.11 are plotted some example of our spectra.

EWs of the lithium line at λ6707.876Å have been derived by direct integration and gaussian profile fitting using the IRAF task SPLOT. The major source of error on the measured EWs comes from the quality of our spectra, due to rapid rotation and/or relatively low S/N. The expected uncertainty in the measured lithium equivalent widths has been estimated from the formula of Cayrel de Strobel & Spite (1988):

$$\sigma_{\mathrm{EW_{Li}}} = \frac{1.6}{\mathrm{S/N}}\sqrt{\mathrm{FWHM} \times \delta \mathrm{x}} \tag{6.3}$$

where S/N is the signal to noise ratio, FWHM is the full width of the line at half maximum, and δx the pixel size (0.02nm).

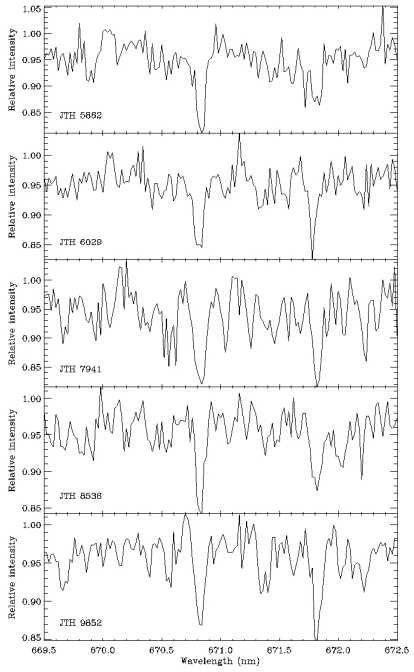

Figure 6.11: Example of some spectra around the λ6707.876Å LiI line.

Given the resolution of the spectra containing the Li-lines (R $\sim$ 8000), the LiIλ6707.8Å line is blended with the nearby FeIλ6707.41Å lines. Therefore, I corrected the total measured equivalent width, EW(LiI+FeI), by subtracting the EW of FeI, by using the empirical relationship given by Soderblom et al. (1993a) (Figure 6.12) and then converting them to log N(Li) using their curve of growth and the NLTE correction of Carlsson et al. (1994).

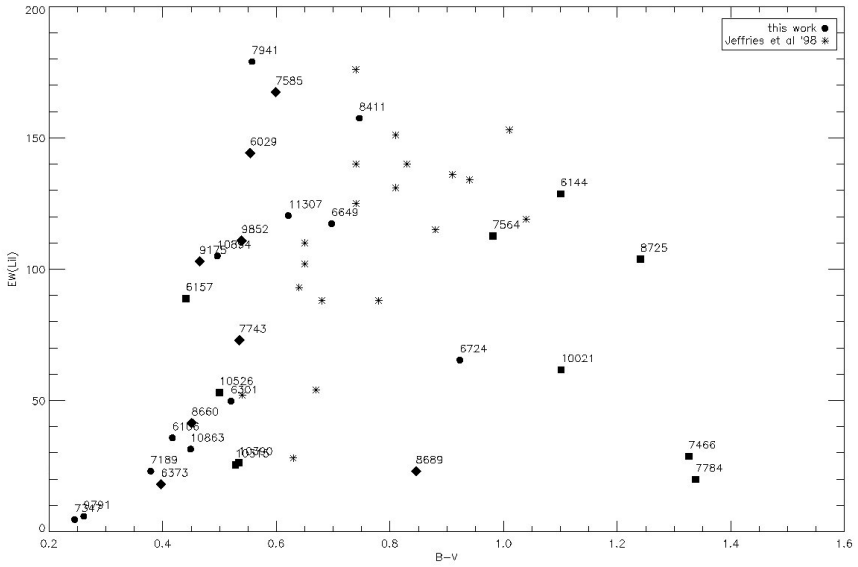

Figure 6.12: EW corrected from the blending versus B-V corrected for the reddening.♦ are probably binaries while ■ are not members. * are data from Jeffries et al. (1998).

From measured EWs, I derived LiI abundance using the curves of growth of Soderblom et al. (1993a) and the effective temperatures derived from corrected B-V colours of Jeffries et al. (2001). Finally, lithium abundances were then corrected for the NLTE effects using the prescriptions of Carlsson et al. (1994). The abundance are given on the usual notation, $\log[N(Li)] = \log[n(Li)/n(H)] + 12$, where n is the number density of atoms and $\log N(H) = 12$.

In Table 6.6 are listed the blended and corrected EW of LiI for NGC2516 cluster members, together with the lithium abundances derived and the S/N.

JTH	EW([LiI + FeI]) (mÅ)	EW(LiI) (mÅ)	eEW(LiI) (mÅ)	logN(LiI)	err-	err+	FWHM	S/N
6029	161.78	144.23	26.21	3.05	0.14	0.14	978	27
6106	53.14	35.72	18.53	2.65	0.33	0.20	121	43
6144	146.78	128.68	23.63	1.50	0.14	0.13	855	28
6157	106.30	88.86	18.62	3.11	0.13	0.12	66	24
6301	67.23	49.71	37.68	2.42	0.65	0.30	63	34
6373	35.44	18.04	18.83	2.34	0.32	0.32	81	77
6649	135.00	117.30	12.57	2.47	0.07	0.07	112	27
6724	83.28	65.36	31.20	1.65	0.33	0.23	64	18
7466	47.06	28.73	29.58	0.27	0.50	0.50	617	19
7564	130.54	112.56	75.37	1.74	0.61	0.38	710	8
7585	185.00	167.40	20.96	2.94	0.10	0.10	105	35
7743	90.45	72.91	34.98	2.62	0.32	0.23	86	33
7941	196.60	179.04	36.07	3.23	0.18	0.19	1230	22
8411	175.23	157.48	40.45	2.48	0.20	0.19	540	13
8660	58.84	41.39	14.90	2.53	0.19	0.15	70	40
8689	40.87	23.02	30.01	1.13	0.41	0.41	46	20
8725	122.02	103.78	6.75	1.15	0.05	0.04	890	100
9175	120.38	102.91	36.68	3.01	0.25	0.20	88	41
9882	33.63	16.57	9.92	2.29	0.42	0.22	100	102
10021	79.73	61.63	42.69	1.04	0.54	0.31	63	19
10315	42.98	25.45	45.27	2.12	0.48	0.48	97	41
10390	43.83	26.30	82.75	2.13	0.72	0.72	83	18
10526	70.51	53.01	12.28	2.65	0.13	0.10	495	41
10863	48.89	31.44	23.75	2.42	0.64	0.25	58	33
10894	122.53	105.03	21.05	3.02	0.13	0.11	1000	34
11307	137.97	120.35	56.34	2.71	0.35	0.27	75	22

Table 6.6: Lithium abundance and EW of stars of NGC2516. In the first column there is the name of the star using the nomenclature of Jeffries et al. (2001). From the second to the fourth there are the EW of the LiI blended to the FeI, then the EW corrected and the errors. From the fifth to the seventh there are the lithium abundance with the upper and lower errors. Finally there are the FWHM and the S/N, used to derive the errors.

The derived lithium abundance supplemented by data from Jeffries et al. (1998) have been compared with theoretical models of Chaboyer et al. (1995); Baraffe et al. (1998) and Siess et al. (2000) (Figure 6.13). I assumed an initial Li abundance of A(Li) = 3.3, similar to that in meteorites and very young T-Tauri stars. Note that the models of Chaboyer et al. (1995) (as

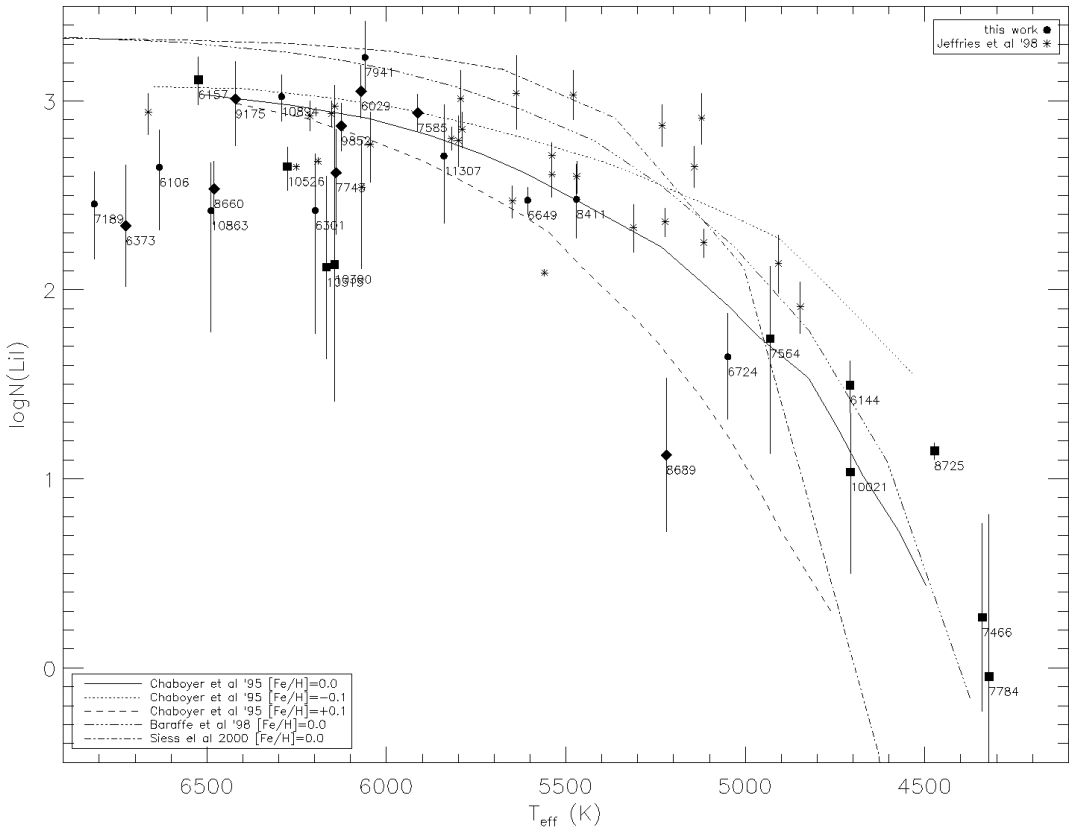

Figure 6.13: Lithium abundance vs. $T_{\rm eff}$. Li abundance from Jeffries et al. (1998). ♦ indicate binaries and ■ not members. Comparison are made with theoretical models at 150 Myr by Chaboyer et al. (1995); Baraffe et al. (1998); Siess et al. (2000). For Baraffe et al. (1998) I used a mixing length parameter of 1.9 pressure scale heights and a solar abundance. For Siess et al. (2000) I choose a model with Z=0.2 and no overshooting. Chaboyer et al. (1995) 's models have been plotted as in Jeffries et al. (1998).

also showed in Jeffries et al. (1998)) and Baraffe et al. (1998) at the age of NGC2516 agree quite well with the data, especially for cooler stars. On the other hand, the model of Siess et al. (2000) shows a deficient depletion for star hotter than 5000 K, and excessive depletion for cooler stars.

It is interesting to note also that some of the stars that have been excluded by the memberships criteria have a lithium age close to that of the cluster. This could be also due to the fact that they have been dereddened using the same E(B-V) of the cluster, and for this reason the $T_{\rm eff}$ calculated could be lower or higher than the ones derived. The hotter stars in the sample show a higher Li depletion, maybe because they are also slow rotators, as pointed out by Jeffries et al. (1998). Future measurements of lithium abundance in stars with $T_{\rm eff} < 5000$K could help us in having a larger and more stringent comparison with the models.

In order to see if there is a relation between the chromospheric activity and the lithium depletion, I reported in Figure 6.14 the $\log R'_{\rm HK}$ vs. $\log N(\rm Li)$. At a first glance, the two

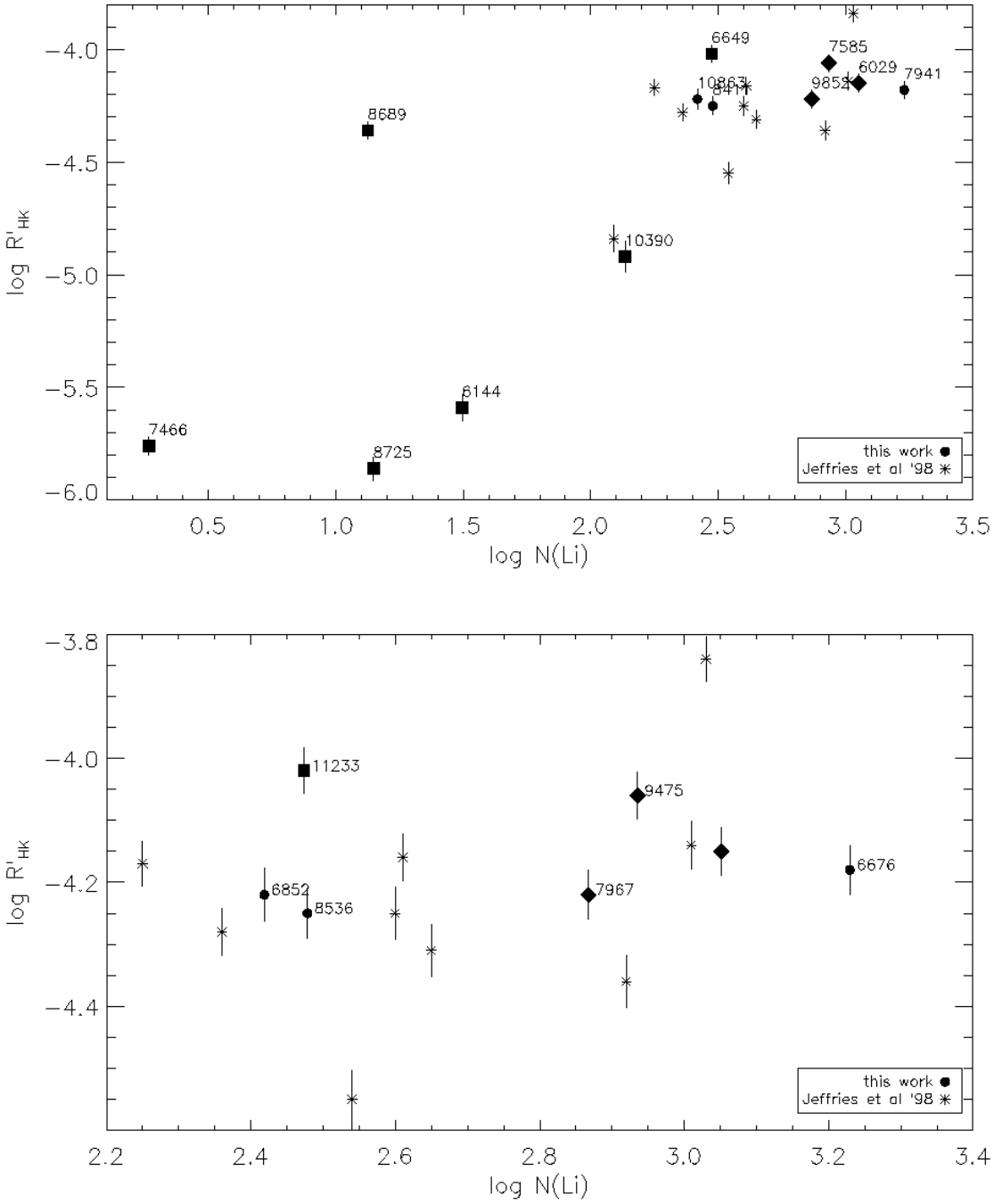

Figure 6.14: CaII H&K emission versus Lithium abundance for the main-sequence stars. ■ and ♦ indicate data for likely non-members and binaries, respectively. The lower panel is a zoom of the upper panel.

quantities seem to show a correlation. However, this may simply derive from the dependence on B − V (or $T_{\rm eff}$) of both $\log R'_{\rm HK}$ and $\log N(\rm Li)$ and therefore not from a genuine dependence of the lithium abundance on stellar magnetic activity. To remove this ambiguity, one would need more measurements than available of both $\log R'_{\rm HK}$ and $\log N(\rm Li)$ on stars of approximately the same B − V. In order to show if there is an evident correlation between

the chromospheric activity index and the lithium abundance, I used the data available for the Pleiades (Figure 6.4) and for NGC2516. As I can see from Figure 6.4, there is not an evident correlation between the two quantities. The pearson coefficient is -0.212329, obtained considering all the 43 points observed (the single B − V intervals are listed in Table 6.4).

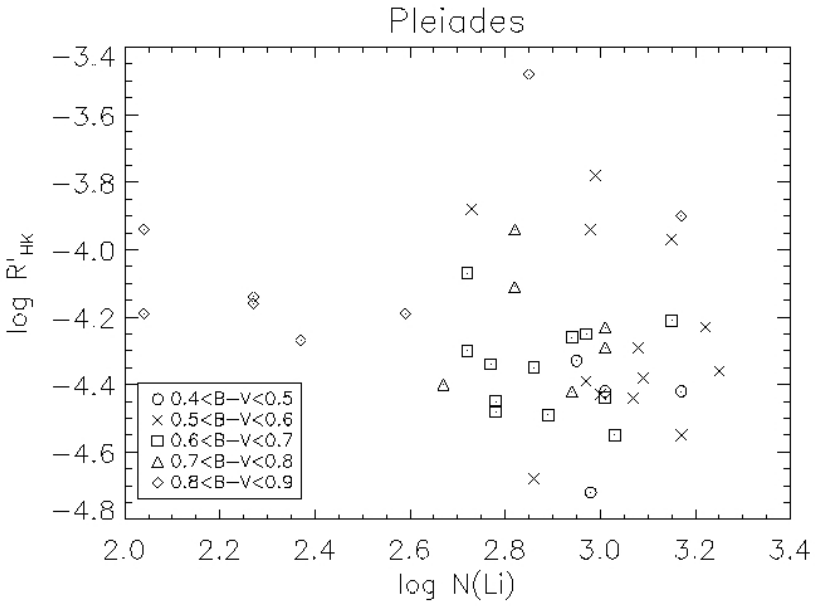

Figure 6.15: CaII H and K emission versus Lithium abundance for the main-sequence stars of the Pleiades.

Colour	Pearson's coefficient r	Number of elements
$0.4 < B - V < 0.5$	0.145	4
$0.5 < B - V < 0.6$	-0.215	13
$0.6 < B - V < 0.7$	-0.104	12
$0.7 < B - V < 0.8$	-0.067	6
$0.8 < B - V < 0.9$	0.533	8

Table 6.7: Pearson coefficient for Pleiades' stars.

6.5 Lithium abundance for NGC3766

In this section have been studied the stars of the young open cluster NGC3766 in order to derive the lithium abundances and give a better estimation of the age. Firstly, I made a colour-magnitude diagram comparing our available photometry with the theoretical models of Baraffe et al. (1998) (with a mixing length parameter of 1.9H_P and solar abundance Z=0.2).

We corrected the V-I colour index using $E(V - I) = 1.615 \cdot E(B - V)$ and I determined the absolute V-band magnitude (M_V), using the observed V-band magnitude (V) of Messina

S. (private communication), correcting it for the reddening (using the distance modulus md = 11.73 ± 0.33 and E(B − V) = 0.20 ± 0.10 of Moitinho et al. (1997)) and assuming no extinction $M_V = V - md - 3.1 \cdot E(B-V)$. As I can see in Figure 6.16 a big scatter is present.

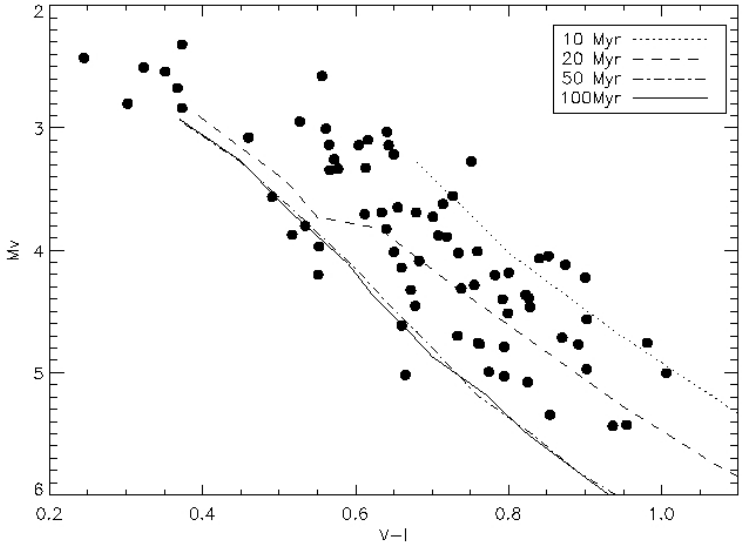

Figure 6.16: Colour-magnitude diagram for the open cluster NGC3766. Models of Baraffe et al. (1998) from 10 to 100 Myr have been overplotted.

The age of the cluster is not yet well defined, and, as said in section 3.2, it varies in the range from 14.5 to 25 Myr. Moreover, the photometry from which the colour-magnitude diagram is derived consist also of field stars, that can modify the real position of the main sequence.

The EW have been derived using the task splot of IRAF, analysing the spectra of different nights and than making an average of the results. In order to correct the blending of the FeI line with the relation 6.2 of Soderblom et al. (1993a), I derived the B-V from the V-I, making a calibration of the two colour indices (Figure 6.17), using the data of Messina et al. (2010) for the three coeval stellar associations Tucana/Horologium, Columba, Carina (∼30Myr), with ages close to NGC3766. In Table 6.5 are listed the blended EW of LiI and the corrected EW for NGC3766 together with the S/N, FWHM and the errors derived from the relation 6.3.

In Figure 6.18 are shown the EW(LiI + FeI) and EW(LiI) versus V-I corrected for the reddening. As can be seen in the figure, the correction of the blending is of approximately of the 20%. The blending correction is to much for stars with low EW, and some stars show a value under the unity. Moreover, this relationship is valid for $0.4 \leqslant (B - V) \leqslant 1.4$, and a source of error could be the derivation of B − V from V − I, since the cluster is in the PMS and I can not use the relationships valid for stars in the MS. In Figure 6.19, instead, are empirically compared the lithium depletion (from the not corrected EW of the 6708Å line) seen in NGC3766 with that in the Pleiades (Soderblom et al., 1993a).

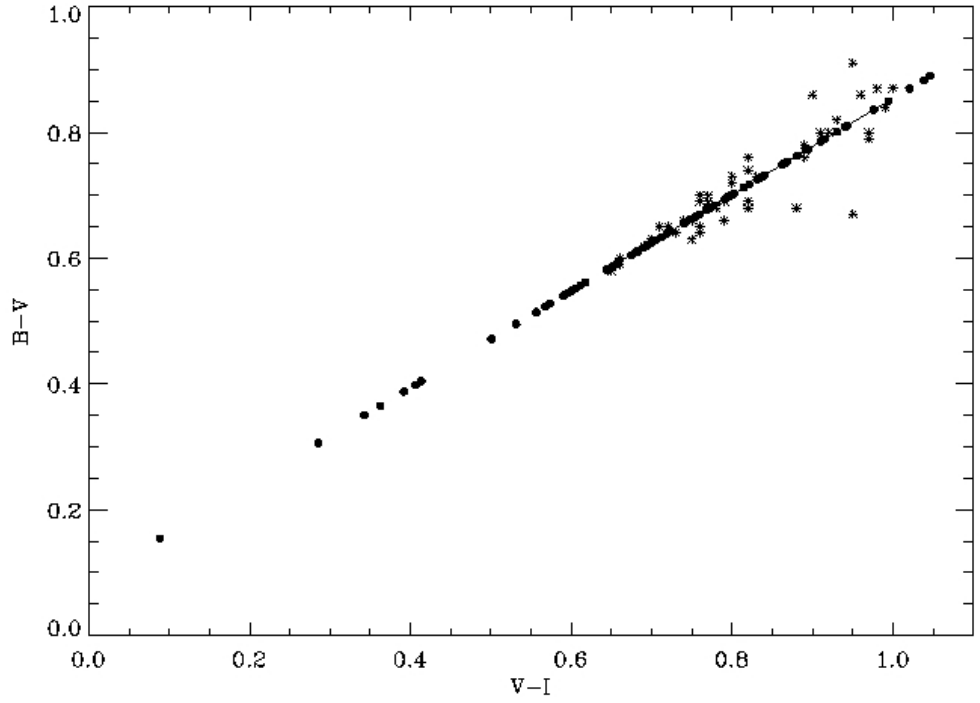

Figure 6.17: Calibration between the V-I and B-V colour indices. The * are the stars used for the calibration, from Messina et al. (2010), while • are the B-V derived from the V-I of Messina,S (private communication).

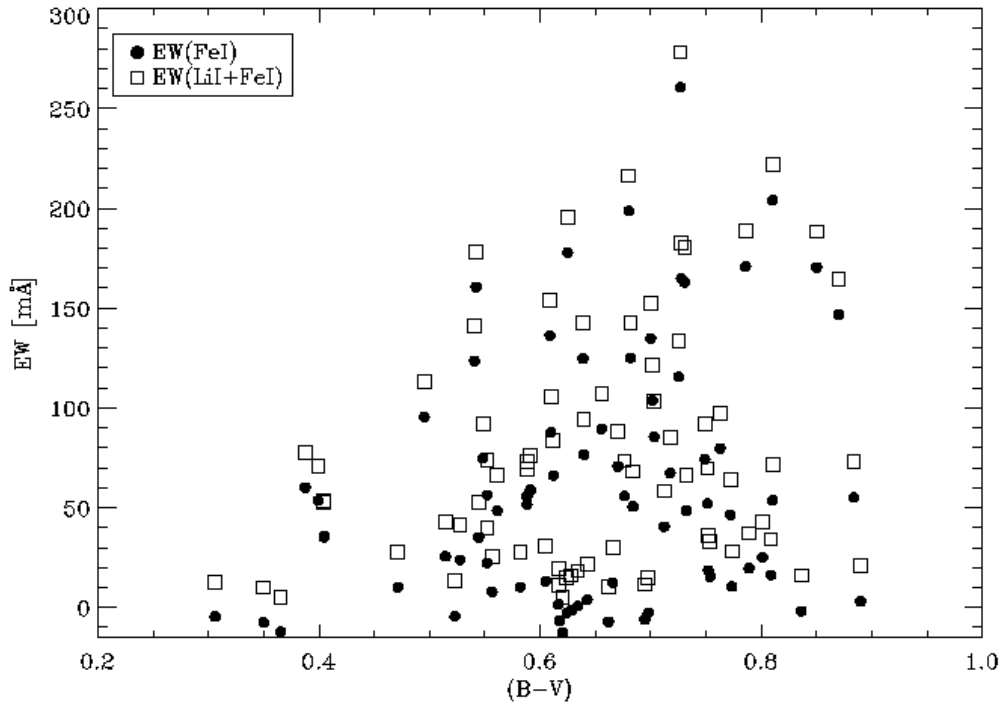

Figure 6.18: EW of both the lithium, blended(□) and deblended (•), versus B−V corrected for the reddening. The errors have not been plotted in order to facility the readability of the plot.

N	S/N	FWHM [mÅ]	EW(LiI+FeI) [mÅ]	e(EW) [mÅ]	N	S/N	FWHM [mÅ]	EW(LiI+FeI) [mÅ]	e(EW) [mÅ]
12	125.33	545.6	13.14	4.22	388	75.39	1671.5	105.35	12.27
17	38.31	320.4	28.18	10.57	399	46.85	1166.0	94.27	16.49
20	78.40	802.3	21.45	8.17	422	101.92	1409.0	52.58	8.33
23	117.21	349.6	9.91	3.61	484	89.47	1142.0	70.92	8.55
29	89.54	425.9	19.20	5.22	524	43.21	926.9	37.26	15.94
32	54.60	972.8	188.28	12.90	527	62.26	1350.5	76.37	13.35
57	40.52	1041.0	153.85	18.02	535	75.77	1178.5	73.93	10.25
61	48.14	876.3	66.01	13.91	546	49.01	919.3	107.07	13.99
62	27.97	837.6	42.86	23.41	551	13.59	1000.3	121.45	52.66
65	24.41	1240.7	278.35	32.65	584	39.42	1066.0	92.09	18.74
66	71.59	877.3	25.42	9.362	601	39.70	1190.0	216.27	19.66
77	47.65	2135.0	152.5	21.94	602	39.71	468.9	10.91	12.34
78	71.72	491.6	30.69	6.99	614	68.94	923.6	27.63	9.98
79	43.55	611.7	41.47	12.85	618	30.12	1291.0	77.51	26.99
80	54.02	1318.0	73.43	15.21	622	42.56	532.7	20.78	12.27
89	41.07	953.8	133.27	17.01	636	30.05	602.0	34.16	18.48
90	36.96	1180.2	182.63	21.03	645	35.40	796.9	58.28	18.04
95	86.84	1571.9	39.87	10.33	657	54.89	376.4	10.49	7.99
109	35.24	1027.3	188.60	20.58	659	53.74	482.0	15.00	9.24
126	98.15	1256.0	27.85	8.170	669	49.01	1406.8	142.34	17.31
129	57.23	1107.0	103.13	13.15	674	33.27	392.9	15.00	13.48
140	48.74	952.3	71.44	14.33	676	104.66	341.7	7.69	3.99
144	43.90	1385.9	142.70	19.18	681	28.07	709.2	69.68	21.47
145	74.02	1616.5	83.81	12.29	703	54.43	1026.7	88.47	13.32
148	34.78	1203.7	221.83	22.57	712	11.71	444.7	30.14	40.75
161	66.98	1330.9	92.17	12.32	716	34.89	1666.3	195.43	26.47
164	27.39	954.1	72.96	25.52	723	72.22	1143.1	53.33	10.59
188	55.42	1179.1	141.23	14.02	725	19.63	653.3	85.07	29.46
192	88.86	528.2	11.61	5.85	728	69.70	855.0	43.01	9.49
196	39.29	957.9	97.52	17.82	758	117.47	731.3	12.68	5.21
198	68.22	1399.0	69.11	12.41	770	139.20	402.1	5.207	3.26
205	38.73	1112.3	66.30	19.49	802	49.99	944.9	68.15	13.91
271	33.76	910.02	164.70	20.22	826	44.83	458.0	16.00	10.80
299	55.18	1074.3	73.21	13.44	843	60.51	490.4	18.27	8.28
308	56.85	1375.0	113.00	14.76	855	54.20	1157.3	178.17	14.20
315	58.70	813.0	36.27	10.99	858	44.14	609.8	33.31	12.66
354	55.98	747.7	64.17	11.05	871	5.99	278.2	16.08	63.01
362	42.34	1125.6	180.60	17.93	883	73.14	318.4	5.07	5.52
373	86.82	1507.5	52.75	10.12					

Table 6.8: Equivalent widths for the young open cluster NGC3766. In the first column are listed the stars with the numbering system taken from the photometry of Messina, S. (private comunication). In the second column there is the S/N, in the third the FWHM in mÅ in the fourth there is the EW of the lithium line blended with the FeI. In the last columns are the derived error.

Contrary to what I expected, stars in NGC3766 show a Li depletion close to the one of the Pleiades and if I were to estimate the age of NGC3766 based on the Li-depletion seen in

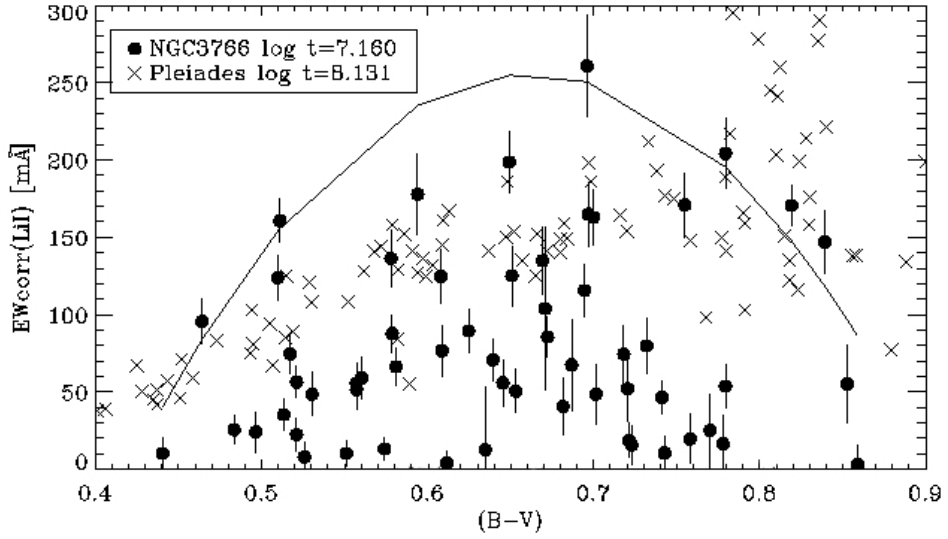

Figure 6.19: Corrected EW versus B − V (corrected for the E(B − V) = 0.2). Our data have been compared to the Pleiades clusters. The ages in the legend are from WEBDA. The curve is obtained considering a polynomial fit of order 2 of the upper values of the EW found for NGC3766.

Figure 6.19 I would conclude it had an age of >100Myr.

In order to measure the lithium abundances I need to derive the effective temperature, but, unfortunately, its determination for PMS stars is a problematic task (King, 1998). The observational quantities used to infer T_{eff} have larger uncertainties than those for MS stars, because of reddening, extinction, and possible contribution from non photospheric emission (Soderblom et al., 1999). Effective temperatures were obtained from the photometric data available, using the relationship found by Randich et al. (1997) for the young open cluster IC2602 of 30Myr:

$$T_{eff} = 9900 - 8598(V - I_C)_0 + 4246(V - I_C)_0^2 - 755(V - I_C)_0^3$$

We have done the conversion of the EW to log N(Li) using the empirical relationship given by Soderblom et al. (1993a) and then correcting the NLTE correction of Carlsson et al. (1994). In Table 6.9 and C.1 the lithium abundance obtained for different corrections of E(B-V) are listed.

Table 6.9: Lithium abundance derived for the stars of the young open cluster NGC3766, assuming a reddening of E(B-V)=0.20(Moitinho et al., 1997). In the first column there is the name of the stars, following the numbering system of Messina,S. (private communication), in the other three columns there are the lithium abundance and the lower and upper errors, assuming no correction for the FeI blending. In the last three columns there are the equivalent width corrected for the blending and the lithium abundance derived, together with the lower and upper errors.

E(B-V)=0.20							
	without correction			with correction			
name	logNLiI	-	+	EW	logNLiI	-	+
12	2.02	0.18	0.13	-4.35	-	-	-
17	1.22	0.23	0.15	10.44	0.77	0.31	0.31
20	1.85	0.23	0.15	3.84	1.07	0.51	0.51
23	2.06	0.20	0.14	-7.40	-	-	-
29	1.79	0.15	0.11	1.61	0.72	0.60	0.60
32	2.12	0.06	0.06	170.46	2.04	0.06	0.06
57	2.87	0.08	0.09	136.27	2.79	0.09	0.08
61	2.56	0.12	0.10	48.48	2.41	0.15	0.13
62	1.42	0.38	0.23	25.09	1.17	0.93	0.31
65	3.05	0.16	0.16	260.65	2.97	0.16	0.16
66	2.12	0.21	0.14	7.89	1.58	0.35	0.35
77	2.45	0.11	0.09	134.83	2.37	0.12	0.11
78	2.02	0.12	0.09	13.12	1.62	0.34	0.20
79	2.53	0.15	0.13	23.97	2.30	0.35	0.18
80	2.19	0.12	0.11	55.78	2.05	0.15	0.13
89	2.36	0.09	0.08	115.58	2.27	0.09	0.09
90	2.59	0.09	0.10	164.93	2.51	0.10	0.10
95	2.52	0.12	0.11	22.349	2.26	0.29	0.17
109	2.37	0.10	0.10	170.84	2.29	0.10	0.10
126	2.16	0.16	0.11	10.30	1.70	0.70	0.27
129	2.19	0.08	0.07	85.46	2.09	0.09	0.08
140	1.69	0.12	0.11	53.66	1.54	0.15	0.12
144	2.61	0.10	0.10	125.05	2.51	0.11	0.10
145	2.50	0.08	0.07	66.22	2.37	0.10	0.09
148	2.54	0.12	0.12	204.05	2.45	0.11	0.12
161	2.94	0.08	0.07	74.65	2.83	0.09	0.08
164	1.48	0.22	0.17	55.11	1.33	0.30	0.21
188	3.21	0.07	0.07	123.72	3.12	0.08	0.07
192	1.31	0.31	0.19	-6.05	-	-	-
196	1.88	0.12	0.11	79.79	1.76	0.14	0.12
198	2.59	0.10	0.09	51.55	2.44	0.13	0.11
205	1.95	0.18	0.14	48.60	1.79	0.24	0.18
271	2.01	0.10	0.10	146.86	1.92	0.10	0.10
299	2.62	0.10	0.09	55.65	2.48	0.14	0.11
308	3.26	0.09	0.08	95.53	3.16	0.10	0.09
315	1.64	0.17	0.13	18.55	1.33	0.42	0.22
354	1.63	0.10	0.09	46.42	1.46	0.13	0.11
362	2.58	0.08	0.08	162.90	2.50	0.09	0.08
373	2.65	0.10	0.08	35.24	2.46	0.14	0.11
388	2.63	0.07	0.06	87.77	2.52	0.08	0.07
399	2.56	0.10	0.09	76.66	2.45	0.13	0.10

Table 6.9: (continued)

E(B-V)=0.20							
	without correction			with correction			
name	logNLiI	-	+	EW	logNLiI	-	+
422	2.83	0.09	0.08	35.21	2.64	0.12	0.09
484	2.99	0.07	0.07	53.55	2.84	0.09	0.08
524	1.36	0.27	0.18	19.50	1.04	0.66	0.29
527	2.64	0.11	0.09	58.81	2.50	0.13	0.11
535	2.82	0.08	0.07	56.41	2.68	0.10	0.08
546	2.41	0.08	0.08	89.44	2.31	0.10	0.08
551	2.29	0.33	0.25	103.78	2.20	0.39	0.27
584	2.13	0.13	0.18	74.37	2.01	0.15	0.13
601	2.97	0.10	0.10	198.62	2.88	0.09	0.10
602	1.53	0.35	0.35	-6.68	-	-	-
614	2.54	0.21	0.13	10.19	2.07	1.72	0.31
618	3.04	0.23	0.19	60.15	2.90	0.28	0.21
622	0.86	0.38	0.21	2.92	0.18	0.54	0.54
636	1.32	0.37	0.21	16.38	0.96	0.36	0.36
645	1.88	0.19	0.14	40.60	1.70	0.27	0.19
657	1.26	0.59	0.26	-7.14	-	-	-
659	1.43	0.43	0.23	-2.67	-	-	-
669	2.82	0.09	0.08	124.73	2.73	0.09	0.09
674	1.68	0.98	0.30	-2.59	-	-	-
676	1.94	0.32	0.19	-9.44	-	-	-
681	1.98	0.19	0.15	51.96	1.82	0.26	0.18
703	2.30	0.09	0.08	70.83	2.17	0.11	0.10
712	1.76	0.41	0.41	12.50	1.34	0.68	0.68
716	3.06	0.12	0.12	177.84	2.98	0.12	0.12
723	2.84	0.11	0.09	35.96	2.65	0.15	0.12
725	2.09	0.23	0.17	67.38	1.96	0.29	0.20
728	2.55	0.11	0.10	25.53	2.33	0.22	0.13
758	2.17	0.24	0.16	-4.59	-	-	-
770	1.77	0.43	0.21	-12.13	-	-	-
802	2.15	0.12	0.10	50.50	1.99	0.14	0.13
826	1.71	0.51	0.24	-1.60	-	-	-
843	1.77	0.28	0.18	0.67	0.44	1.01	1.01
855	3.39	0.06	0.07	160.66	3.31	0.07	0.07
858	1.60	0.22	0.15	15.59	1.24	0.71	0.28
871	0.75	0.78	0.78	-1.72	-	-	-
883	1.19	0.33	0.33	-12.52	-	-	-

In order to make an estimate of the age I plotted in Figure 6.20, three different set of data (each of E(B-V)=[0.175, 0.2, 0.22]), considering the models of Baraffe et al. (1998) from 30 My to 100Myr (assuming an initial Li abundance of A(Li) = 3.3, a solar metallicity and a mixing length parameter lmix = $1.9H_P$). First of all, we can observe a great dispersion of the data, this could be due to the presence of not members, since the membership of the cluster has not yet obtained. As we can easily see, the models do not fit completely with the data,

neither considering a low reddening correction, nor with a higher correction.

Since there were not available models of Baraffe et al. (1998) for stars of higher metallicity than the solar one, I decided to compare our data (using the data with $E(B-V) = 0.2$) with the Siess et al. (2000)'s models, obtained using their web tool[2], using Z=[0.1,0.2,0.3] and ages from 20Myr to 60Myr (Figure 6.21). In Figure 6.21 we can see that models with ages between 40 and 60Myr and $Z = 0.3$ agree better with the data. However, since I do not know well the metallicity and the age of the cluster I can only suppose these assumptions.

A similar case has been observed by Jeffries et al. (2009), for the young open cluster IC4665, which age was estimated to be close to 30Myr. In that case, they compared their results with open cluster of similar age, finding that an empirical age estimate based on Li depletion among the late-type stars of IC 4665 would give an age older than 100 Myr, in disagreement with ages determined with other methods. For these reasons, they suppose that the causes of this trend are possibly the metallicity and/or the slow rotation of the stars considered. The cause of this behaviour should be carefully taken under investigation.

Therefore I can say that determine the lithium abundance of this cluster is quite difficult at the present, since the source of errors are various and of different nature. First of all, the curve of growth of Soderblom et al. (1993a), obtained for the Pleiades and universally used by different authors also for PMS clusters, could not be the right choice. Furthermore, the determination of the effective temperatures is quite difficult and imprecise for PMS stars, while the FeI blending correction has been obtained from B-V, empirically determined by calibration. These assumptions, with the uncertain reddening and metallicity, and a not yet known membership, do not permit a precise estimation of the abundance of lithium.

[2]http://www-astro.ulb.ac.be/ siess/server/iso.html

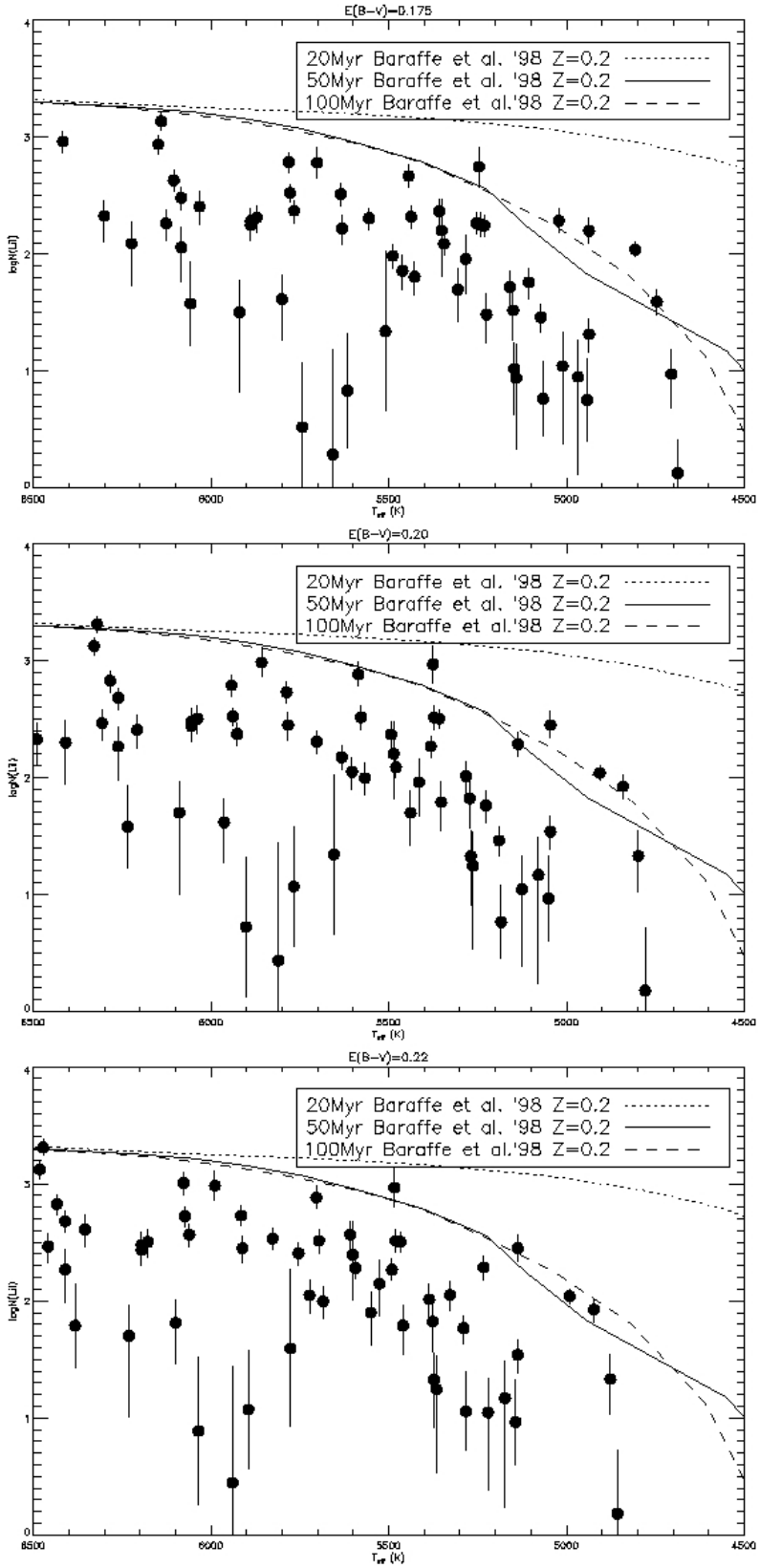

Figure 6.20: Stars of NGC3766 for which I determined the lithium abundance, and compared with the theoretical models of Baraffe et al. (1998) from 30 My to 100Myr. In the upper panel there are the data obtained using a $E(B-V) = 0.175$, in the middle there are the ones obtained with $E(B-V) = 0.20$, and in the lower panel the ones with $E(B-V) = 0.22$.

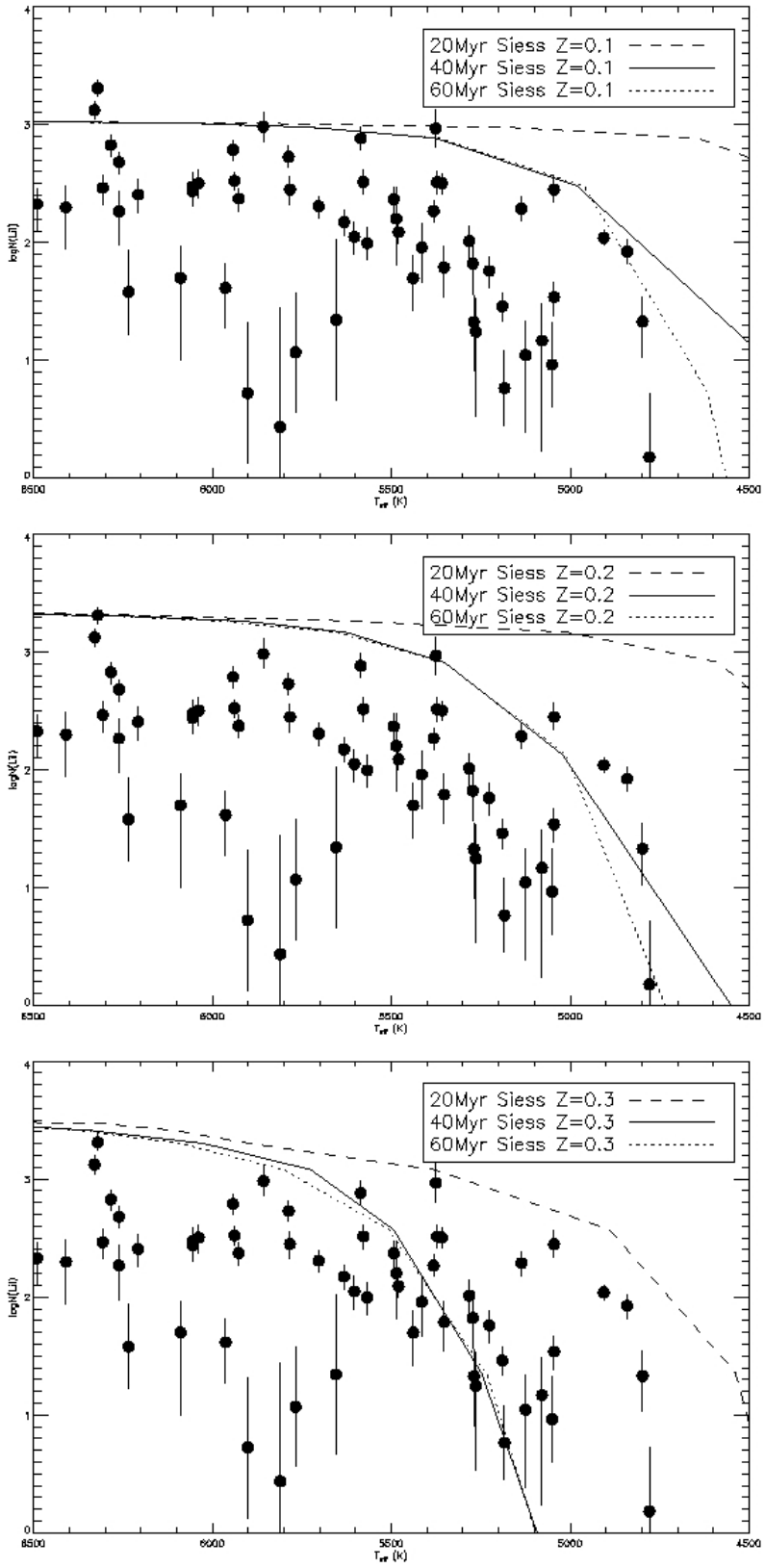

Figure 6.21: Stars of NGC3766 for which I determined the lithium abundance considering a reddening of $E(B-V) = 0.22$, and compared with the theoretical models of Siess et al. (2000), using Z=[0.1,0.2,0.3] and ages from 20Myr, 40Myr and 60Myr.

Chapter 7

Conclusions

Open clusters' studies are fundamental for a better understanding of the stellar evolution. Early stages of solar-like stars evolution, in particular, are still poorly understood. Several methods for determining the age of young clusters are used and for each of them there are different validity and limitation issues to be considered. This thesis focuses on their study, concentrating on the analysis of chromospheric activity and lithium abundance of the open clusters NGC2516 and NGC3766, in order to infer more information about their age, or to better understand what are the problems and difficulties connected to the study of the CaII H and K band.

The first survey monitored the stars of NGC2516, using ESO Archive data, considering star spectra in the range of the CaII H and K ($3854-4049$Å) and the LiI range ($6438-7184$Å). I tried to determine the effective temperatures and astrophysical parameters in the continuous range from 3990 to 4040 Å . Since this range is overcrowed by the presence of a lot of metal lines that create a blending in most of them, it is quite difficult find suitable lines which the equivalent width variation is greater enough to measure a variation in temperature or gravity. The differences between the temperature determined from the photometry and with this method are greater than 200K (Figure 5.3). Indeed, the analysis of this region of the spectrum for determining fundamental stellar properties, such as the temperature, does not give a precise estimation and, furthermore, is quite time consuming due to the difficulties in the search of suitable lines. For this reason I think that the use of this range, to made a determination of the stellar parameters, is not a good choice and it is better to consider a different one. Moreover, the presence of all these metal lines pull down the continuum, and this make the normalisation of the spectra in this range a great problem.

Radial velocities, that extend the survey of Terndrup et al. (2002), agree quite well with their data, and allow to determine a better membership for the stars of this cluster. Most of the star studied in this survey are surely considered as member of the cluster, except for some with ambiguous V_{rad}, that could be assumed as binaries or not members.

As explained in Chapter 2, the determination of the chromospheric indices R'_{HK} is obtained with different methods, each of them with different advantage and limitation. In our case, for the open cluster NGC2516, I choose to derive them using the method developed by Linsky et al. (1979b), as exposed in section 2.4.2. Chromospheric indices R'_{HK} show a dispersion if correlated with $B-V$. This effect seems to vary with the age, as underlined by Mamajek & Hillenbrand (2008) and is not still well determined. The estimation of the cluster's age using the mean value of R'_{HK} gives 140Myr. The values derived could be overestimated, as observed by the comparison with the coronal activity index in Figure 6.8. However, since the relation between these two quantities, derived by Mamajek & Hillenbrand (2008), has been calibrated using only stars which R'_{HK} have been measured using the Mt. Wilson method, it is possible that this discrepancy could be due to different methods used to derive the chromospheric activity indices. Despite that, this is the first survey of this cluster done in the CaII H and K band, and only new measurements of the R'_{HK} index, using the same set of stars and using the two different technique, will permit to understand if the Linsky et al. (1979b) method overestimates the activity index.

I have enlarged the sample of stars for which the lithium of NGC2516 have been measured. For them I have observed the same trend found by Jeffries et al. (1998), essentially confirming their results. The stars of the survey fit well with models with [Fe/H] = 0 and [Fe/H] = −0.1 assuming an age of 150Myr. Some stars (the hotter ones, see Figure 6.13) in the sample show a higher Li depletion. This could be due to the fact that could be slow rotators, as pointed out by Jeffries et al. (1998). This effect has not been confirmed since I do not know neither the rotation period nor the $v \sin i$ for these stars. Interestingly, some of the stars that have been excluded by the memberships criteria have a lithium age close to that of the cluster. I presume that this is due to the fact that they have been dereddened using the same $E(B-V)$ of the cluster, and for this reason the T_{eff} calculated could be lower or higher than the ones derived. For this reason future measurements of lithium abundance in stars with $T_{eff} < 5000$K could help us in having a larger and more stringent comparison with the models.

I finally cross-correlated the R'_{HK} with the logN(LiI), in order to find a connection between these age indicators. Their correlation is not well defined, and could be only due to their dependence to the $B-V$. This is another aspect should be better investigated in the future, if a great number of data with both measurements are available.

Part of the work done on NGC2516, including the chromospheric activity index derivation, and the lithium abundance measurements, has been presented at the JENAM 2010-SYMPOSIUM 5: "Star Clusters in the Era of Large Surveys", held in Lisbon in September

2010 (Messina et al., 2010a).

The second FLAMES survey monitored the stars of the NGC3766 cluster using observation obtained in the LiI range. I interestingly observe that if I compare the EWs obtained for this cluster with the ones of an older cluster such as the Pleiades, I would attribute an age close to ∼100Myr (Figure 6.19 and 6.20). Furthermore, I have determined the lithium depletion of this cluster, using different values of reddening, since the right value is still uncertain. I can presume that effect could be due to the presence of an high metallicity, since the models showing a better comparison with the data are the ones of Siess et al. (2000) with Z=0.3. Unfortunately, the uncertainty about the reddening and the age of the cluster do not permit to estimate well how much the metallicity can contribute to this high depletion. Moreover, also the determination of the T_{eff} is quite imprecise, since in the PMS the calibration of this parameter with the colour index is more uncertain than in the main sequence (King, 1998). The knowledge of metallicity and the reddening will permit a more precise determination of the temperature and consequently of the lithium abundance and the age.

The research plan for this cluster in the next future would be surely focalized on the study of the membership. This could be obtained analysing the radial velocities, that would provide a good tool for the discrimination of not members. Moreover, the accurate determinations of the rotational velocities or of the rotation periods, for both the clusters NGC2516 and NGC3766 would clearly be invaluable in understanding if the reason of high lithium depletion is connected to the rotation. Other interesting development in the study of this cluster could be the analysis of H_α emission (in the same spectral region of the lithium line) that will give new information about the activity level in this young open cluster. A photometric survey of cool stars in the UBV band, with a determination of the reddening based also on cooler stars, could be useful for improving our knowledge about NGC3766. Finally, the study of the metallicity will give a more stringent constraint to the trend of lithium abundance.

Ringraziamenti

"Metti il piede in fallo e cadi sette volte, otto rialzati e risorgi." Hagakure (1, 128)

Questo dottorato é stato senza ombra di dubbio il periodo piú difficile del mio percorso di studi e di questa fase della mia vita, in quanto molto di ció in cui credevo é stato rimesso completamente in discussione. Diverse persone si sono avvicendate in questo delicato periodo, con ruoli diversi e contribuendo in maniera piú o meno diretta alla realizzazione di questa tesi.

L'osservatorio astrofisico di Catania é sicuramente un luogo bellissimo in cui lavorare, da cui poter osservare sia il mare che l'Etna, riparato dal caos della cittadella. Tutto ció, insieme alle persone che dentro ci lavorano e ti tengono compagnia, contribuisce senz'altro a rendere migliore la propria giornata lavorativa. Detto questo vorrei dunque ringraziare coloro che hanno contribuito alla realizzazione di questa tesi, con consigli o semplicemente una parola di conforto al momento giusto.

Vorrei ringraziare il mio tutor, il professore Alessandro Lanzafame, per avermi dato la mia piú grande lezione di vita, ossia avermi insegnato quanto sia importante, soprattutto nel campo della ricerca, farcela con le proprie forze. É stata dura, ma se sono qui a poter scrivere i ringraziamenti per questa tesi é anche merito suo. Vorrei anche ringraziare la dottoressa Innocenza Busá per il suo prezioso aiuto in alcuni momenti "critici", e il dottor Sergio Messina, per avermi gentilmente fornito i dati fotometrici dell'ammasso NGC3766. Ringrazio ancora tutti i colleghi, vecchi e nuovi, i dottorandi, i postdoc e chi piú ne ha ne metta, che hanno allietato le mie giornate e i miei momenti di pausa e non solo.

Ringrazio la mia famiglia, che mi ha sempre assecondato in questo mio percorso, pur sapendo quali erano le difficoltá da affrontare e le conseguenze per il futuro, sopportando con infinita pazienza soprattutto quest'ultimo periodo di tesi.

Un grazie va anche a tutti gli amici del gruppo scout CNGEI di Giarre e dell'associazione astrofili ionico-etnei, che nonostante mi abbiano sempre vista puntualmente mancare a molte delle attivitá organizzate, specie nell'ultimo periodo, mi hano sempre sostenuta e incoraggiata.

Per ultimi, ma non in ordine di importanza, vorrei ringraziare due persone molto speciali,

senza le quali sono sicura non sarei arrivata da nessuna parte. Gabriele è stato finora il miglior amico che avessi mai avuto. Anche se distante è sempre riuscito ad aiutarmi nei momenti di maggiore sconforto e difficoltá, avendo sempre la parola giusta per ogni occasione.

Infine Alessio, che ringrazio per l'infinita pazienza con cui sopporta i miei continui momenti di scoraggiamento, e perché cerca di rendermi ogni giorno una persona piú forte, indipendente e ottimista (e vi assicuro che non è facile). I motivi per cui dovrei ringraziarlo sarebbero praticamente infiniti, e senza il suo prezioso appoggio, il suo saperlo sempre vicino anche quando ci separa la distanza o quando fa "finta" di non esserci, non sarei di sicuro riuscita a raggiungere questo traguardo. È a lui, insieme alla mia famiglia e a tutti quelli che mi vogliono bene e continuano a credere in me, che dedico questa tesi.

Appendix A

Radial Velocities

In Figure A.1 is plotted the range from 4030-4037Å, for the stars of the NGC2516 cluster to which we derived the radial velocities (section 6.1) and we applied the radial velocities correction.

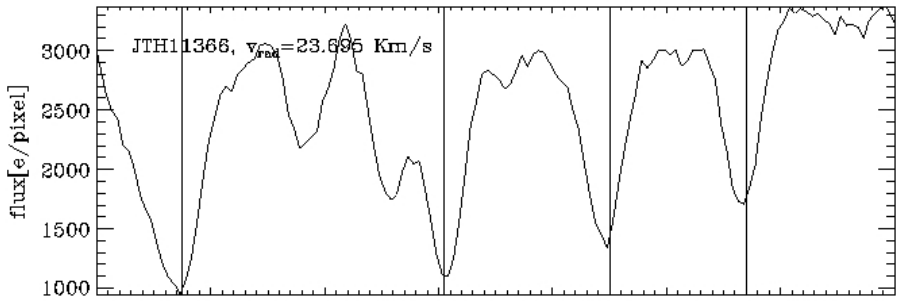

(a)

Figure A.1: Radial velocities correction for star spectra of NGC2516. The lines at 4030.75,4033.05,4034.5 and 4035.7 have been emphasized with a line, in order to show the correct position of the spectrum. The V_{rad} in the legend refers to the correction carried out.

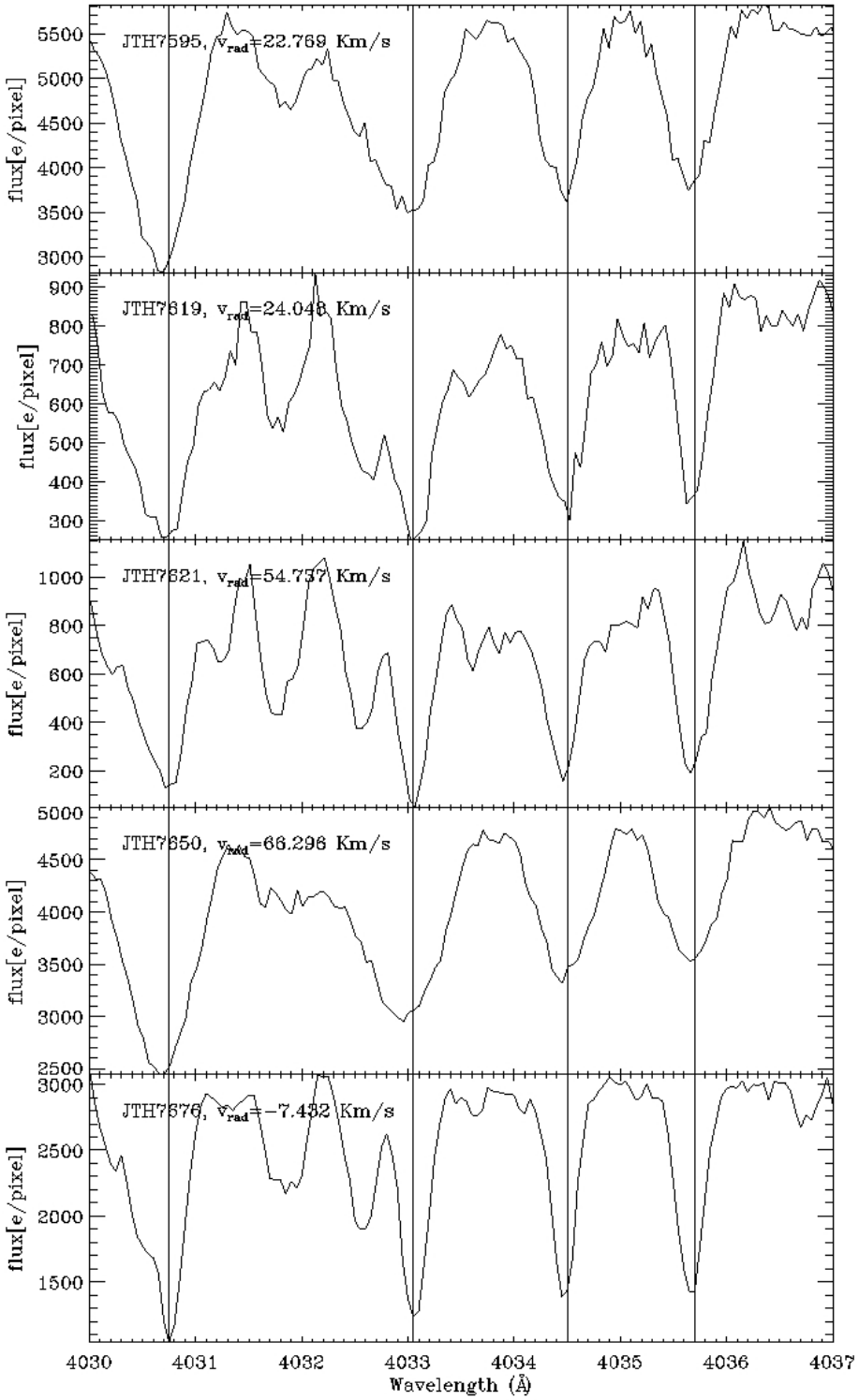

(b)

Figure A.1: continue

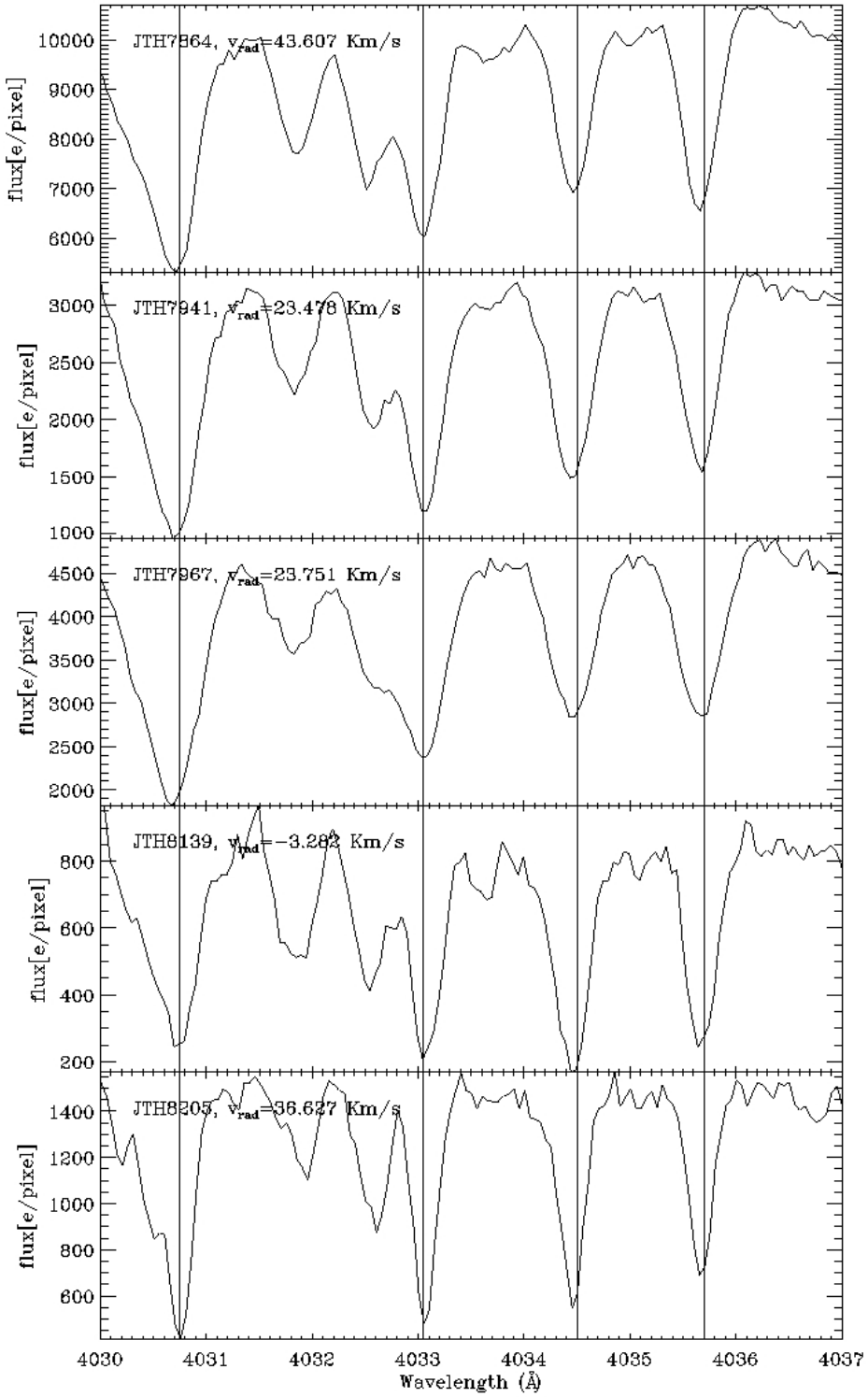

(c)

Figure A.1: continue

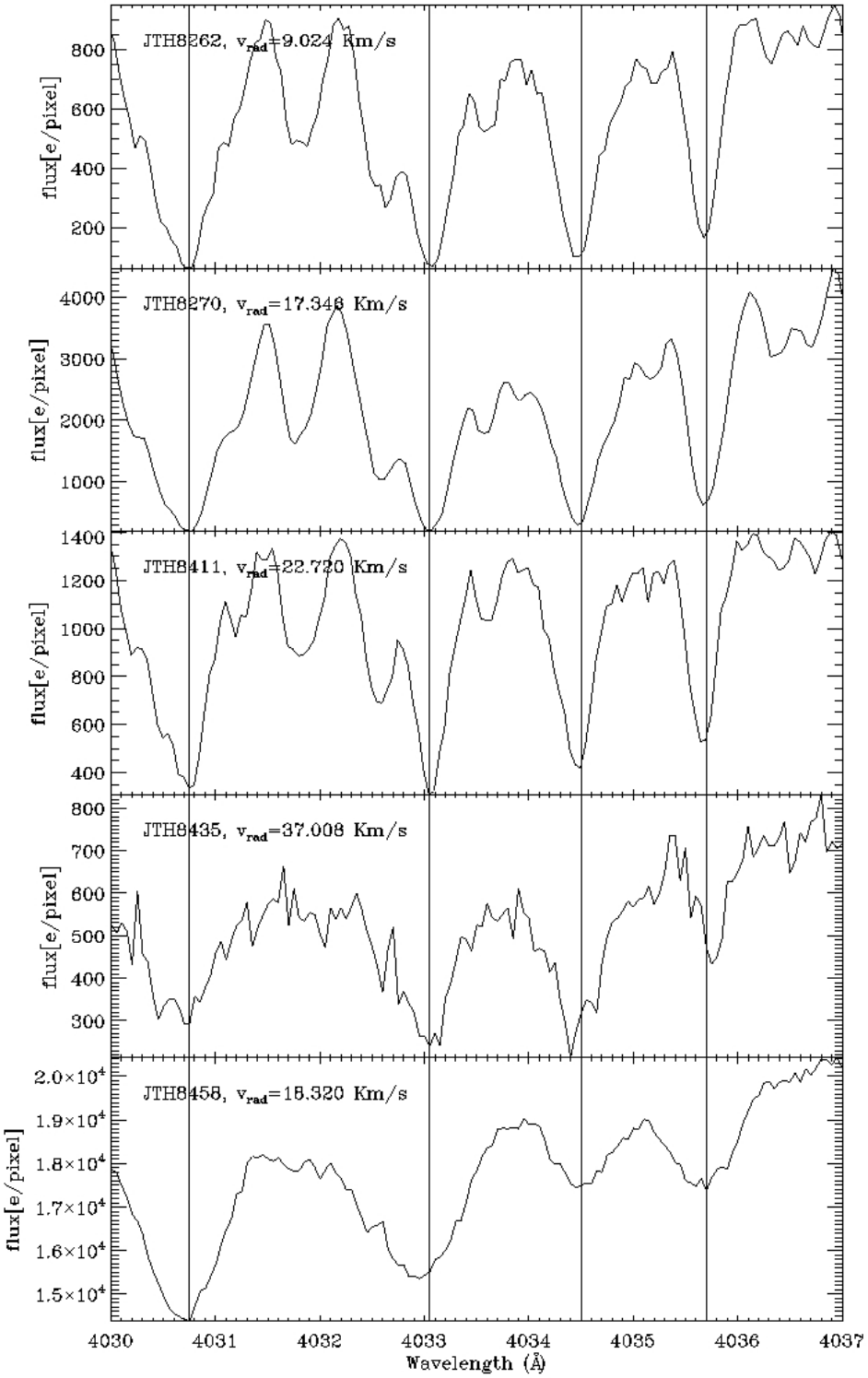

(d)

Figure A.1: continue

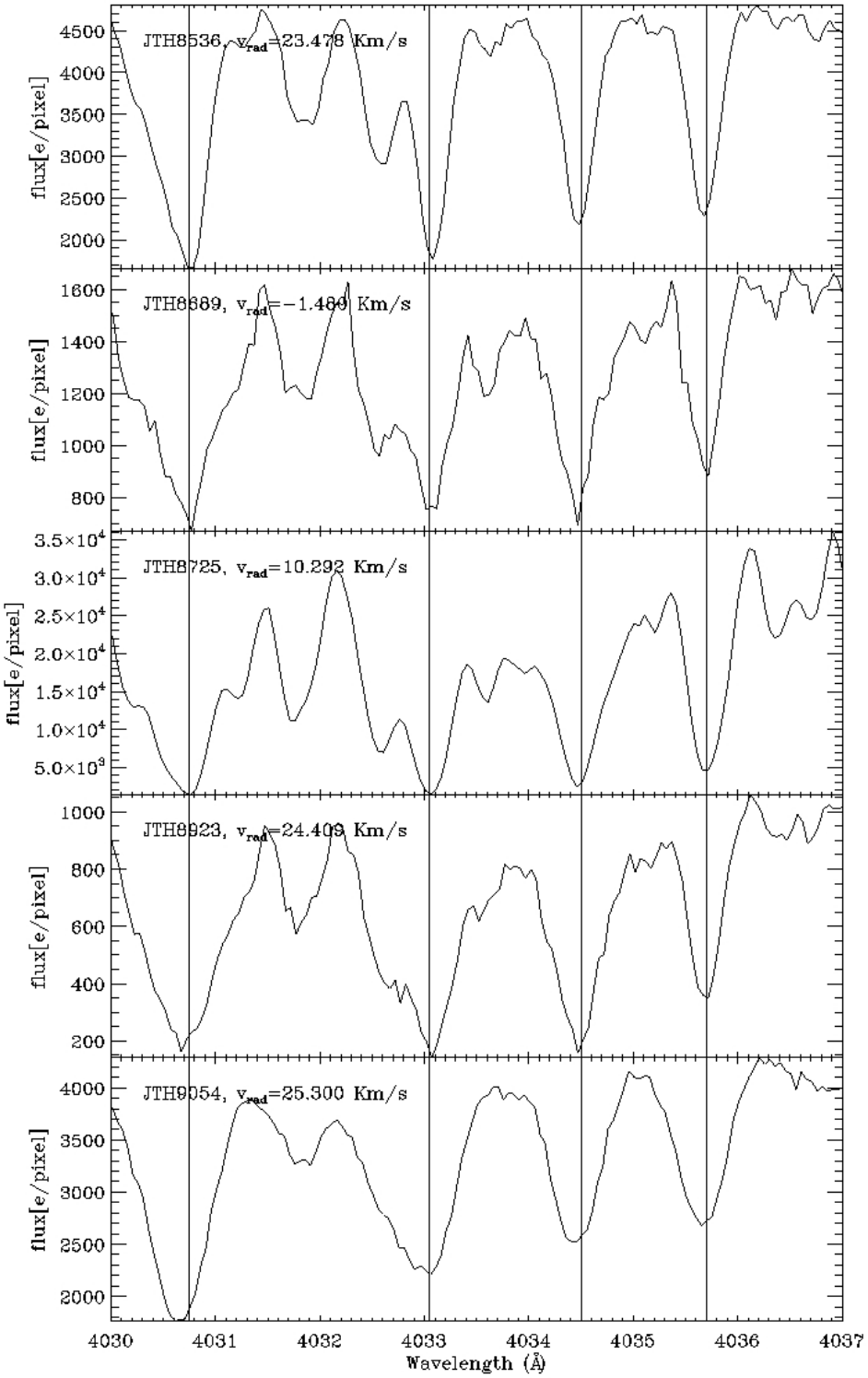

(e)

Figure A.1: continue

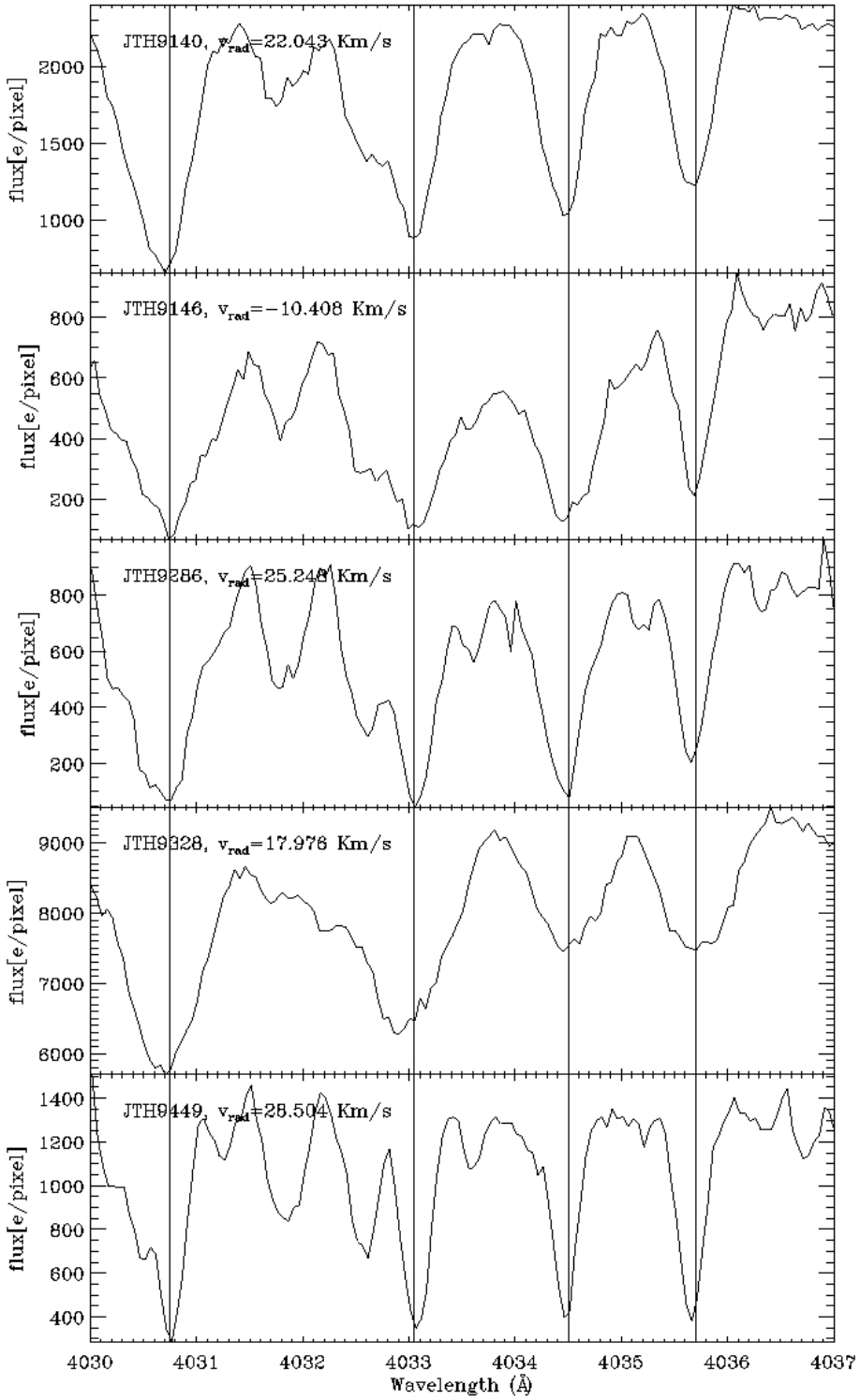

(f)

Figure A.1: continue

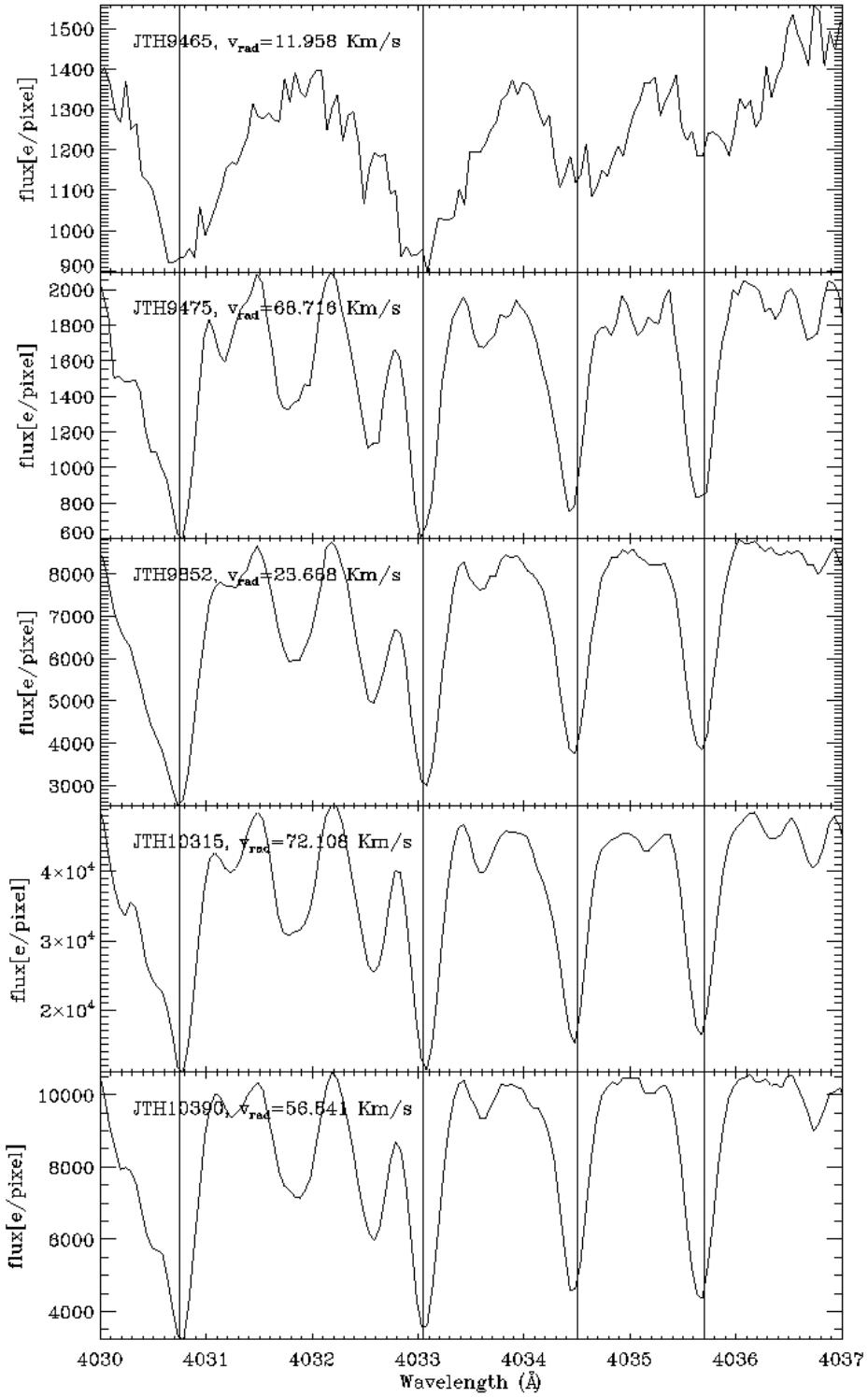

(g)

Figure A.1: continue

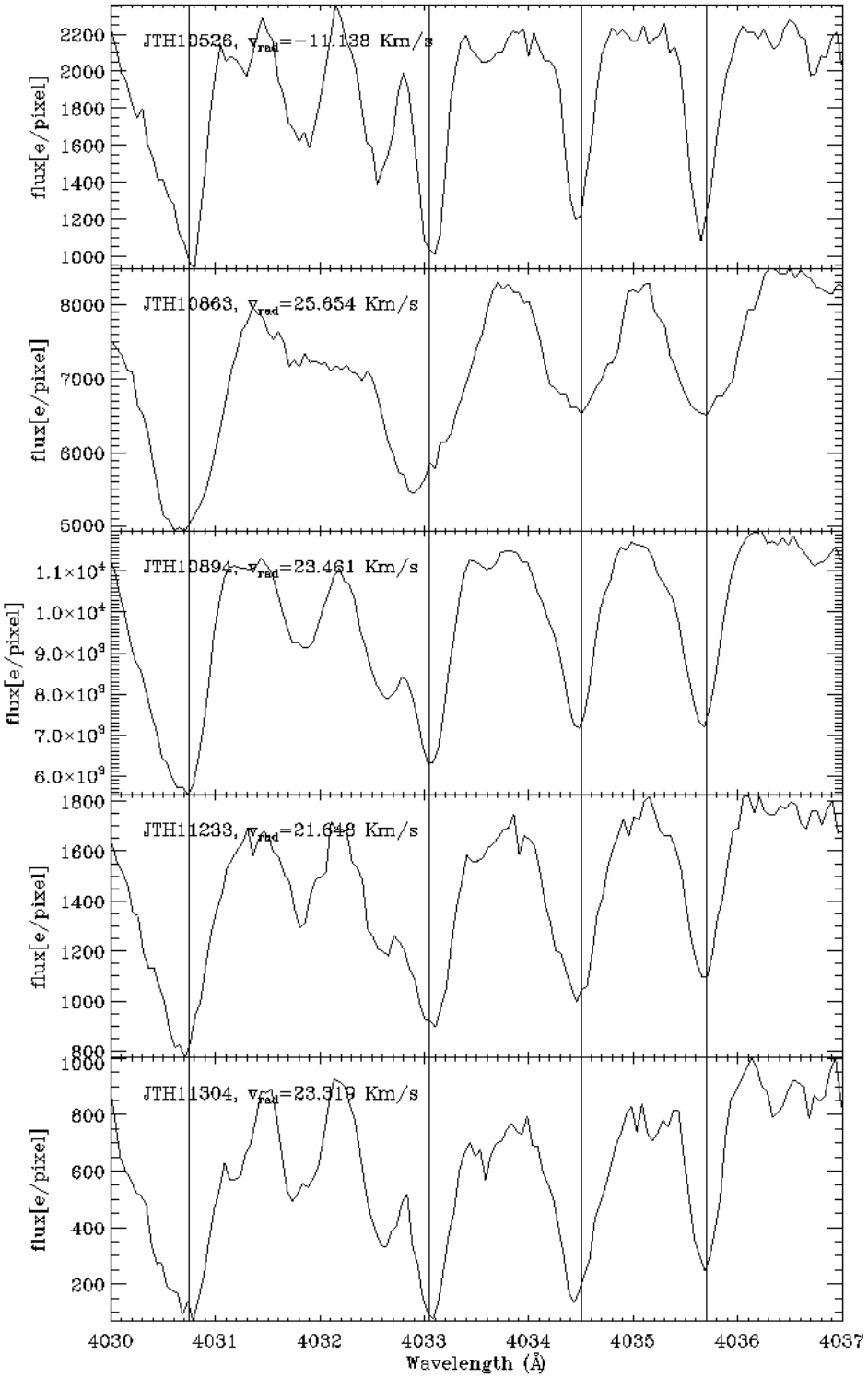

(h)

Figure A.1: continue

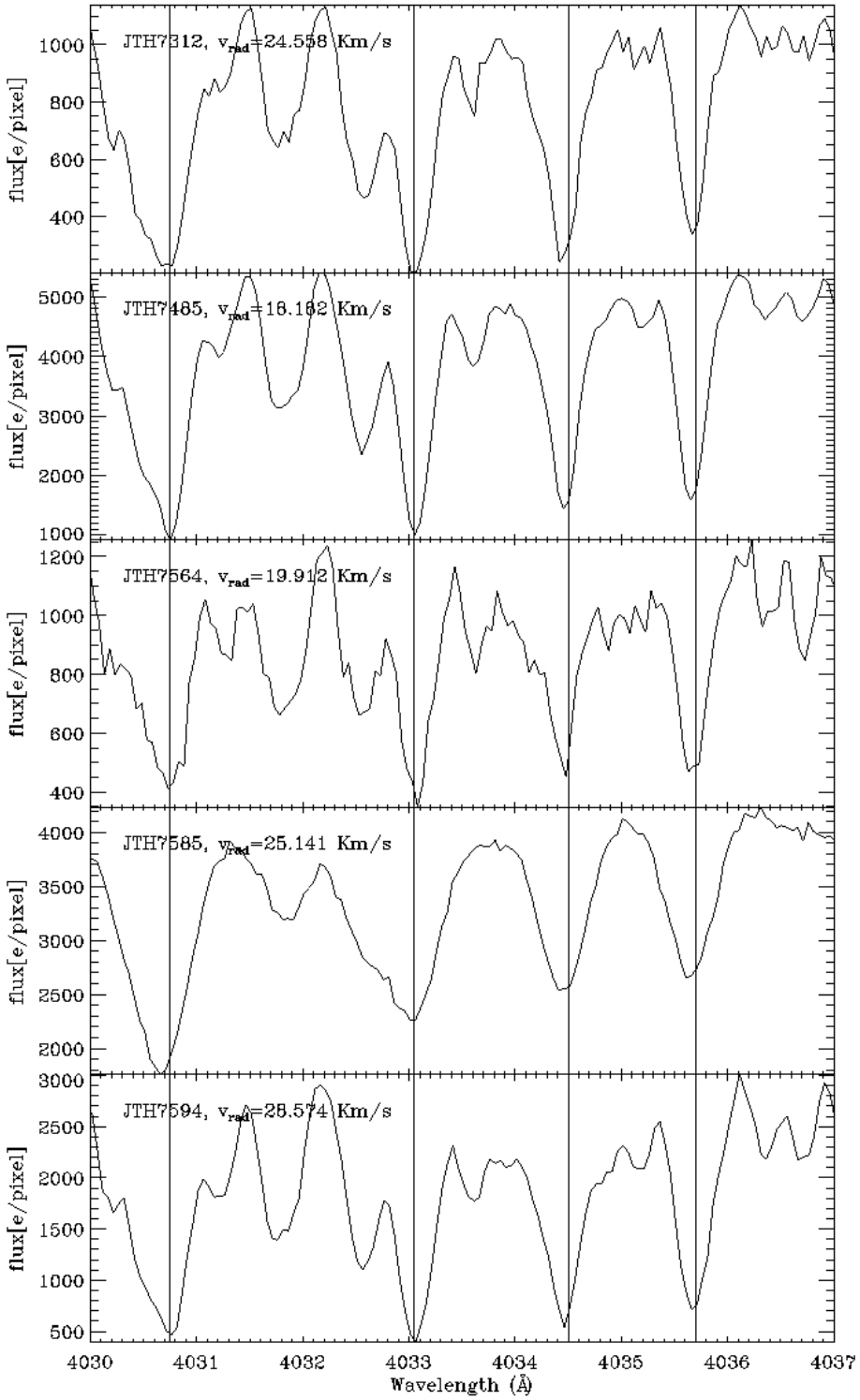

(i)

Figure A.1: continue

Appendix B

CaII H and K range

In Figure B.1 is plotted the range from 3925Å to 3975Å containing the H and K lines of CaII for stars of NGC2516 cluster for which I determined the $\log R'_{HK}$.

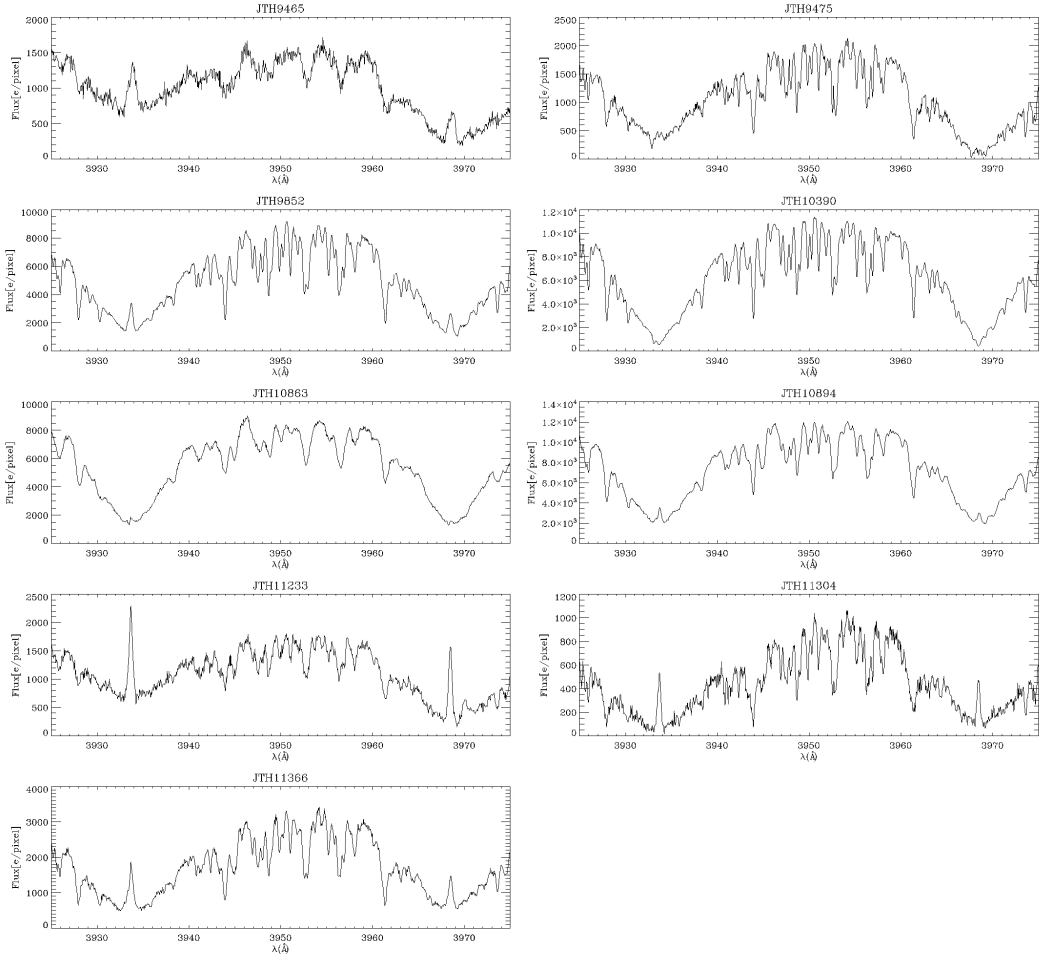

(a)

Figure B.1

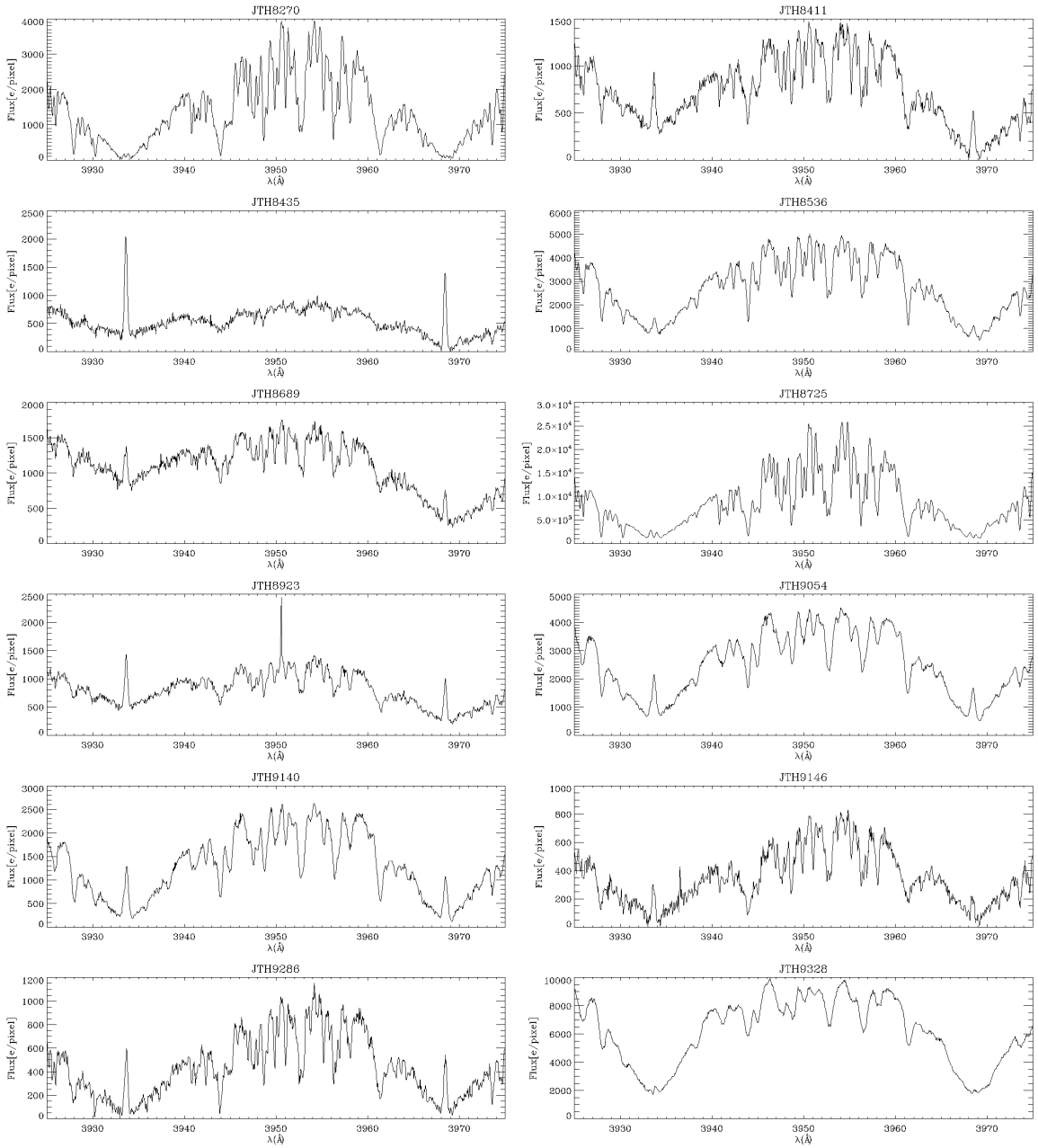

(b)

Figure B.1: continue

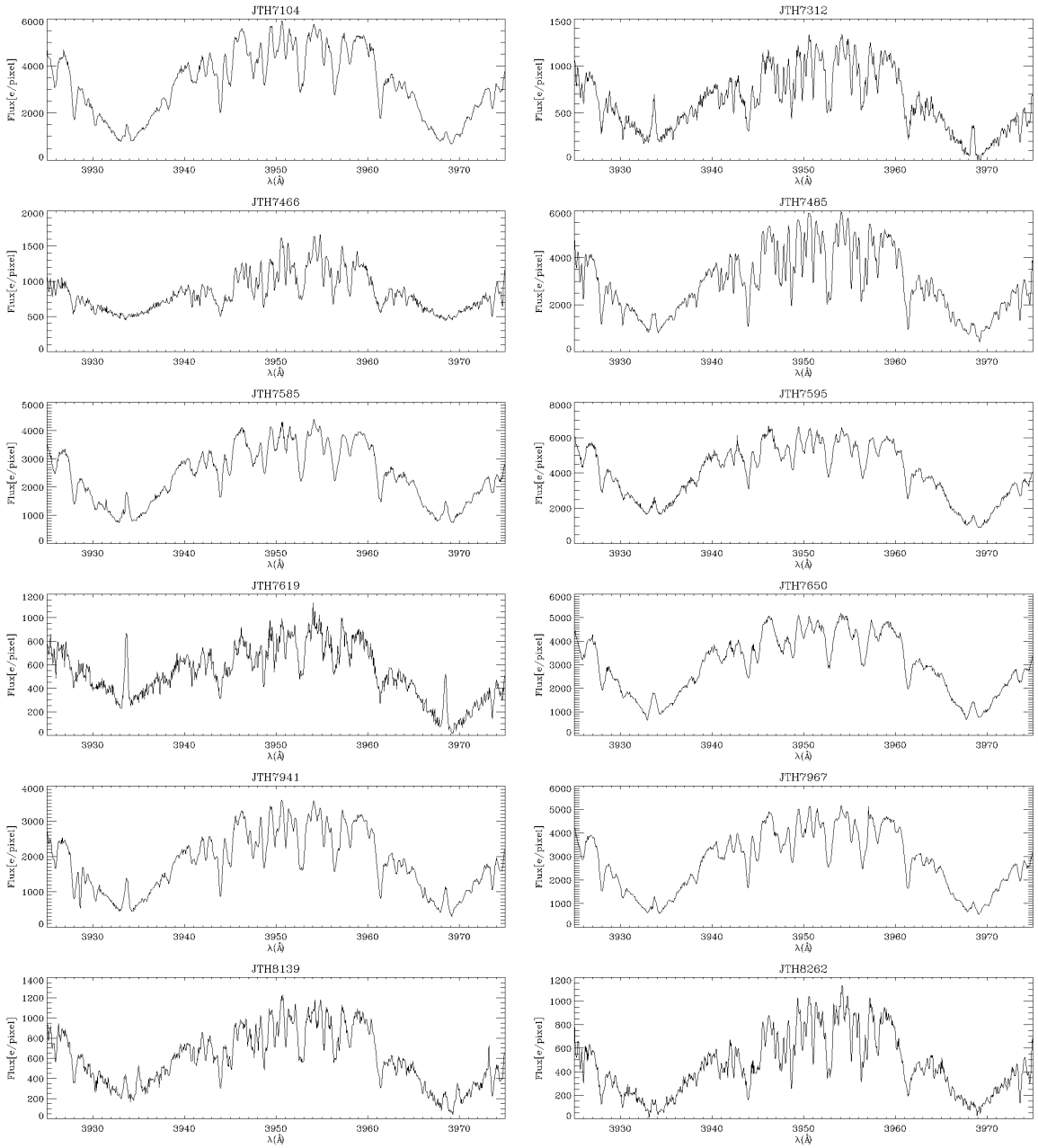

(c)

Figure B.1: continue

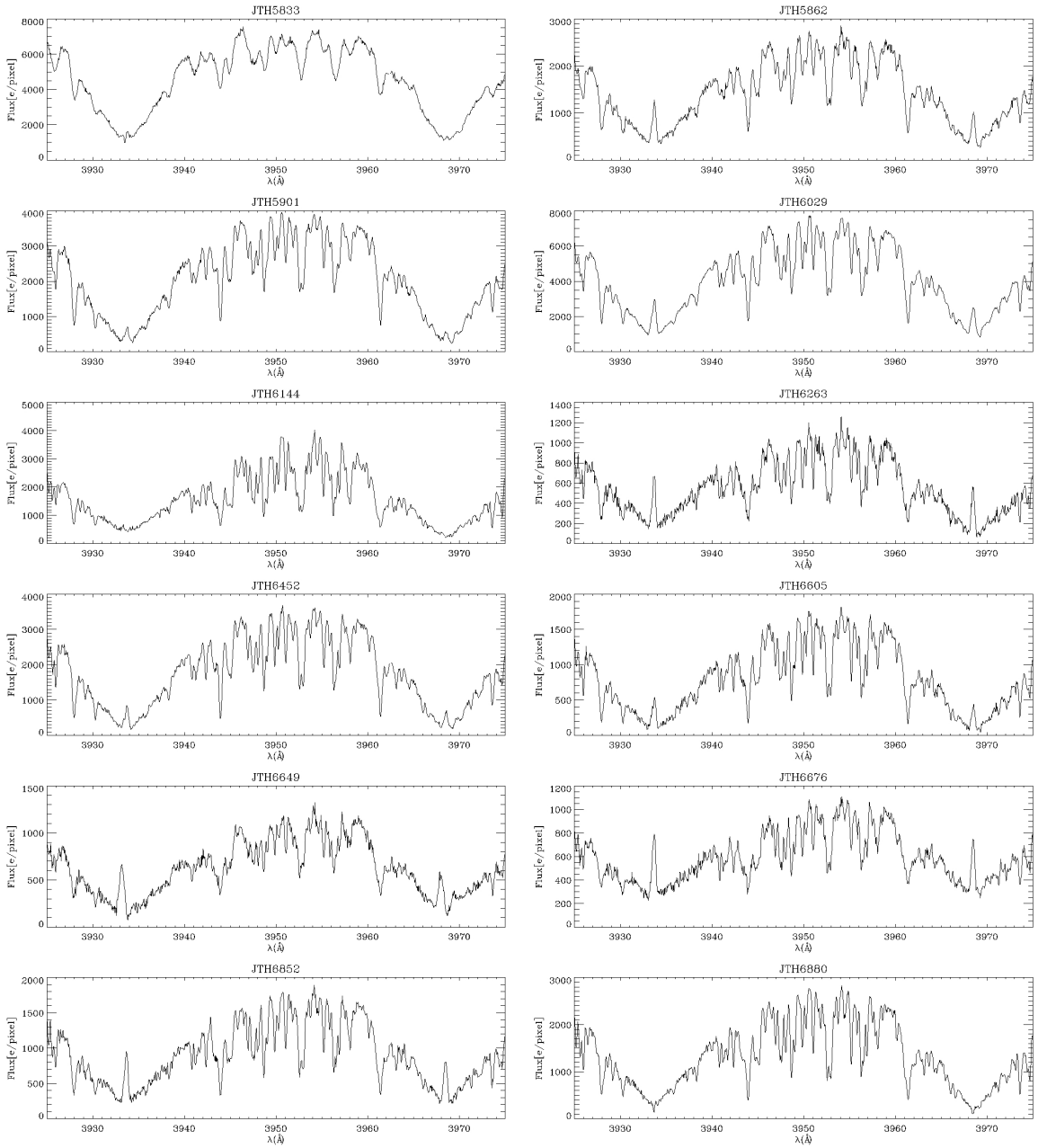

(d)

Figure B.1: continue

Appendix C

Lithium abundance NGC3766

In Table C.1 are listed the lithium abundances found for stars of NGC3766 open cluster, using a reddening of E(B-V)=0.175 and E(B-V)=0.22.

Table C.1: In the first column there is the number used in the numbering system of Messina, S. (private communication). In the next seven columns are listed the lithium abundance obtained for a reddening correction of E(B-V)=0.175. In details, in the second column there is the lithium abundance obtained without applying a blending correction. With + and - are listed the upper and lower errors. The same for the other four columns, except for EWcorr, that is the equivalent width obtained after the deblending. The same explanation is valid for the other columns, obtained for a reddening correction of E(B-V)=0.22.

	E(B-V)=0.175							E(B-V)=0.22						
	without correction			with blending correction				without correction			with blending correction			
N	logN(LiI)	-	+	EWcorr (mÅ)	logN(LiI)	-	+	logN(LiI)	-	+	EWcorr (mÅ)	log(NLiI)	-	+
12	2.02	0.18	0.13	-4.38				2.19	0.17	0.13	-4.33			
17	1.22	0.23	0.15	10.41	0.76	0.32	0.32	1.53	0.22	0.15	10.46	1.06	0.33	0.33
20	1.59	0.23	0.16	3.81	0.83	0.49	0.49	1.85	0.23	0.15	3.86	1.07	0.51	0.50
23	2.06	0.20	0.14	-7.43				2.06	0.20	0.14	-7.38			
29	1.54	0.15	0.12	1.58	0.52	0.55	0.55	1.98	0.15	0.11	1.64	0.89	0.63	0.63
32	2.12	0.06	0.06	170.43	2.04	0.06	0.06	2.12	0.06	0.06	170.49	2.04	0.06	0.06
57	2.87	0.08	0.09	136.24	2.79	0.09	0.08	3.10	0.09	0.09	136.29	3.01	0.09	0.09
61	2.56	0.12	0.11	48.45	2.41	0.15	0.13	2.76	0.12	0.10	48.50	2.61	0.15	0.12
62	1.20	0.37	0.23	25.06	0.95	0.83	0.31	1.42	0.38	0.23	25.11	1.17	0.93	0.31
65	2.84	0.17	0.16	260.62	2.75	0.17	0.17	3.05	0.16	0.16	260.68	2.97	0.16	0.16
66	2.12	0.21	0.14	7.86	1.58	0.36	0.36	2.33	0.21	0.13	7.92	1.79	0.36	0.36
77	2.45	0.11	0.09	134.8	2.37	0.12	0.11	2.66	0.11	0.11	134.86	2.57	0.12	0.11
78	2.02	0.12	0.09	13.08	1.61	0.34	0.20	2.20	0.12	0.09	13.14	1.81	0.34	0.19
79	2.33	0.16	0.13	23.94	2.09	0.36	0.19	2.71	0.16	0.13	23.99	2.47	0.36	0.19
80	2.01	0.12	0.10	55.75	1.86	0.16	0.13	2.19	0.12	0.11	55.81	2.05	0.15	0.13
89	2.36	0.09	0.08	115.55	2.27	0.09	0.09	2.36	0.09	0.08	115.60	2.27	0.09	0.09
90	2.34	0.11	0.10	164.90	2.26	0.11	0.11	2.59	0.09	0.09	164.96	2.51	0.10	0.09
95	2.31	0.13	0.11	22.32	2.06	0.29	0.17	2.52	0.12	0.11	22.37	2.27	0.29	0.17
109	2.37	0.10	0.10	170.81	2.29	0.10	0.10	2.37	0.10	0.10	170.87	2.29	0.10	0.10
126	1.97	0.17	0.11	10.27	1.50	0.68	0.27	2.16	0.16	0.11	10.32	1.70	0.69	0.27
129	2.19	0.08	0.07	85.43	2.09	0.09	0.08	2.39	0.08	0.07	85.48	2.28	0.09	0.08
140	1.47	0.12	0.10	53.63	1.32	0.16	0.13	1.69	0.12	0.11	53.68	1.54	0.15	0.13
144	2.41	0.09	0.09	125.02	2.32	0.10	0.09	2.61	0.10	0.09	125.07	2.51	0.11	0.10
145	2.49	0.09	0.07	66.19	2.37	0.10	0.09	2.69	0.09	0.08	66.25	2.56	0.10	0.09

Table C.1: (continued)

	E(B-V)=0.175							E(B-V)=0.22						
	without correction			with correction				without correction			with correction			
N	log(NLiI)	-	+	EWcorr(mÅ)	logNLiI	-	+	log(NLiI)	-	+	EWcorr(mÅ)	log(NLiI)	-	+
148	2.28	0.11	0.11	204.02	2.19	0.11	0.11	2.54	0.12	0.12	204.07	2.45	0.11	0.12
161	2.75	0.08	0.08	74.62	2.63	0.09	0.08	2.94	0.08	0.07	74.67	2.83	0.09	0.08
164	1.13	0.23	0.18	55.08	0.97	0.28	0.21	1.48	0.23	0.17	55.13	1.33	0.30	0.21
188	3.03	0.07	0.07	123.69	2.94	0.08	0.08	3.21	0.07	0.07	123.74	3.12	0.08	0.07
192	1.11	0.31	0.19	-6.08				1.31	0.31	0.19	-6.03			
196	1.88	0.12	0.11	79.76	1.76	0.14	0.12	2.17	0.12	0.09	79.81	2.05	0.13	0.12
198	2.39	0.09	0.09	51.52	2.25	0.13	0.11	2.59	0.10	0.09	51.58	2.44	0.13	0.11
205	1.65	0.19	0.15	48.57	1.48	0.24	0.18	1.95	0.18	0.14	48.62	1.79	0.24	0.17
271	1.69	0.11	0.10	146.83	1.59	0.11	0.11	2.01	0.09	0.09	146.89	1.92	0.10	0.09
299	2.42	0.10	0.09	55.62	2.28	0.13	0.11	2.62	0.11	0.09	55.68	2.48	0.13	0.11
308	3.07	0.08	0.08	95.50	2.96	0.09	0.09	3.26	0.09	0.08	95.56	3.16	0.09	0.09
315	1.34	0.17	0.12	18.52	1.02	0.38	0.23	1.64	0.17	0.13	18.57	1.33	0.42	0.22
354	1.63	0.10	0.09	46.39	1.46	0.13	0.11	1.93	0.09	0.08	46.45	1.77	0.13	0.11
362	2.33	0.09	0.08	162.87	2.24	0.09	0.09	2.58	0.08	0.08	162.92	2.50	0.09	0.08
373	2.45	0.10	0.09	35.21	2.26	0.15	0.11	2.65	0.10	0.08	35.27	2.46	0.14	0.11
388	2.63	0.07	0.06	87.74	2.52	0.08	0.07	2.83	0.08	0.07	87.79	2.72	0.08	0.08
399	2.34	0.11	0.09	76.63	2.22	0.13	0.11	2.56	0.10	0.09	76.69	2.45	0.13	0.10
422	2.83	0.09	0.07	35.17	2.64	0.11	0.09	2.83	0.09	0.08	35.23	2.64	0.12	0.09
484	2.99	0.07	0.06	53.52	2.84	0.09	0.08	2.99	0.07	0.07	53.58	2.84	0.09	0.08
524	1.36	0.27	0.17	19.47	1.04	0.66	0.28	1.36	0.27	0.18	19.53	1.05	0.66	0.29
527	2.45	0.10	0.08	58.78	2.31	0.13	0.10	2.64	0.11	0.09	58.83	2.50	0.13	0.11
535	2.63	0.08	0.07	56.38	2.48	0.10	0.09	2.82	0.08	0.07	56.44	2.68	0.09	0.08
546	2.41	0.08	0.08	89.41	2.31	0.09	0.09	2.64	0.08	0.07	89.47	2.53	0.09	0.08
551	2.29	0.32	0.25	103.75	2.20	0.38	0.27	2.49	0.34	0.27	103.80	2.39	0.39	0.28
584	1.85	0.13	0.12	74.34	1.72	0.16	0.13	2.13	0.13	0.11	74.39	2.01	0.15	0.13
601	2.75	0.09	0.09	198.59	2.67	0.09	0.09	2.97	0.10	0.10	198.65	2.88	0.09	0.10
602	1.28	0.35	0.35	-6.71				1.72	0.35	0.35	-6.65			

Table C.1: (continued)

	E(B-V)=0.175							E(B-V)=0.22						
	without correction			with correction				without correction			with correction			
N	log(NLiI)	-	+	EWcorr(mÅ)	logNLiI	-	+	log(NLiI)	-	+	EWcorr(mÅ)	log(NLiI)	-	+
614	2.54	0.21	0.13	10.16	2.07	1.79	0.31	2.53	0.21	0.13	10.21	2.08	1.67	0.31
618	3.04	0.23	0.19	60.12	2.90	0.21	0.21	3.04	0.23	0.19	60.18	2.90	0.29	0.21
622	0.54	0.29	0.20	2.89	0.13	0.29	0.29	0.86	0.38	0.21	2.94	0.18	0.54	0.54
636	1.09	0.36	0.21	16.35	0.75	0.35	0.35	1.31	0.37	0.21	16.41	0.96	0.36	0.36
645	1.88	0.19	0.14	40.57	1.69	0.27	0.19	2.07	0.18	0.14	40.62	1.89	0.28	0.18
657	1.26	0.59	0.26	-7.17				1.51	0.62	0.26	-7.12			
659	1.23	0.43	0.23	-2.69				1.43	0.43	0.23	-2.64			
669	2.61	0.09	0.09	124.70	2.51	0.09	0.09	2.82	0.09	0.08	124.76	2.73	0.09	0.09
674	1.43	0.92	0.31	-2.62				1.68	0.98	0.30	-2.57			
676	1.94	0.32	0.19	-9.47				1.94	0.32	0.19	-9.41			
681	1.68	0.19	0.16	51.93	1.52	0.26	0.19	1.98	0.19	0.15	51.98	1.82	0.26	0.18
703	2.11	0.09	0.08	70.79	1.99	0.11	0.09	2.53	0.08	0.08	70.85	2.41	0.11	0.09
712	1.76	0.41	0.41	12.47	1.34	0.68	0.68	2.01	0.39	0.39	12.53	1.59	0.67	0.67
716	2.87	0.13	0.13	177.80	2.78	0.13	0.13	3.07	0.12	0.12	177.86	2.98	0.12	0.12
723	2.84	0.11	0.09	35.92	2.65	0.15	0.12	2.84	0.11	0.09	35.98	2.65	0.15	0.12
725	2.09	0.23	0.17	67.35	1.96	0.29	0.20	2.28	0.23	0.18	67.41	2.15	0.28	0.20
728	2.55	0.10	0.09	25.49	2.33	0.22	0.13	2.73	0.11	0.09	25.55	2.50	0.22	0.14
758	2.17	0.24	0.16	-4.63				2.17	0.24	0.16	-4.57			
770	1.77	0.43	0.21	-12.16				1.77	0.43	0.21	-12.1			
802	1.96	0.12	0.10	50.47	1.81	0.16	0.13	2.15	0.12	0.10	50.52	1.99	0.14	0.13
826	1.46	0.49	0.25	-1.63				1.71	0.51	0.24	-1.57			
843	1.52	0.28	0.18	0.636	0.29	0.90	0.90	1.77	0.28	0.18	0.69	0.45	0.99	0.99
855	3.22	0.07	0.08	160.63	3.13	0.07	0.07	3.39	0.06	0.07	160.68	3.31	0.07	0.07
858	1.31	0.23	0.15	15.56	0.94	0.61	0.28	1.60	0.22	0.15	15.61	1.24	0.71	0.28
871	0.75	0.78	0.78	-1.76				0.96	0.79	0.79	-1.70			
883	0.95	0.32	0.32	-12.55				1.38	0.33	0.33	-12.49			

Bibliography

Athay, R. G. 1981, NASA Special Publication, 450, 85

Avrett, E. H. 1985, Chromospheric Diagnostics and Modelling, 67,

Avrett, E. H., & Loeser, R. 1992, Cool Stars, Stellar Systems, and the Sun,26, 489

Ayres, T. R., Linsky, J. L., & Shine, R. A. 1974, ApJ, 192, 93

Ayres, T. R., & Linsky, J. L. 1975, ApJ, 200, 660

Baliunas, S. L., et al. 1995, ApJ, 438, 269,

Baliunas, S. L., Donahue, R. A., Soon, W., & Henry, G. W. 1998, Cool Stars, Stellar Systems, and the Sun, 154, 153,

Baraffe, I., Chabrier, G., Allard, F., & Hauschildt, P. H. 1998, A&A, 337, 403

Barrado y Navascues, D., & Stauffer, J. R. 1996, A&A, 310, 879

Biazzo, K., Frasca, A., Catalano, S., & Marilli, E. 2006, A&A, 446, 1129,

Biazzo, K., Frasca, A., Henry, G. W., Catalano, S., & Marilli, E. 2007, ApJ, 656, 474,

Blanco, C., Catalano, S., Marilli, E., & Rodonò, M. 1974,A&A, 33, 257,

Blecha, A. Simond,G, 2004, GIRAFFE BLDR Software - Reference Manual,

Busà, I., Andretta, V., Gomez, M. T., & Terranegra, L. 2003, The Future of Cool-Star Astrophysics: 12th Cambridge Workshop on Cool Stars, Stellar Systems, and the Sun , 12, 1134

Busà, I., Aznar Cuadrado, R., Terranegra, L., Andretta, V., & Gomez, M. T. 2007, A&A, 466, 1089,

Cabrera-Cano, J., & Alfaro, E. J. 1985, A&A, 150, 298

Cabrera-Cano, J., & Alfaro, E. J. 1990, A&A, 235, 94

Cameron, L. M. 1985, A&A, 147, 39,

Carlsson, M. 1992, Cool Stars, Stellar Systems, and the Sun, 26, 499

Carlsson, M., Rutten, R. J., Bruls, J. H. M. J., & Shchukina, N. G. 1994, A&A, 288, 860

Castelli, F., & Kurucz, R. L. 2004,

Catalano, S. 1979, A&A, 80, 317,

Cayrel de Strobel, G., & Spite, M. 1988, The Impact of Very High S/N Spectroscopy on Stellar Physics, IAU Symposium No. 132,

Cerruti-Sola, M., Cheng, C.-C., & Pallavicini, R. 1992, A&A, 256, 185,

Chaboyer, B., Demarque, P., & Pinsonneault, M. H. 1995, ApJ, 441, 876

Chmielewski, Y. 2000, A&A, 353, 666,

Cincunegui, C., Díaz, R. F., & Mauas, P. J. D. 2007, A&A, 469, 309,

Cox, A. N. 1955, ApJ, 121, 628,

Cox, A. N. 2000, Allen's Astrophysical Quantities,

Dachs, J., & Hummel, W. 1996, A&A, 312, 818,

Dachs, J., & Kabus, H. 1989, A&AS, 78, 25,

Damiani, F., Flaccomio, E., Micela, G., Sciortino, S., Harnden, F. R., Jr., Murray, S. S., Wolk, S. J., & Jeffries, R. D. 2003, ApJ, 588, 1009,

Duncan, D. K., et al. 1991, ApJS, 76, 383,

Eberhard, G., & Schwarzschild, K. 1913, ApJ, 38, 292,

Eggen, O.J. 1972, Apj, 173, 63,

Fawzy, D., Rammacher, W., Ulmschneider, P., Musielak, Z. E., & Stępień, K. 2002, A&A, 386, 971,

Fernández-Figueroa, M. J., Montes, D., de Castro, E., & Cornide, M. 1994, ApJS, 90, 433,

Fosbury, R. A. E. 1974, MNRAS, 169, 147,

Gálvez, M. C., Montes, D., Fernández-Figueroa, M. J., de Castro, E., & Cornide, M. 2007, A&A, 472, 587,

Gálvez, M. C., Montes, D., Fernández-Figueroa, M. J., De Castro, E., & Cornide, M. 2009, AJ, 137, 3965,

Giampapa, M. S., Cram, L. E., & Wild, W. J. 1989, ApJ, 345, 536,

González, J. F., & Lapasset, E. 2000, AJ, 119, 2296,

Gray, D. F. 2005, The Observation and Analysis of Stellar Photospheres, 3rd Edition, by D.F. Gray. ISBN 0521851866. Cambridge, UK: Cambridge University Press, 2005,

Gray, R. O., Corbally, C. J., Garrison, R. F., McFadden, M. T., Bubar, E. J., McGahee, C. E., O'Donoghue, A. A., & Knox, E. R. 2006, AJ, 132, 161,

Griffin, R., Griffin, R., & Beggs, D. W. 1994, MNRAS, 270, 409,

Hall, J. C. 1996, PASP, 108, 313,

Hall, J. C. 2008, Living Reviews in Solar Physics, 5, 2,

Hall, J. C., Lockwood, G. W., & Skiff, B. A. 2007, AJ, 133, 862,

Harnden, F. R., Jr., et al. 2001, ApJL, 547, L141,

Hartmann, L., Soderblom, D. R., Noyes, R. W., Burnham, N., & Vaughan, A. H. 1984, ApJ, 276, 254,

Hawley, S. L., Tourtellot, J. G., & Reid, I. N. 1999, AJ, 117, 1341,

Heath, D. F., & Schlesinger, B. M. 1986, JGR, 91, 8672,

Henry, T. J., Soderblom, D. R., Donahue, R. A., & Baliunas, S. L. 1996, AJ, 111, 439,

Hillenbrand, L., Mamajek, E., Stauffer, J., Soderblom, D., Carpenter, J., & Meyer, M. 2009, American Institute of Physics Conference Series, 1094, 800

Kelch, W. L., Worden, S. P., & Linsky, J. L. 1979, ApJ, 229, 700,

King, D. S. 1978, Journal and Proceedings of the Royal Society of New South Wales, 111, 61,

King, J. R. 1998, AJ, 116, 254

Kurucz, R. 1993, SYNTHE Spectrum Synthesis Programs and Line Data. Kurucz CD-ROM No. 18. Cambridge, Mass.: Smithsonian Astrophysical Observatory, 1993., 18,

Irwin, J., Hodgkin, S., Aigrain, S., Hebb, L., Bouvier, J., Clarke, C., Moraux, E., & Bramich, D. M. 2007, MNRAS, 377, 741,

Jackson, R. J., & Jeffries, R. D. 2010, MNRAS, 925

Jefferies, J. T., & Thomas, R. N. 1959, ApJ, 129, 401

Jeffries, R. D. 2000, Stellar Clusters and Associations: Convection, Rotation, and Dynamos, 198, 245

Jeffries, R. D., James, D. J., & Thurston, M. R. 1998, MNRAS, 300, 550,

Jeffries, R. D., Thurston, M. R., & Hambly, N. C. 2001, A&A, 375, 863,

Jeffries, R. D., Thurston, M. R., & Pye, J. P. 1997, MNRAS, 287, 350,

Jeffries, R. D., Jackson, R. J., James, D. J., & Cargile, P. A. 2009,MNRAS, 400, 317

Johnson, H. L., Iriarte, B., Mitchell, R. I., & Wisniewski, W. Z. 1966, Communications of the Lunar and Planetary Laboratory, 4, 99,

Lanzafame, A. C. 1995, A&A, 302, 839

Linsky, J. L., & Ayres, T. R. 1978, Apj, 220, 619,

Linsky, J. L., Hunten, D. M., Sowell, R., Glackin, D. L., & Kelch, W. L. 1979a, ApJS, 41, 481,

Linsky, J. L., McClintock, W., Robertson, R. M., & Worden, S. P. 1979b, ApJs, 41,47,

Lubin, D., Tytler, D., & Kirkman, D. 2010, ApJ, 716, 766

Mallik, S. V. 1997, A&AS, 124, 359,

Mallik, S. V. 1998, Bulletin of the Astronomical Society of India, 26, 479,

Mamajek, E. E. 2009, IAU Symposium, 258, 375

Mamajek, E. E., & Hillenbrand, L. A. 2008, ApJ, 687, 1264

Marino, A., Micela, G., Pillitteri, I., & Peres, G. 2006,A&A, 456, 977,

McSwain, M. V. 2008, ApJ, 686, 1269

Meibom, S. 2000, A&A, 361, 929,

Meynet, G., Mermilliod, J.-C., & Maeder, A. 1993, A&AS, 98, 477,

Messina, A.E., Lanzafame, A.C, Busá Innocenza, 2010a, "Chromospheric activity and Lithium abundance in NGC2516", in Astrophysics and Space Science Proceedings series, A. Moitinho & J.F. Alves (eds.), *in press*

Messina, S., Desidera, S., Turatto, M., Lanzafame, A. C., & Guinan, E. F. 2010, A&A, 520, A15

Micela, G., Sciortino, S., Jeffries, R. D., Thurston, M. R., & Favata, F. 2000, A&A, 357, 909,

Michaud, G., & Charbonneau, P. 1991, Space Science Reviews, 57, 1

Middelkoop, F. 1982, A&A, 107, 31,

Moitinho, A., Alfaro, E. J., Yun, J. L., & Phelps, R. L. 1997, AJ, 113, 1359

Montes, D., de Castro, E., Fernández-Figueroa, M. J., & Cornide, M. 1995a, A&AS, 114, 287,

Montes, D., Fernández-Figueroa, M. J., de Castro, E., & Cornide, M. 1994, A&A, 285, 609,

Montes, D., Fernández-Figueroa, M. J., de Castro, E., & Cornide, M. 1995b, A&A, 294, 165,

Montes, D., Fernández-Figueroa, M. J., de Castro, E., & Cornide, M. 1995c, A&AS, 109, 135,

Montes, D., Fernández-Figueroa, M. J., de Castro, E., & Sanz-Forcada, J. 1997, A&AS, 125, 263,

Montes, D., Fernández-Figueroa, M. J., De Castro, E., Cornide, M., Latorre, A., & Sanz-Forcada, J. 2000,A&AS, 146, 103,

Montes, D., Sanz-Forcada, J., Fernández-Figueroa, M. J., de Castro, E., & Poncet, A. 1998, A&A, 330, 155,

Narain, U., & Ulmschneider, P. 1996, Space Science Reviews, 75, 453,

Naylor, T., Mayne, N. J., Jeffries, R. D., Littlefair, S. P., & Saunders, E. S. 2009, IAU Symposium, 258, 103

Noyes, R. W. 1983, Solar and Stellar Magnetic Fields: Origins and Coronal Effects, 102, 133

Noyes, R. W., Hartmann, L. W., Baliunas, S. L., Duncan, D. K., & Vaughan, A. H. 1984, ApJ, 279, 763,

Oranje, B. J., & Zwaan, C. 1985, A&A, 147, 265,

Pace, G., Pasquini, L., & Ortolani, S. 2003, A&A, 401, 997,

Pasquini, L., de Medeiros, J. R., & Girardi, L. 2000, A&A, 361, 1011

Pasquini, L., & Pallavicini, R. 1991, A&A, 251, 199

Pasquini, L., Pallavicini, R., & Pakull, M. 1988, A&A, 191, 253

Pillitteri, I., Micela, G., Damiani, F., & Sciortino, S. 2006, A&A, 450, 993

Pinsonneault, M. H., Stauffer, J., Soderblom, D. R., King, J. R., & Hanson, R. B. 1998, ApJ, 504, 170,

Randich, S., Aharpour, N., Pallavicini, R., Prosser, C. F., & Stauffer, J. R. 1997, A&A, 323, 86

Randich, S., Primas, F., Pasquini, L., Sestito, P., & Pallavicini, R. 2007, A&A, 469, 163,

Robichon, N., Arenou, F., Mermilliod, J.-C., & Turon, C. 1999, A&A, 345, 471,

Robinson, R. D., Cram, L. E., & Giampapa, M. S. 1990, ApJS, 74, 891

Rutten, R. G. M., Schrijver, C. J., Lemmens, A. F. P., & Zwaan, C. 1991, A&A, 252, 203

Saar, S. H., & Linsky, J. L. 1985, ApJ, 299, L47

Schrijver, C. J. 1983, A&A, 127, 289

Schrijver, C. J. 1987, A&A, 172, 111

Schrijver, C. J. 1993, A&A, 269, 395

Schrijver, C. J., Cote, J., Zwaan, C., & Saar, S. H. 1989, ApJ, 337, 964

Schrijver, C. J., Dobson, A. K., & Radick, R. R. 1992, A&A, 258, 432

Schrijver, C. J., & Zwaan, C. 2000, Solar and stellar magnetic activity / Carolus J. Schrijver, Cornelius Zwaan. New York : Cambridge University Press, 2000. (Cambridge astrophysics series ; 34),

Sciortino, S., et al. 2001, A&A, 365, L259,

Shobbrook, R. R. 1985, MNRAS, 212, 591

Shobbrook, R. R. 1987, MNRAS, 225, 999

Siess, L., Dufour, E., & Forestini, M. 2000, A&A, 358, 593

Skumanich, A. 1972, ApJ, 171, 565

Slettebak, A. 1985, ApJS, 59, 769

Soderblom, D. R. 2010, ARA&A, 48, 581

Soderblom, D. R., Jones, B. F., Balachandran, S., Stauffer, J. R., Duncan, D. K., Fedele, S. B., & Hudon, J. D. 1993a, AJ, 106, 1059

Soderblom, D. R., King, J. R., Siess, L., Jones, B. F., & Fischer, D. 1999, AJ, 118, 1301

Soderblom, D. R., Pilachowski, C. A., Fedele, S. B., & Jones, B. F. 1993b, AJ, 105, 2299

Solanki, S. K., Steiner, O., & Uitenbroeck, H. 1991, A&A, 250, 220

Stauffer, J. 2000, Stellar Clusters and Associations: Convection, Rotation, and Dynamos, 198, 255

Stauffer, J. R. 2004, Debris Disks and the Formation of Planets, 324, 100

Strassmeier, K. G. 1994, A&A, 281, 395

Strassmeier, K. G., Fekel, F. C., Bopp, B. W., Dempsey, R. C., & Henry, G. W. 1990, ApJS, 72, 191

Strassmeier, K. G., Handler, G., Paunzen, E., & Rauth, M. 1994, A&A, 281, 855,

Strassmeier, K., Washuettl, A., Granzer, T., Scheck, M., & Weber, M. 2000, A&AS, 142, 275,

Sung, H., Bessell, M. S., Lee, B.-W., & Lee, S.-G. 2002, AJ, 123, 290,

Tadross, A. L. 2001, New Astronomy, 6, 293

Terndrup, D. M., Pinsonneault, M., Jeffries, R. D., Ford, A., Stauffer, J. R., & Sills, A. 2002, ApJ, 576, 950,

Thatcher, J. D., & Robinson, R. D. 1993, MNRAS, 262, 1

Tinney, C. G., McCarthy, C., Jones, H. R. A., Butler, R. P., Carter, B. D., Marcy, G. W., & Penny, A. J. 2002, MNRAS, 332, 759

Tschäpe, R., Rüdiger, G. 2001, A&A, 377, 84

Vaughan, A. H., & Preston, G. W. 1980, PASP, 92, 385

Vaughan, A. H., Preston, G. W., & Wilson, O. C. 1978, PASP, 90, 267

Vernazza, J. E., Avrett, E. H., & Loeser, R. 1973, ApJ, 184, 605

Vernazza, J. E., Avrett, E. H., & Loeser, R. 1976, ApJS, 30, 1

Vernazza, J. E., Avrett, E. H., & Loeser, R. 1981, ApJS, 45, 635

Vieytes, M., & Mauas, P. J. D. 2004, Ap&SS, 290, 311

Ulmschneider, P., Fawzy, D., Musielak, Z. E., & Stępień, K. 2001, ApJ, 559, L167

White, R. J., Gabor, J. M., & Hillenbrand, L. A. 2007, AJ, 133, 2524

Willstrop, R. V. 1965, MmRAS, 69, 83,

Wilson, O. C. 1963, ApJ, 138, 832,

Wilson, O. C. 1968, ApJ, 153, 221

Wilson, O. C. 1978, ApJ, 226, 379

Wilson, O. C., & Vainu Bappu, M. K. 1957, ApJ, 125, 661

Wolk, S. J., et al. 2004, ApJ, 606, 466

Wright, J. T., Marcy, G. W., Butler, R. P., & Vogt, S. S. 2004,ApJS, 152, 261

Yilmaz, F. 1976, A&AS, 26, 1

Zwaan, C. 1991, Mechanisms of Chromospheric and Coronal Heating, 241.